

Heuristic and deterministic computational
solutions for solid-state NMR and molecular
spectroscopy

(Dennis) L. A. G. Grimminck

ISBN/EAN 978-94-6191-743-0

Heuristic and deterministic computational solutions
for solid-state NMR and molecular spectroscopy

(Dennis) L. A. G. Grimminck

PhD Thesis Radboud University Nijmegen

Cover design by (Dennis) L. A. G. Grimminck and Frans R. Spiering

Printed by Ipskamp Drukkers B.V.

Heuristic and deterministic computational solutions for solid-state NMR and molecular spectroscopy

Proefschrift

ter verkrijging van de graad van doctor
aan de Radboud Universiteit Nijmegen
op gezag van de rector magnificus prof. mr. S.C.J.J. Kortmann,
volgens besluit van het college van decanen
in het openbaar te verdedigen op donderdag 13 juni 2013
om 10.30 uur precies

door

(Dennis) Leonardus Adrianus Gerardus Grimminck

geboren op 28 mei 1985
te Roosendaal en Nispen

Promotoren

Prof. dr. W. L. Meerts (Vrije Universiteit Amsterdam)

Prof. dr. A. P. M. Kentgens

Prof. dr. ir. G. C. Groenenboom

Manuscriptcommissie

Prof. dr. D. H. Parker

Dr. L. Wiesenfeld (Institut de Planétologie et d'Astrophysique de Grenoble)

Prof. dr. D. Massiot (Centre national de la recherche scientifique, France)

Prof. dr. C. A. de Lange (Vrije Universiteit Amsterdam)

Dr. E. R. H. van Eck

Dankwoord

In mijn dankbetuigingen wil ik graag de route volgen die ik als interdisciplinair promovendus van het Instituut voor Moleculen en Materialen heb afgelegd in 4 jaar tijd. Begin 2009 had ik een bureau op de laser fysica afdeling(en). Een half jaar daarna verhuisde ik naar de NMR afdeling. Na tweeënhalf jaar NMR onderzoek ben ik gewisseld van onderwerp, niet van bureau, en bij de afdeling theoretische chemie begonnen.

Ik begin graag met het bedanken van mijn onofficiële 4e promotor Wim van der Zande. Beste Wim, bedankt voor je ‘chivalrous support’ [1], enthousiasme en betrokkenheid. Ik heb me altijd gesteund gevoeld en waardeer het zeer dat je met regelmaat even langskwam. Ik bewonder je bevoegdheid voor natuurkunde en ben blij dat we toch nog samen aan een project hebben kunnen werken.

Beste Leo, ik wil je bedanken voor je betrokkenheid en goede zorgen voor mij als begeleider. Naast de ontspannen gesprekken over werk en privé, waardeer ik heel erg de momenten waarop we samen onderzoek gedaan hebben. Daar heb ik veel van geleerd. Ook wil ik hier de kans gebruiken om je te bedanken voor alle mogelijkheden die je me hebt gegeven, o.a.: de NWO TopTalent aanvraag, onderzoek doen in Düsseldorf, conferenties en (last but not least) het regelen van een IMM promotieplaats. Ten slotte, ik vind het een eer om je laatste promovendus te zijn nu je met je emeritaat bent.

In de loop van de jaren heb ik veel mensen van de laser afdelingen in meer of mindere maten leren kennen. In het bijzonder wil ik Frans S. bedanken voor de plezierige samenwerking betreft het onderzoek, maar ook voor de steun tijdens de pittige tijd aan het einde van de mijn promotie. Verder zijn er een hoop mensen die ik wil bedanken om velerlei zaken: discussies, dagje-uit, borrelen, etc. Thank you all: Dave, Frans H., Simona, André, Afric, Jolijn, Cor, Leander, Nico, Rienk, Frans W., Gautam, Denis, Chandan, Raymund, Ashim, Julien, Devasena, Anouk, Ruurd, Elena, Arjan v. V., Arjan D. Mernoosh, Gerbe, Ivan, ZhiChau, Zahid, Vitali, Bas, Peter en Masha.

Dan is de volgende halte op mijn route de NMR afdeling. Arno, u wil ik als eerst bedanken voor: de discussies, uw kritische kijk op mijn geschreven werk en de goede bereikbaarheid voor vragen ondanks de drukke agenda. Het was leuk om methodologisch werk te doen aan quadrupool NMR met/voor iemand met zoveel liefde voor het onderwerp; de twinkeling in uw ogen is me niet ontgaan. Thank you Andreas and Suresh for the nice cooperation regarding the NMR experiments and the work on the paper’s manuscript. Geen experimenten zonder technische hulp, dus bedank ik ook graag: Jan v. O., Hans J. en Gerrit. Margriet en Ernst wil ik bedanken voor de metingen die ze hebben gedaan. Daarnaast wil ik Ernst ook bedanken voor het kritisch lezen van mijn manuscripten. Bas, jou wil ik bedanken voor de gesmeerde samenwerking (we

hebben een paper!) en het feit dat jij mijn enige en dus enigste student wilde zijn. Ten slotte wil ik graag iedereen van de afdeling bedanken voor de gezellige koffiepauzes en overige activiteiten, thank you all: Arno, Suresh, Andreas, Margriet, Ernst, Jan v. B., Bas, Gijs, Mithun, Chandra, Jan v. O., Hans J., Ruud, Hans H., Ard, Vincent, Marc, Vipin, Sjaak, Sybren, James, Vinod, Lavinia, Michael, Ole, Koen, Anna-Jo, Gerrit, Martijn, Leon, Ramon, Kirsten, Aafke, Frank, Marco, Nan en Niels.

De laatste halte sinds april 2011 is de afdeling theoretische chemie. Wegens mijn focus op een afgerond proefschrift binnen 4 jaar heb ik helaas minder met afdelingsactiviteiten meegedaan. Gerrit, graag bedank ik jou voor de mogelijkheid om onder jouw begeleiding onderzoek te kunnen doen. Het is voor mij een eer dat ik jouw eerste promovendus ben die jij als hoogleraar promoveert. Ook wil ik Ad bedanken voor zijn belangrijke suggesties gedurende het hele onderzoek. Gerrit en Ad, ik bewonder de precisie waarmee jullie theorie bedrijven en beschrijven, wat mij betreft een niveau wat ik altijd na zal streven. Ook wil ik Liesbeth bedanken voor het gebruiksklaar maken van en de hulp bij haar scatteringcode. Dat was een flinke sprong voorwaarts in het onderzoek. De overige collega's wil ik bedanken voor de goede sfeer, thank you all: Tijs, Simon, Rik, Herma, Leendertjan, Thanja, Joost, Lei Song, Sasha, Dick en Michał.

Gedurende mijn promotie heb ik ook twee jaar in de organisatie van de OIIMMpiade deelgenomen. Graag bedank ik: Pieter, Marie-Louise, Frans S., Anja, Aafke en Kirsten voor de goede en leuke samenwerking. Als (half-)theoreticus kun je niet zonder een goed functionerend computernetwerk en de bijbehorende backups. In mijn ogen doet C&CZ dat uitstekend, daarvoor mijn dank aan: Bram, Ron, Ben, Erik, Peter, Wim en Caspar. Daarnaast wil ik de secretaresses apart bedanken, vanwege hun bijzondere rol in het reilen en zeilen binnen de universiteit. Bedankt voor jullie inzet en interesse: Marian, Miriam, Erna, Magda, Ine en Marieke.

Ik prijs me gelukkig met mijn achterban die een belangrijke bijdrage heeft geleverd aan deze mijlpaal in mijn leven. Een hoop vrienden en familie bedank ik voor hun interesse. Pa, ma en Nicole, jullie wil ik bedanken voor jullie onvoorwaardelijke liefde, steun en vertrouwen. Robbert en Marja, schoonpa en-ma, ik heb jullie leren kennen tijdens mijn promotie, bedankt voor jullie interesse en steun. Aryan, je hulp en vriendschap gedurende de promotietijd is voor mij erg waardevol geweest, bedankt.

Lieve Alvera, verliefd, verloofd, getrouwd, een nieuw thuis, onze prachtige dochter Linne en nu een volwassen promotiethesis. . . *I count my blessings* na 4 jaar heel hard werken. Wat ben ik jou dankbaar voor wie je bent.

Dennis Grimminck
Nijmegen, 16 april 2013

Scope of this thesis

This thesis covers my work on three research topics during my time as an interdisciplinary PhD student at the Institute for Molecules and Materials (IMM) in Nijmegen. I was part of two collaborations between the research group of molecular and biophysics, and both solid-state NMR and theoretical chemistry. The common factor between the topics is the development and use of computational methods for spectroscopy, while the range covers: experiment optimisation, data analysis, and actual prediction of experimental results.

This thesis is structured in a modular fashion: introduction to the subject, followed by the relevant paper(s). The first two topics are from the field of solid-state NMR and involve the heuristic computational approach hinted to in the title of this thesis. Both topics have in common that evolutionary algorithms are used for either, on-spectrometer optimisation of radio-frequency homonuclear decoupling pulse shapes, or to find the interaction parameters that provide the best match between simulation and experimental quadrupolar NMR data. These (heuristic) algorithms are a tool (not the goal!) to obtain the optimal solution by trial-and-error learning.

The third topic is from the field of molecular spectroscopy, where the influence of atomic collisions on the absorption of light by an oxygen molecule is theoretically studied and compared to experiment. The theory uses first principles to describe the physics, which means that only the fundamental constants and laws of physics are used. It therefore leads to a deterministic (one straightforward way) approach to compute the result and actually predict the experimental outcome. Hence the second part of my title is explained. The author wishes the reader a pleasant reading of his thesis.

Contents

Dankwoord	v
Scope of this thesis	vii
1 Nuclear spin interaction engineering in solid-state NMR	1
1.1 Solid-state NMR for protons	1
1.2 Interaction engineering	4
1.3 Decoupling by rotating the material	4
1.4 Decoupling using rf-pulses	5
1.5 Real-time pulse optimisation	6
1.6 Answers and perspectives	7
2 EASY-GOING DUMBO (paper)	9
2.1 Introduction	9
2.2 Materials and methods	11
2.3 Results and Discussion	17
2.4 Conclusions	23
3 Quadrupole NMR	25
3.1 Quadrupolar nuclei	25
3.2 Interaction parameters and local structure	26
3.3 Quadrupolar interaction as a perturbation	28

3.4	Typical line shapes	30
3.5	Excitation of quadrupolar nuclei	32
3.6	Multiple Quantum Magic Angle Spinning	34
4	EASY-GOING deconvolution: one dimensional spectra (paper)	37
4.1	Introduction	38
4.2	Theory	40
4.3	Evolutionary algorithms	43
4.4	<i>EASY-GOING deconvolution</i> program structure	44
4.5	Examples	45
4.6	Conclusions and outlook	49
4.7	Experimental	50
5	EASY-GOING deconvolution: MQMAS spectra (paper)	55
5.1	Introduction	56
5.2	Theory	57
5.3	The program	63
5.4	Examples	65
5.5	Discussion	72
5.6	Conclusions	73
5.7	Experimental	74
6	Pressure broadening in the impact approximation	77
6.1	Absorption of radiation by a molecular gas	77
6.2	Change in absorption by elastic particle collisions	78
6.3	Absorption line shape in the impact approximation	79
6.4	Multiple transitions and inelastic collisions	82
7	Pressure broadening of the oxygen A-band (paper)	85
7.1	Introduction	85
7.2	Theory	87
7.3	He-O ₂ (<i>b</i> ¹ Σ _g ⁺) interaction potential	93
7.4	Scattering calculations	97
7.5	Cavity ring-down experiments	99
7.6	Results and Discussion	102
7.7	Conclusions	108
	Bibliography	111

Summary	119
Samenvatting	123
Publications	127
Curriculum Vitae	129

CHAPTER 1

Nuclear spin interaction engineering in solid-state NMR: Manipulation in Euclidian and spin space

They make ten thousands of revolutions per second and are exposed to precisely tailored radio frequency (rf) pulse shapes. It is the daily routine for solid state materials during NMR (nuclear magnetic resonance) experiments in the Goudsmit-pavilion in Nijmegen. Measuring nuclear spin magnetisation provides information about structure and dynamics at the molecular level. Nuclear spins, however, interact in several ways with their surroundings. In this chapter I will show how spin systems can be manipulated in such a way, that only the contributions of specific interactions with the spin's surrounding become visible.

translated and adapted from: Ned. Tijdschr. Natuurkd. 78 (2012) 152–155

1.1 Solid-state NMR for protons

When it comes to both signal strength and abundance, the proton (the hydrogen nucleus) is the favourite NMR nucleus. A proton in a magnetic field has two quantum states, spin *up* and spin *down*. With increasing field strength the relative population of the *up* state increases, which we observe in the laboratory as a small magnetisation of the solid state material along the field.

With NMR we measure the magnetisation behaviour in time after the application of an rf-field pulse. During the rf-pulse, *up* and *down* states form a collective quantum superposition state with a small net nuclear spin correlation; in a classical picture this can be imagined as a partial alignment of the nuclear spins. This is called the excitation of coherence. In the laboratory we measure after the pulse a rotating, more accurately a precessing, magnetisation around the magnetic field that continues for (milli) seconds. During that time the collective quantum superposition state persists!

The main point is that the frequency of precession is equal to the energy difference between the *up* and *down* state divided by Planck's constant. The influence of the molecular surroundings on the proton changes the energies of the states. Determination of the individual precession frequencies in the overall magnetisation precession, directly provides information about the chemical environment of the protons.

With chemical environment we mean the electron density of the hydrogen atom and the influence of other nuclear spins in the vicinity. Figure 1.1 provides an example of glycine in the solid state. The protons in the (white coloured) hydrogen atoms interact with the electron density of the atom, which is indirectly influenced by the chemical bonds. In figure 1.1 the inter-molecular proton-proton (magnetic dipole-dipole) interactions are indicated with dotted lines. To keep a clear illustration, the intra-molecular proton-proton interactions are not indicated.

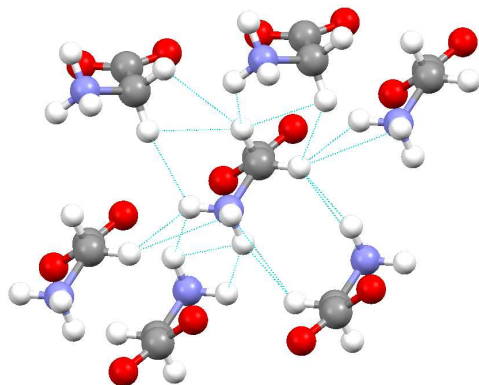


Figure 1.1: A crystal structure of the amino acid glycine (white=hydrogen, red=oxygen, blue=nitrogen, black=carbon) from the Cambridge Structural Database. The dotted lines indicate several inter-molecular proton-proton interactions. Intra-molecular proton-proton interactions are not shown.

Due to the relatively low sensitivity of the NMR technique, there has to be suffi-

cient material to measure enough signal. Solid-state NMR experiments are regularly performed on powders, which are relatively easily obtained in large enough quantities. Here we use glycine as a model system for proton-proton interactions, due to the very strong intra-molecular interaction between the CH_2 protons, see figure 1.1.

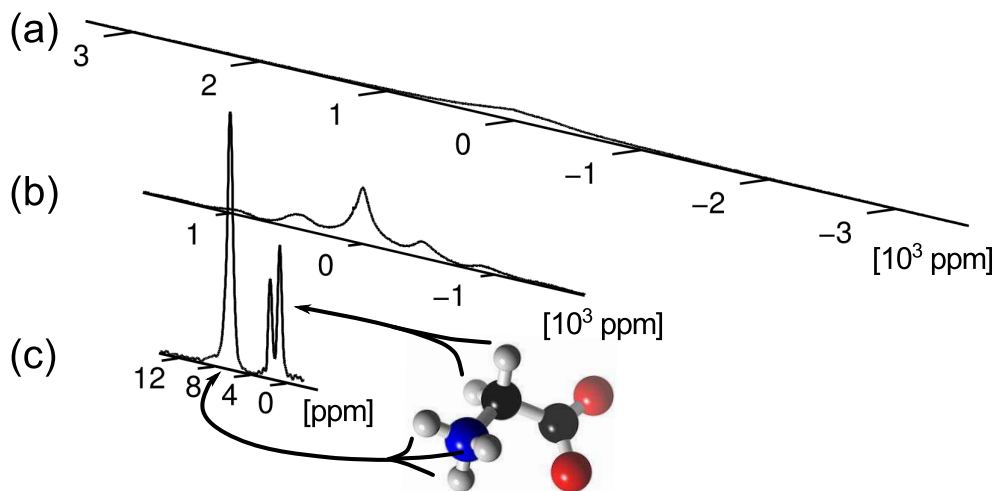


Figure 1.2: (a) Spectrum of glycine in powdered form, the magnetisation precession is measured directly after an rf-pulse. We use a ppm scale to report the position of the peaks independent of the strength of the magnetic field. The precession frequencies scale directly with the magnetic field strength. (b) Same measurement as in (a) but now the material is spinning at 12,500 revolutions per second at the magic angle. (c) Experiment (b) with an optimised rf-pulse shape between the signal acquisition events. The differences in electronic structure surroundings of the protons now become visible.

A measurement of the magnetisation behaviour of glycine in powdered form results in a broad spectrum of precession frequencies, as is shown in figure 1.2(a). This is caused by the angular dependence of the proton-proton interactions, a number of which are indicated with dotted lines in figure 1.1. The energy difference of the *up* and *down* states depends on the angle of the inter-nuclear vector with respect to the external magnetic field. In a powder all orientations are present, so there is a broad range of precession frequencies. The spectrum in figure 1.2(a) does not have any characteristics that provide information about the molecular structure.

1.2 Interaction engineering

Proton-proton interactions (couplings) thus dominate the measured spectra. The typical time scales of NMR, however, allow to manipulate the spin system in such a way that the couplings effectively disappear. As the subtitle of this chapter suggests, we can manipulate both in Euclidean (x,y,z) and nuclear spin (particle states) space. In the first case we physically rotate the material and in the second we use rf-pulses, see figure 1.3.

Nuclear spins are ideal molecular spectators, their states do not change radically by normal chemical and physical processes, and they provide information about the local surroundings at the molecular level. Solid-state NMR is therefore a very useful technique to study materials with for example: disordered structure, proton exchange processes, slowly progressing chemical reactions etc.

Coherences that are created, survive for (milli) seconds. This provides enough opportunities for electronics to perform measurements and manipulations. The precession frequency of a proton in a typical 11.7 Tesla magnetic field is 500 MegaHertz. When this proton is magnetically coupled to a neighbouring proton, this frequency can change maximally about 30 kiloHertz. Because the rf-field has a frequency close to the 500 MegaHertz frequency, the coupled proton sees a rotating rf-field of (maximally) 30 kHz. To effectively manipulate the coupled proton, we have to perform our manipulations within a precession (about 30 microseconds).

This time scale is easily covered by electronics. The shaping of rf-pulses and magnetisation detection in current state-of-the-art NMR spectrometers is possible with respectively 0.2 and 0.125 microseconds. The maximum for mechanical rotation currently lies at a stunning 110,000 revolutions per second!

1.3 Decoupling by rotating the material

The most important dipole-dipole interaction-energy term is proportional to

$$E_{\text{dip.dip.}} \propto \langle 3 \cos^2 \theta - 1 \rangle$$

θ is the angle between the inter-nuclear vectors (dotted lines in figure 1.1) and the external magnetic field. By fast rotation of a material containing protons, the positions of the protons change so quickly, that on average the proton-proton interactions appear to only act along the axis of rotation.

At the magic angle $\theta=54.74^\circ$ the interaction energy given in the boxed equation above is zero; at this angle the dipoles do not experience each others field. In NMR

experiments on solids, the materials are often spun at this angle, see figure 1.3, in order to minimise the proton-proton interactions. See figure 1.2(b) to see the influence of magic angle spinning on the spectrum of glycine.

We can now differentiate NMR of solids from NMR of liquids. In liquids, *e.g.*, glycine dissolved in water, molecules can move freely among each other and rotate around their own axes. The dipole-dipole interaction is therefore a less important interaction in the field of liquid state NMR (except for large molecules). Unfortunately, dissolving solid state materials is not the way to study the molecular structure of the solid state.

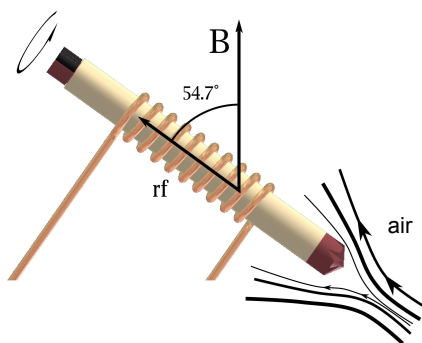


Figure 1.3: Illustration of a material spinner in the rf coil. The spinner contains the material under study and is powered by an air stream. The whole system is at the magic angle with respect to the magnetic field \mathbf{B} .

1.4 Decoupling using rf-pulses

The use of rf-pulses for effectively removing proton-proton couplings is conceptually challenging. With coupling we mean quantum states that interact with each other. In our case this means the *up* and *down* states of two or more protons, that have a magnetic dipole-dipole interaction.

When two protons are close in space, the energies of the *up* and *down* states change, and so do the precession frequencies. Additionally, the states also start a sort of flip-flop motion; when the spin of one proton flips, the same happens to the other proton, but in the opposite direction so that the energy is conserved. To simplify the explanation we change one of the two protons for a fluorine-19 nucleus. Due to the difference in precession frequencies of the two nuclei, the flip-flop motion does not happen here.

The most simple experiment to decouple the proton and fluorine states consists of the application of a constant rf-field resonant with the fluorine nuclear spin. The *up* and *down* states of the fluorine nucleus will now rapidly alternate and the proton will effectively experience no difference between the fluorine states. By measuring at the proton frequency, the decoupling rf-field is not resonant with the proton resonance, we obtain the signal of a proton without interaction with the fluorine.

If we consider the system of two coupled protons, the decoupling approach mentioned above does not work. A resonant rf-field will make both protons rapidly alternate between *up* and *down* states, so they will appear to stand still with respect to each other. Additionally, there is the flip-flop motion of the coupled protons with equal transition frequencies. A suitable rf-field decoupling should therefore be capable of destructively interfering the flip-flop and *up/down* alternation mechanism. This will either require several rf-pulses or a shaped pulse.

Furthermore, in contrast to the previous experiment, the measurement of the proton precession cannot be done at a frequency that differs much from the rf-field frequency. With this in mind, proton-proton decoupling experiments involve measuring between the rf-pulses. When decoupling is efficient, the magnetisation will behave as though there are no proton-proton couplings.

1.5 Real-time pulse optimisation

The description in the previous sections was focused on isolated proton-proton spin systems. In practice protons form a strongly coupled network, as illustrated in figure 1.1. This means the proton precession frequencies are distributed over a broad range, so either magic angle spinning or pulse sequences are not effective enough. Therefore in the state-of-the-art experiments, mechanical rotation is combined with rf-pulses.

The subject of the next chapter is the on-spectrometer optimisation of the rf-pulse shape for this type of experiment. Every measurement of the spectrum of glycine is carried out with a different pulse shape. An evolutionary algorithm (EA) is used to vary the parameters that determine this shape. Figure 1.4 visualises how complicated such a pulse shape can become.

The use of an EA for our purpose has several advantages. EA's optimise a population of trial solutions, which makes it less likely for the algorithm to get trapped in a local optimum, since the information of the entire population is used to generate the next population. EA's can handle a large number of parameters. Furthermore, the only application-specific information needed by the algorithm is a figure of merit for

the quality of the trial solutions. This allows the application to function as a black box.

The result of the approach elaborated on in the next chapter, and the gain of the combined mechanical rotation and the new rf-pulse shape is illustrated in figure 1.2. Moving from the spectrum of figure 1.2(a), via 1.2(b) to 1.2(c), shows an impressive gain in spectral resolution. The result in figure 1.2(c) shows peaks that correspond to the different electronic structure surroundings of the protons in glycine.

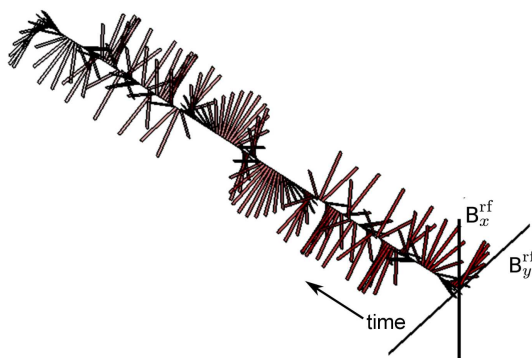


Figure 1.4: Visualisation of a typical rf-pulse shape for the experiments on glycine in the next chapter. Figure 1.3 provides an illustration of a coil that is used to generate such a pulse. The change of the rf-field in time is presented in the rotating frame of the proton. The pulse has a constant amplitude and changing phase.

1.6 Answers and perspectives

In the next chapter a detailed explanation is given of the on-spectrometer optimisation of decoupling pulse-shapes with the use of EA's. Our approach uses as many degrees of freedom as the number of parameters chosen for the pulse shape. This freedom is used to try and answer a research question that was still unanswered in this field of research, namely *Does proton-proton decoupling at very high rf-field work (more) efficiently?* For the particular case of couplings between different nuclear species, for example the fluorine-proton coupling mentioned above, this is known to be true. Experiments will be performed at very high rf-fields that are a factor of 3 or 4 stronger than achievable in conventional NMR setups [2].

CHAPTER 2

EASY-GOING DUMBO on-spectrometer optimisation of phase-modulated homonuclear decoupling sequences in solid-state NMR

A one-step many-parameter optimisation scheme for phase-modulated proton homonuclear decoupling sequences in solid-state NMR is presented. Phase-modulations, parameterised by DUMBO Fourier coefficients, were optimized using a Covariance Matrix Adaptation Evolution Strategies algorithm. Our method, denoted EASY-GOING DUMBO, starts with featureless spectra and optimises proton-proton decoupling, during either proton or carbon signal detection. Optimisations at moderate magic angle spinning (MAS) frequencies and medium radio-frequency (rf) field strengths resulted in solutions closely resembling (e)DUMBO. Application of EASY-GOING DUMBO for optimisation at very high 680 kHz rf field strength, 12.5 kHz MAS on a 400 MHz NMR spectrometer resulted in a new solution, with competitively resolved proton spectra.

adapted from Chem. Phys. Lett. 509 (2011) 186–191

2.1 Introduction

Research on proton homonuclear decoupling in solid state NMR has been receiving considerable attention in the last decade. Contemporary state of the art techniques

are the Combined Rotation And Multiple Pulse Sequence (CRAMPS) methods [3]. These techniques rely on the shaping of radio-frequency (rf) pulses and the interplay between rf cycle and magic angle spinning (MAS) frequencies. This is, considering the capabilities of contemporary NMR spectrometers, a large parameter space. Two categories of approaches to find efficient homonuclear decoupling sequences can be distinguished. The first category can be considered as the 'bottom-up' approach; starting from the theoretical description of the direct dipole-dipole interaction, an averaging scheme is developed. Typical examples are : FSLG [4, 5, 6], PMLG [7, 8, 9] and $RN_n^{N/2}$ [10] sequences. These methods are effective as well as insightful in understanding the process of averaging homonuclear couplings. Their performance for large spin systems and non-ideal rf pulses is, however, difficult to model.

To the second category belong the 'top-down' approaches. These subject the spin system, by numerical simulations (*in silico*) or experimentally (on-spectrometer), to a large variety of pulse shapes to optimise the decoupling efficiency. This encompasses the area of optimal control [11], and the method of greatest relevance to this paper, (e)DUMBO (decoupling using mind-boggling optimisation) [12, 13]. DUMBO is the *in silico* optimisation of phase-modulated homonuclear decoupling pulse shapes, by simulating the response of a coupled homonuclear two-spin system for a range in dipole-dipole couplings and rf field strengths. The DUMBO method produced a pulse shape whose effectiveness competes with and often outperforms the other methods mentioned above. Unfortunately, understanding the exact mechanism behind the resulting phase-modulation is not trivial, as can be expected from a 'top-down' method. DUMBO also has its on-spectrometer implementation named e(xperimental)DUMBO [14], which takes the DUMBO pulse shape as the initial point for a local optimisation, driven by a simplex algorithm. An important advantage of this approach is that the actual spectrometer performance is inherently taken into account. Recently a new version of eDUMBO, named eDUMBO-PLUS [15], was reported for use in the ultra fast MAS regime. Here initial points for local optimisation were found experimentally by a randomised search for well performing phase-modulations.

In this paper we report a method that simplifies eDUMBO by making the optimisation possible in a single step. We explored the use of a Covariance Matrix Adaptation Evolution Strategies (CMA-ES) algorithm [16] (an evolutionary algorithm), known as a robust many-parameter optimiser, for on-spectrometer optimisation. We report our success in reaching convergence in the whole twelve-parameter space spanned by the DUMBO parameterisation. After optimisation, starting from featureless spectra, we confirm the optimal performance of the (e)DUMBO pulse shapes, thereby benchmarking our approach for future work. We chose the adjective EASY-GOING (Evolutionary

Algorithms Serving Your Global Optimisation Improvement Needs Gladly), which emphasises the use of evolutionary algorithms which have a broad range of applications. The current application is therefore denoted EASY-GOING DUMBO (*EGD*).

To determine the agreement of the experimental results with theory, we simulated the experiments for the optimised phase-modulations. The outcomes show that in the current regime of moderate spinning speed and medium rf field strength theory agrees well for these complex pulse shapes. We conclude this paper by presenting our first results for *EGD* decoupling at very high rf field strengths. To achieve this field strength we used a recently presented micro-magic-angle spinning (μ MAS) probehead for application in high-resolution proton solid-state NMR of nanoliter sample volumes [2]. Although this probehead allows the generation of proton rf field strengths of 800 kHz with about 10 W of rf power, we found that the optimal proton spectral resolution is achieved at medium rf field strength when using FSLG and (e)DUMBO. We attributed this effect to rf phase transients that scale with the rf field strength [17]. In this paper we show that our *EGD* approach obtains a pulse sequence that achieves a competitively resolved proton spectrum at very high rf fields.

2.2 Materials and methods

2.2.1 Experiment

^1H and ^{13}C spectra were recorded on a 300 MHz (7.1 T) Varian NMR spectrometer with VNMRs console and a Bruker 2.5 mm double resonance probe tuned to 300.1 and 75.8 MHz, respectively. The samples were spun at 12.5 kHz in 2.5 mm ZrO_2 spinners. [α - ^{13}C , ^{15}N] alanine and [^{15}N] glycine samples were purchased from Sigma-Aldrich and used without further purification. The samples were restricted to volumes of approximately 11 μL , so that they reside well within the coil and rf inhomogeneity effects are limited. Experiments reported at very high rf field strength were performed in a recently presented μ -MAS probehead [2]. We performed these experiments on a 400 MHz (9.4 T) Varian spectrometer under 12.5 kHz MAS, additional settings are shown in table 2.1. Glycine was held in a fused-silica sample container with an outer diameter of 400 μm and an inner diameter of 320 μm with a sample volume of 70 nL.

Figure 2.1(a) shows the pulse sequence to obtain J-resolved ^{13}C spectra. For every new experiment, during the *EGD* optimisation, a new phase-modulated pulse shape is applied while the carbon signal is detected. These experiments were performed on the [α - ^{13}C , ^{15}N] alanine sample, because efficient proton-proton decoupling of alanine's α - ^{13}C CH proton, reveals a doublet caused by the J_{CH} -coupling with the α -carbon. We

used four scans per experiment, and set the length of a phase-modulation block τ_{pmb} , determining the rf cycle time τ_c , to correspond to a 6π pulse. Acquisition on the carbon channel was synchronised with this cycle time. Further experimental settings are shown in the first row of table 2.1.

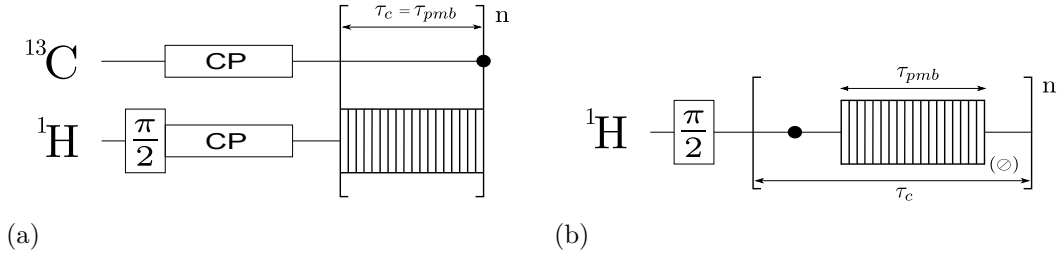


Figure 2.1: (a) Two-channel pulse sequence for assessing the proton homonuclear decoupling performance via carbon detection. The experiment consists of cross polarisation followed by continuous phase-modulation on the proton and acquisition on the carbon channel. The first row in table 2.1 displays settings for the performed carbon detection experiments on the $[\alpha\text{-}^{13}\text{C}, ^{15}\text{N}]$ alanine sample. (b) Single channel pulse sequence employing proton homonuclear decoupling alternated with detection in inserted intervals (windows). \odot indicates super cycling with alternating $[0, \pi]$ phase. The second and third row in table 2.1 show the experimental settings for the reported proton detection experiments on the ^{15}N glycine sample.

Figure 2.1(b) illustrates the pulse sequence for obtaining high-resolution directly detected ^1H spectra. The homonuclear decoupling phase-modulation is applied between the detection windows. This experiment was carried out on glycine. Efficient decoupling will resolve the two lines of the strongly coupled $\alpha\text{-CH}_2$ protons, each with a different chemical shift, making it a reliable indicator of decoupling efficiency. Experimental settings are shown in the second and third row of table 2.1. We used four scans per experiment and define the rf cycle time as the sum of the pulse and detection window durations $\tau_c = \tau_{pmb} + \tau_{win}$.

During the experiment, the phase-modulation is super cycled to create a z-rotation homonuclear decoupling sequence in order to remove zero-frequency contributions from the spectrum without having to optimise an additional pre-pulse prior to the homonuclear decoupling sequence [18]. The orientation of the effective field during the homonuclear decoupling sequence determines the optimal choice of the phase and flip-angle of this pre-pulse to rotate the longitudinal proton magnetisation into a plane

that is perpendicular to the effective field resulting in an artifact-free spectrum [18]. This results in a higher scaling factor for the isotropic chemical shift compared to a super cycled sequence, for example DUMBO-1 has a theoretical scaling factor of 0.52 [12], whereas in the super cycled version this reduces to 0.41. However, we chose super cycling to guarantee spectra without artifacts, since the effective field of the homonuclear decoupling sequence is changing during the optimisation of the DUMBO Fourier coefficients, and hence would in principle require to adjust the pre-pulse in each iteration.

The scaling factor of the chemical shift was determined experimentally, as described in [2]. A series of two-dimensional proton spectra were taken as a function of the rf-field offset. In these experiments, the homonuclear decoupling sequence from figure 2.1(b) is applied during the t_1 evolution, while the proton signal is detected in the t_2 domain without decoupling. This correlates the scaled to the unscaled chemical shift positions. When all 2D data is gathered in one graph, a linear fit through the peak positions is used to correct the scaled spectrum. The axis of the scaled spectrum is divided by the slope of the fit (the scaling factor) and the offset of the fit is subsequently added.

Fig.	sw	ν_{rf}	ν_{off}^{13C}	ν_{off}^{1H}	τ_{pmb}	τ_{res}	τ_{win}	τ_{rd}	τ_{at}
2.4(a)	33.8	101.4	1.0	-1.0	29.6	0.20	–	3.0	30.0
2.5(a)	33.8	140.0	–	0.0	25.6	0.25	4.0	2.0	18.0
2.6	89.3	680.0	–	-2.0	8.8	0.20	2.4	4.0	15.0

Table 2.1: Experimental settings for pulse sequences illustrated in figure 2.1. Settings are related to the figure displaying the experimental data. From left to right: spectral width, nutation and rf field offset frequencies in kHz; phase-modulation block, phase resolution and acquisition window timings in μs , recycle delay in s and acquisition time in ms.

2.2.2 Optimisation strategy

The CMA-ES algorithm

Evolutionary Algorithms (EA's) are based upon the Darwinian theory of a natural selection process occurring by reproduction and mutation of genes in a chromosome leading to only best adapted individuals. The optimisations mentioned in this paper

were performed with an Evolution Strategy (ES) algorithm, a class of EA's, which start with one or a population of parent(s). A parent is a trial solution, that corresponds to a vector of application and strategy parameters. Application parameters are in this case the Fourier coefficients parameterising the phase-modulation. The parent generates offspring in a mutative step-size fashion that depends on the strategy parameters. The fitness (solution performance) of these children is checked and new parents are chosen. There are several different strategies for the generation of the offspring as well as the choice of the next parent(s). For a more detailed description see [19].

For this work, the CMA-ES algorithm developed by Hansen and Ostermeier [16] was used. In this algorithm the mutative steps are dependent on application-parameter covariance which are determined by taking into account the effect of previous mutations on offspring performance. The algorithm is reported reliable for both local optimisation and global optimisation [20]. The CMA-ES algorithm does not leave the choice of strategy parameters open to the user. The only meta-parameters available are parent and offspring population size.

Algorithm – spectrometer interface

An interface was written to link the CMA-ES algorithm, part of the automated fitting program written by Meerts *et al.* [21], to the VNMRJ program controlling the spectrometer.

Optimisation parameters of the phase-modulation were chosen according to the DUMBO parameterisation [12]

$$\varphi(\tau) = \begin{cases} 0 \leq \tau < \frac{1}{2} & : \sum_{n=1}^6 a_n \cos(2\pi n\tau) + b_n \sin(2\pi n\tau), \\ \frac{1}{2} \leq \tau \leq 1 & : \varphi(1 - \tau) + \pi, \end{cases} \quad (2.1)$$

with $\tau = \frac{t}{\tau_{pmc}}$ the phase-modulation progress, and Fourier coefficients a_n and b_n the optimisation parameters in units of 2π . The discretisation of the phase-modulation is determined by the phase resolution τ_{res} , see table 2.1. A phase of π is added in the second half of the phase-modulation to ensure an rf propagator equal to unity at time τ_{pmc} , at which point the spin operator part of the dipole-dipole Hamiltonian should be averaged to zero. The '1 - τ ' argument in this part of the phase-modulation ensures time reversal symmetry to cancel odd order terms in the Magnus expansion [22]; a property used to reduce simulation complexity in the DUMBO approach.

The quality of the spectrum or induction decay is determined by evaluation of the relevant fitness function. Note that fitness needs to be maximised in analogy to the

‘survival of the fittest’ concept. For the proton detection experiment on glycine this function was defined as the path length the transverse magnetisation traveled in the complex plane

$$F = \sum_{n \in \{b+s, \dots, b+ms \leq N\}} |p_n - p_{n-s}|. \quad (2.2)$$

Here is N the number of time-domain datapoints, b the index of the starting datapoint, $\frac{1}{s}$ the fraction of spectral width that is observed for the fitness evaluation, m all positive integer values that match the condition $n < N$, and p_n the n -th complex datapoint. All presented proton detection experiments are optimised with b equal to three and s equal to six.

The fitness function for the carbon detection experiment on alanine was defined as the difference between the average peak intensity of the doublet (α - ^{13}CH J-coupling), and the minimum between the peaks. We will refer to this as the dip-depth between the peaks. To ensure a non-zero feedback for the CMA-ES algorithm at all times, one sixteenth of the maximum spectrum intensity in a pre-set frequency domain was added. For the reported carbon detection experiment the pre-set domain was set to 600 Hz centered at the carrier frequency. This domain was large enough to encompass the width of the expected doublet and to exclude the spectral part not of interest to the optimisation.

Algorithm settings

From the twelve Fourier coefficients in equation 2.1, eleven were allowed to vary from -0.5 to 0.5; the twelfth coefficient could only vary over half of this domain. The latter choice excludes phase-modulations that only differ by an overall sign change. We observed experimentally that the spectrum does not change by applying $-\varphi(\tau)$ instead of $\varphi(\tau)$.

For the CMA-ES algorithm, a population of 48 with 24 parents and 100 generations was found to be a suitable choice for convergence of the twelve parameter problem. Typical optimisation durations were between ten and sixteen hours. Experiments reported here have been done for different random starting populations.

2.2.3 Simulation

All simulations mentioned, were performed using SPINEVOLUTION [23]. The alanine spin system for the carbon detection experiment, nine protons and one carbon nucleus,

was taken from [24] (shown in figure 2.2), and adjusted by addition of a J_{CH} -coupling of 140 Hz for the alpha carbon.

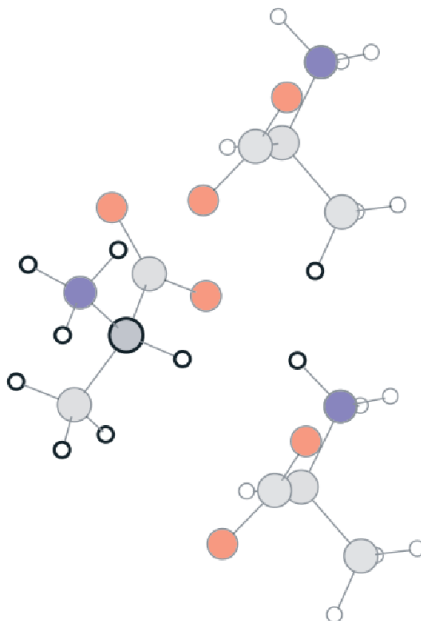


Figure 2.2: Ten spin system, one carbon-13 atom and nine protons, for the alanine simulations. The illustration was taken from [24].

The pulse sequence was matched to the part after CP of figure 2.1(a), hence starting with carbon transverse magnetisation. Furthermore, settings according to section 2.2.1 were used, including rf cycle synchronised detection.

For simulations of the proton detection experiments on glycine, an effective seven-spin system was set up. This was done to reduce the time needed for the calculations, since the unit cell of solid-state glycine contains a large number of protons. Additionally the reduced spin system provides the possibility to perform *in silico* optimisations, these are not presented in this work. Figure 2.3 illustrates what combinations of nuclei were chosen, to form effective spins that mimic the surrounding direct dipole-dipole couplings to neighbouring glycine molecules. An effective spin was created by the summation of the interaction tensors of the grouped spins, and diagonalisation of the resulting interaction tensor to obtain the interaction parameters. The simulation was set up using the experimental settings of section 2.2.1. Simulation started from

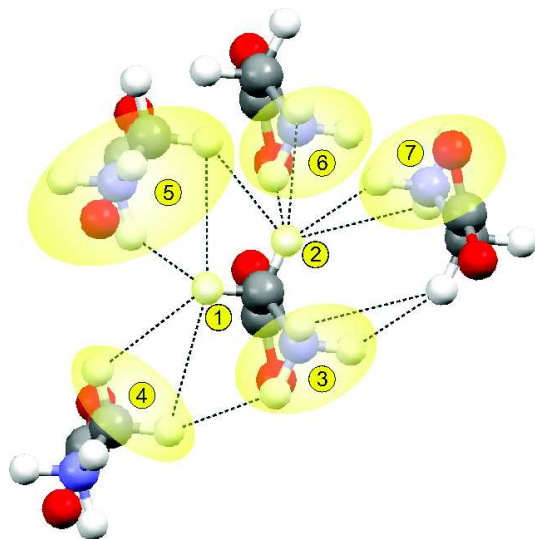


Figure 2.3: Effective seven-spin system for the glycine simulations.

transverse proton magnetisation and included super cycling. The calculated induction decay proved to be invariant to the choice of detection timepoint in the window. For practical reasons, we then synchronised the detection with the rf cycle time.

In both simulations relaxation was not explicitly taken into account. The simulated induction decays were therefore exponentially apodised. Typical calculation times, for a single spectrum, were between seven to ten hours on five 2.5 GHz Opteron cores.

2.3 Results and Discussion

2.3.1 Optimisation of proton homonuclear decoupling during carbon detection

The outcome of *EGD* optimisation of proton homonuclear decoupling detected indirectly via the carbon signal of $[\alpha\text{-}^{13}\text{C},^{15}\text{N}]$ alanine, is shown in figure 2.4(a). For comparison we added eDUMBO-1_{12.5} data, taken with the same experimental settings as mentioned in section 2.2.1.

A comparison of the spectra reveals a better linewidth, but also stronger J-coupling scaling for the *EGD* result, so that the effective resolution is comparable. Full width half height for our pulse shape is 68 Hz, and 94 Hz for the eDUMBO-1_{12.5} data. The obtained phase-modulations are similar, and it is important to note that the phase-

n	Figure 2.4(a)		Figure 2.5(a)		Figure 2.6	
	a_n	b_n	a_n	b_n	a_n	b_n
1	+ 0.01911	+ 0.24799	+ 0.07188	+ 0.13788	- 0.03859	+ 0.25292
2	+ 0.00108	+ 0.15656	+ 0.02961	+ 0.18771	+ 0.08175	+ 0.23386
3	+ 0.01726	+ 0.10816	+ 0.06718	+ 0.01731	+ 0.26925	- 0.15763
4	- 0.02958	+ 0.01289	+ 0.00219	+ 0.12842	- 0.18227	+ 0.25675
5	+ 0.04037	+ 0.08059	+ 0.02404	- 0.04593	+ 0.00595	- 0.10046
6	- 0.03763	- 0.00842	+ 0.04448	+ 0.05531	-	-

Table 2.2: Coefficients, in units of 2π , found by *EGD* decoupling for the carbon and proton detection experiments.

modulation coefficients, see table 2.2, reaffirm the observation by Elena *et al.* [14], that cosine coefficients have a negligible contribution. The compromise between scaling of the J-splitting and the carbon linewidth makes it difficult to determine which phase-modulation performs best. Ultimately, it is the choice of fitness function that determines the outcome. The choice to use the dip-depth of the doublet, appears to be more favourable towards smaller linewidth. Conversely eDUMBO-1_{12.5} is the outcome of using a measure that favours a splitting size equal to the theoretical maximum scaling of 0.57 (for the static-sample case) and maximisation of peak intensities.

Figure 2.4(b) shows how simulation is able to predict the trend in scaling of the J-coupling for the complex eDUMBO and the *EGD* phase-modulations. Apparently the behaviour of the spin system as a result of the complex pulse shapes is near ideal.

2.3.2 Optimisation of proton homonuclear decoupling during windowed proton detection

Figure 2.5(a) shows the resulting spectra for employing *EGD* homonuclear decoupling with windowed acquisition of the proton signal. We experimentally determined a scaling factor of 0.56. Data obtained by the same experimental settings and the DUMBO phase-modulation is displayed in the figure for comparison.

Comparison of the phase-modulations shows small deviations, which translate into small differences of the spectra. It is remarkable that our *EGD* phase-modulation is so similar to DUMBO, which is obtained *in silico* for a two-spin system. This may be considered as a benchmarking of our method, as discussed below.

Figure 2.5(b) shows simulation results. We scaled the simulated spectra with the experimental scaling factors. The peak positions for the CH₂ peaks are reproduced.

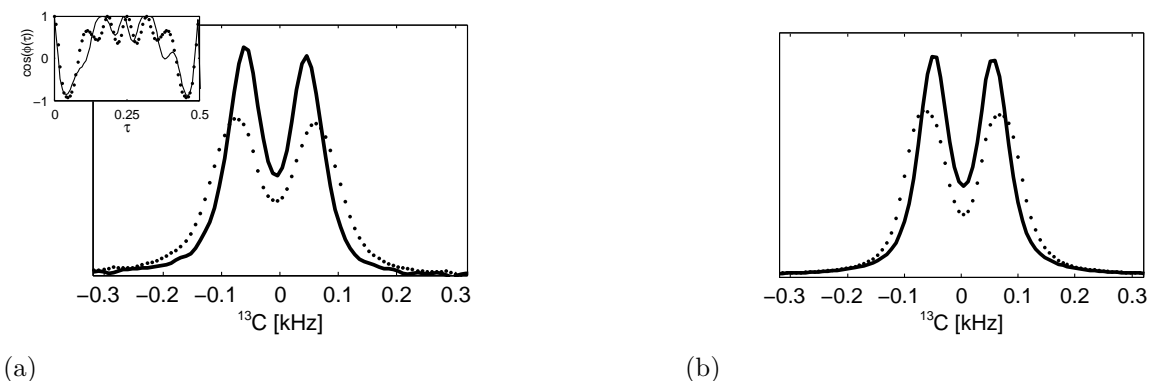


Figure 2.4: (a) Outcome of *EGD* proton homonuclear decoupling (continuous line) for the carbon detection experiment on $[\alpha\text{-}^{13}\text{C},^{15}\text{N}]$ alanine. The spectrum, caused by the $\alpha\text{-}^{13}\text{CH}$ J-coupling, and phase-modulation are compared to eDUMBO-1_{12.5} data (dotted line). Experimental linewidths at FWHH are $\Delta(CH)=68$ and 94 Hz respectively. Phase-modulations are shown in the inset, based on the coefficients in table 2.2 and [14]. (b) Simulation results for the experiment of figure 2.4(a). A spin system consisting of nine protons and one carbon nucleus was used. Simulated induction decays were apodised to match the experiment.

With the use of the experimental scaling factors for chemical shift correction, a nearly one-to-one mapping of experiment and theory is obtained. Chemical shift values for spin number one, two and three in figure 2.3 were determined from the scaled spectrum in figure 2.5(a). It is remarkable that theory can correctly predict the different outcomes of slightly distinguishable pulse shapes, regarding the possibility of pulse shape imperfections in the experiment and the presence of detection windows in the pulse sequence.

The fitness function used for this optimisation seems to be a quite 'natural' choice, no incorporation of unphysical weighting factors to maximise scaling and minimise linewidth. The path length of the magnetisation in the complex plane becomes longer with increasing dephasing time and the presence of higher or more frequencies. Additionally this fitness function is more generally applicable, since it is independent of the number of peaks.

Unfortunately, this fitness function proved to be impractical for optimisation of the proton rf offset. The optimisation will maximise the offset, since that will result in induction decays with faster oscillations. We also applied this fitness function (b equal to three and s equal to five) for the carbon detection experiment. The resulting spectrum was a singlet. This can be understood by the significantly different dephasing

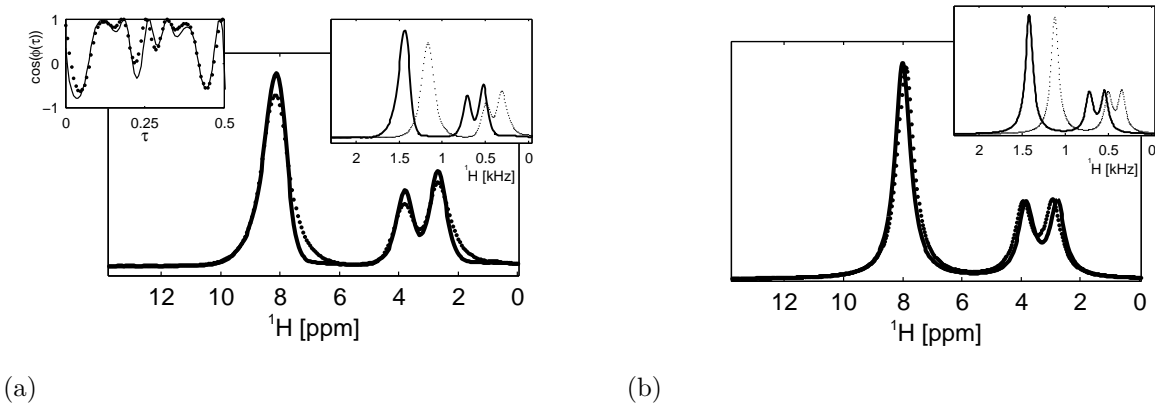


Figure 2.5: (a) Results for the proton detection experiment on $[^{15}\text{N}]$ glycine. Comparison between *EGD* (continuous line) and DUMBO phase-modulations and spectra before (inset upper right corner) and after correction for chemical shift scaling (main window). Experimental unscaled linewidths at FWHH are $\Delta(\text{NH}_3^+)_{\text{raw}}=160, 176$ Hz and $\Delta(\text{CH}_2)_{\text{raw}}=112, 128$ Hz and scaled $\Delta(\text{NH}_3^+)_{\text{real}}=0.95, 1.12$ ppm and $\Delta(\text{CH}_2)_{\text{real}}=0.67, 0.76$ ppm respectively. Phase-modulations, shown in the upper left inset, are based on the coefficients in table 2.2 and [12]. (b) Simulation of spectra in figure 2.5(a). The effective spin system is illustrated in figure 2.3. Simulated induction decays are apodised to match the experimental data.

times for an uncoupled and a J-coupled carbon nucleus.

2.3.3 Convergence to (e)DUMBO solutions

Figures 2.4(a) and 2.5(a) show that the *EGD* optimisation results at moderate rf field strength resemble those of (e)DUMBO. Especially the results for the proton detection experiment are remarkable; two completely different approaches converge to the same result. We find, viewing the carbon spectra, that the definition of the fitness function can steer the optimisation towards lesser scaling or linewidth. *EGD* experiments performed by us with other fitness functions, for both carbon and proton detection experiments, confirm this observation. From this point of view, the path length fitness function for the proton detection experiment, is a translation of the purely theoretical DUMBO quality measure, into experimental parameters. This is important due to the fact that DUMBO’s quality measure is designed for minimising the multi-spin (couplings) and maximising single-spin operator coefficients, an ideal definition for a single-objective (one fitness) optimisation. By the latter statement we would like to

refer to the possibility of performing a multi-objective optimisation [25], where the incommensurability of the two objectives can be studied in a more objective sense.

The same search space has been explored by different methods, both *in silico* and on-spectrometer, resulting in similar optima, accepting a difference in measures of quality. This suggests that the one-step *EGD* scheme successfully managed to navigate the twelve parameter search space.

2.3.4 EASY-GOING DUMBO optimisations at 680 kHz rf field strength

In this section we demonstrate that the *EGD* method is not strongly dependent on the initial choice of parameters, by applying it to new experimental conditions. For this purpose we employed *EGD* homonuclear decoupling at very high rf fields of 680 kHz using our recently presented μ MAS setup [2] for high resolution proton NMR. The solenoid coil that generated the strong rf field has an inner diameter of 450 μ m and a Q-factor of 45.

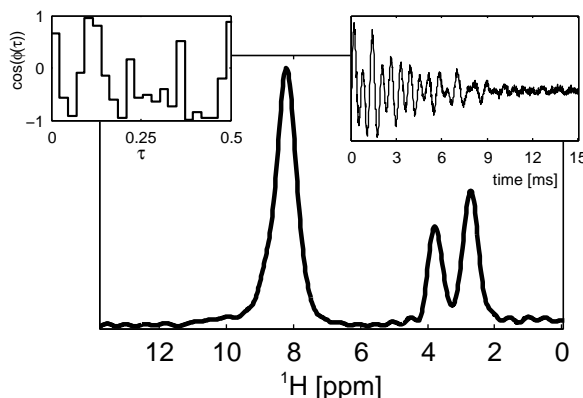


Figure 2.6: Optimisation outcome for *EGD* proton homonuclear decoupling direct detection experiment at 680 kHz rf field strength, 12.5 kHz MAS on a 400 MHz Varian spectrometer. The phase-modulation, coefficients are shown in table 2.2, is presented in the inset as stairs to indicate the small number of phase steps that was used. The experimental spectrum is shown in the main window and its induction decay in the upper right inset. The chemical shift scale of the spectrum was corrected with a scaling factor of 0.32. Experimental unscaled linewidths at FWHH are $\Delta(NH_3^+)_{raw}=93$ Hz and $\Delta(CH_2)_{raw}=65$ Hz and scaled $\Delta(NH_3^+)_{real}=0.73$ ppm and $\Delta(CH_2)_{real}=0.51$ ppm respectively.

For the experimental conditions mentioned in section 2.2.1, we determined that the

DUMBO phase-modulation does not resolve glycine’s CH₂ peaks. Figure 2.6 shows the outcome of the *EGD* proton detection experiment at 680 kHz rf field strength. Note that we are applying 12π pulses to ensure the ratio $\frac{\tau_{pmb}}{\tau_{res}}$, equal to 44 in this case, does not become so small that no freedom of choice for the phases is left.

A value of 0.32 was estimated for the experimental scaling factor of the resulting homonuclear decoupling sequence. Although this scaling is unfavourable, there is a considerable improvement in the linewidth compared to the results depicted in figure 2.5(a), exceeding 0.1 ppm. For comparison we tabulated our results together with results for several different direct proton detection methods for homonuclear decoupling in table 2.3. This table shows that the unscaled linewidth in Hz for the CH₂ protons obtained in this work compares very favourably to the results published so far. For a well-ordered crystalline compound this line width should be dominated by residual proton-proton dipolar interactions which are efficiently suppressed by *EGD* at high rf field strength which is remarkable, considering the fact that the spectra were obtained under moderate 12.5 kHz MAS on a 400 MHz spectrometer. Unfortunately our scaling factor is unfavourable but still results in a competitive effective resolution as compared to the other methods summarized in table 2.3. We therefore anticipate better resolution for *EGD* when implemented at higher external magnetic fields. It certainly encourages further investigation of the potential of very high rf field homonuclear decoupling at higher external fields and/or spinning speeds.

ref.	seq. name	ν_r [kHz]	ν_{rf} [kHz]	ν_{1H} [MHz]	λ	Δ_{real} [ppm]	Δ_{real} [Hz]	Δ_{raw} [Hz]
[15]	PLUS-1	65	170	500	0.73	0.33	165	120
[26]	DUMBO-1	65	170	500	0.47	0.47	230	108
[27]	wPMLG5 _{mm} ^{x̄}	10	99	600	0.47	0.47	282	133
[28]	TIMES	10	170	900	0.35	0.6	550	192
this work	DUMBO-1	12.5	140	300	0.56	0.76	229	128
this work	EASY-GOING DUMBO	12.5	140	300	0.56	0.67	200	112
this work	EASY-GOING DUMBO	12.5	680	400	0.32	0.51	203	65

Table 2.3: Comparison of experimental parameters and linewidths of the CH₂ resonances for different direct proton detection schemes, including our very high rf field results. All resonances are from glycine except for [15] that used β-L-Asp-L-Ala. From [28] we determined the line width by hand. Columns from left to right represent: reference, sequence name, MAS and rf nutation frequency, main magnetic field strength, scaling factor and respectively the scaled linewidth in ppm and Hz, and the unscaled linewidth in Hz.

From numerical simulations (not shown) we obtained a scaling factor of 0.22 which does not match the experimental value. We are not certain what causes this difference. Super cycling is able to compensate effects from phase transient that can be described by z-rotations [18]. However, our results indicate that this description might no longer be sufficient at high rf fields. Further research is needed to elucidate these effects.

2.4 Conclusions

We presented the benchmarking and, furthermore, successful application of our one-step EASY-GOING DUMBO phase-modulated homonuclear decoupling optimisation scheme at 12.5 kHz MAS conditions. Starting from a random set of phase-modulations and featureless spectra we managed to optimise to effective decoupling solutions. Optimisation of proton-proton decoupling at medium rf field strength, for both direct proton and indirect carbon detection schemes, reaffirm the optimal performance of (e)DUMBO, thereby benchmarking our method. Simulations of both experiments reproduce the experimental scaling factors, which shows that theory can distinguish between the influences of slightly differing pulse shapes. We end the paper with results for EASY-GOING DUMBO optimisation at 680 kHz of rf field strength and 12.5 kHz MAS on a 400 MHz NMR spectrometer. The optimisation resulted in a new pulse shape that provides a competitive spectral resolution, given relatively low MAS and main field requirements. In this case, simulation could not reproduce the scaling factor, for which we do not yet have a sound explanation, given that super cycling should compensate for pulse transients. We consider the results at very high rf field strength encouraging for further investigations of the potential of very high rf field homonuclear decoupling.

Acknowledgements

We thank Prof. Dr. Wim J. van der Zande for his chivalrous support of this project. Technicians Jan van Os and Gerrit Janssen are thanked for experimental help as are Dave Rice and Vadim Zorin from Varian Inc. The Netherlands Organisation for Scientific Research (NWO) and Radboud University Nijmegen are acknowledged for their financial support of the solid-state NMR facility for advanced material science.

3.1 Quadrupolar nuclei

The atomic nucleus is a composite particle consisting of protons and neutrons, referred to as nucleons. Nucleons themselves consist of elementary particles named quarks. Properties of the nucleus emerge from the intrinsic properties of its constituent particles, *e.g.* spin and charge, combined with their orbital motion. The total nuclear angular momentum that results from the coupling of the particles' spin and orbital angular momentum, is what is commonly referred to as nuclear spin with quantum number I [30].

Most of the NMR active nuclei have nuclear spin $I \geq 1$, a few examples are shown in table 3.1. Note that in a magnetic field the number of energy levels of these nuclei is $2I+1$ (labelled by magnetic quantum number $M_I = -I, -I+1, \dots, I$), this means we no longer consider a two-level spin system as was the case for the (uncoupled) protons in the previous chapters. The shape or charge distribution of the nucleus is related to the nuclear spin quantum number I . From a basic angular momentum theory treatment of the multipole expansion describing the interaction between the nucleus and the

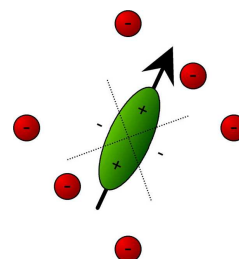


Figure 3.1: Impression of the quadrupolar charge distribution surrounded by point charges representing the local structure of the chemical site [29].

electromagnetic field, follows that the highest electric multipole moment of the nucleus is of rank $2I$ [30]. Odd rank multipole moments, such as the electric dipole moment, are not present due to a parity conservation law from nuclear physics [31].

Consequently in addition to a magnetic interaction of the nucleus with the magnetic field, the nucleus may also have an anisotropic electrostatic interaction with its surroundings. In practice the most important contribution is that of the quadrupole moment of the nucleus, that interacts with the electric field gradient of the surrounding charge distribution. An impression of this interaction is given in Fig. 3.1.

Spin	Isotopic species (natural abundance)					
1	² D (0.02%)	⁶ Li (7.42%)	¹⁴ N (99.63%)			
3/2	⁷ Li (92.85%)	⁹ Be (100.00%)	¹¹ B (80.42%)	²³ Na (100.00%)	⁸⁷ Rb (27.85%)	
5/2	¹⁷ O (0.04%)	²⁷ Al (100.00%)	⁵⁵ Mn (100.00%)	⁸⁵ Rb (72.15%)	¹²⁷ I (100.00%)	
7/2	⁴³ Ca (0.15%)	⁴⁹ Ti (5.51%)	⁵¹ V (99.79%)	⁵⁹ Co (100.00%)	¹³³ Cs (100.00%)	

Table 3.1: Several isotopes with a nuclear quadrupole moment and their natural abundance (www.webelements.com).

3.2 Interaction parameters and local structure

The quadrupolar interaction is parameterised with the quadrupolar coupling constant C_q and asymmetry parameter η . The expression for the interaction in its principal axis frame (PAF) is given by

$$\hat{H}_Q^{PAF} = \frac{2\pi C_q}{4I(2I-1)} \left\{ 3\hat{I}_Z^2 - \hat{I}^2 + \eta(\hat{I}_X^2 - \hat{I}_Y^2) \right\}, \quad (3.1)$$

with \hat{I} the nuclear spin operator. Further explanations of Eq. 3.1 are given in section 4.2.1. The focus of this section is the relation of these parameters to the structure of a chemical site (nuclear spin atomic surroundings). Chapters 4 and 5 will then be concerned with the quantification of these parameters by fitting experimental spectra.

Fig. 3.2 relates C_q to several atomic coordination structures of a central atom with quadrupolar nucleus. For systems considered by NMR, the quadrupolar coupling constant is typically of the order of several MHz. C_q is directly proportional to the quadrupole moment of the nucleus, and the largest principal axes component of the electric field gradient tensor at the position of the nucleus. It therefore quantifies

the strength of the interaction. On the left in Fig. 3.2 are symmetrical coordination structures for which the electric field gradient at the nucleus cancels, hence $C_q \approx 0$ MHz. These are from top to bottom: cubic, octahedral and tetrahedral. Moving further to the right this cancellation is more and more lifted, leading to an increase of the field gradient experienced by the nucleus.

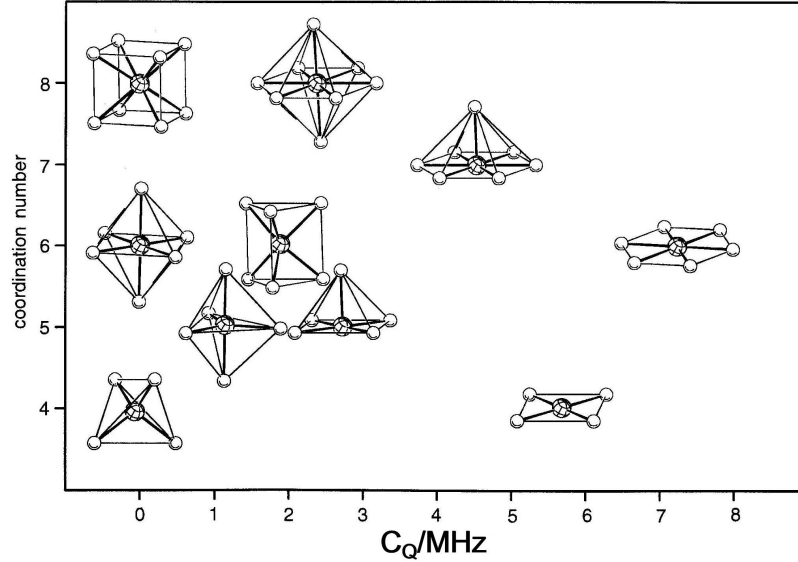


Figure 3.2: Relation between the quadrupolar coupling constant C_q and coordination structures of a central atom with a quadrupolar nucleus [29].

The second interaction parameter η is a measure for the asymmetry of the electric field gradient, the definition is given in equation 4.4. It may take values ranging from 0 to 1. The $\eta = 0$ case is the prolate limiting case of the principal components of the electric field gradient. There is cylindrical symmetry in the gradient. An example of such a structure is the coordination most to the right in Fig. 3.2 with all charges surrounding the central atom set equal. The $\eta = 1$ case is the oblate limiting case of the principal components of the electric field gradient. Also here there is cylindrical symmetry, but one principal component is equal to zero, leading to a planar field gradient. An example of such a structure is again the most right coordination in Fig. 3.2, but with three neighbouring charges changed in sign.

3.3 Quadrupolar interaction as a perturbation

As was explained in the first chapter, the NMR spectrum effectively summarises the nuclear spin precession frequencies present after coherence-excitation of the nuclei. These frequencies depend on the energy differences between the nuclear spin levels. In the strong magnetic fields (> 6 Tesla) used in NMR experiments, the Zeeman interaction between the nuclear spins and the magnetic field dominates for the cases relevant to this work. The quadrupolar interaction may then be treated as a perturbation.

Fig. 3.3 presents the energy level diagram for a quadrupolar nucleus with spin $5/2$ in an external magnetic field. From left to right the shift in energy of the levels is illustrated, starting with the Zeeman interaction H_Z followed by the first and second order perturbation H_Q^1 and H_Q^2 of the quadrupolar interaction. The angular frequency ω_Q is defined as

$$\omega_Q = \frac{6\pi C_q}{2I(2I - 1)}. \quad (3.2)$$

It is important to note that the energy difference between levels with the same value for $|M_I|$ remain unchanged by the first order shift of the quadrupolar interaction. This has significant consequences for the range of precession frequencies (width of the spectral lines) present in the spectrum. To illustrate this, Fig. 3.4 shows a ^{23}Na ($I = 3/2$) spectrum of powdered NaNO_3 for which both the central $|M_I = 1/2\rangle \leftrightarrow |M_I = -1/2\rangle$ transition and the satellite transitions $|M_I = \pm 3/2\rangle \leftrightarrow |M_I = \pm 1/2\rangle$ are present. It is ultimately the anisotropy of the quadrupolar interaction combined with the sum over all crystallite orientations that is responsible for the typical shape. The central transition is the sharp line in the middle, while the wide lines at the base are the satellite transitions for which the precession frequencies are determined by the first order shift. The exceptionally small value for C_q of 337 kHz of the sodium chemical site resulted in all $2I$ transitions (1 central, 2 satellites) to appear fully in this spectrum.

From this point on only the central transitions will be considered, since for larger values of C_q the satellite lines become too broad for proper excitation and significant spectral intensity contribution. To conclude, for integer I nuclei there is no central transition, all transitions for these nuclei are broadened by the anisotropy of the first order perturbation in Fig. 3.3. The rest of this introduction therefore is concerned with half integer spin nuclei.

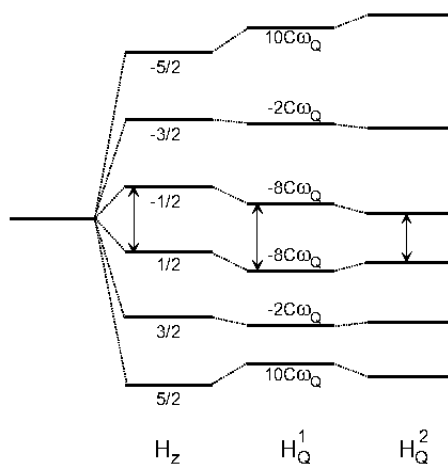


Figure 3.3: The energy level diagram for a nucleus with spin $I=5/2$ [29]. The dominating Zeeman interaction H_z is directly proportional to the magnetic field strength. Subsequently the energy levels are shifted by a first H_Q^1 and second H_Q^2 order perturbation due to the quadrupolar interaction. Note that the symmetric transitions $|M_I\rangle \leftrightarrow | -M_I\rangle$ are not broadened by the first order shifts.

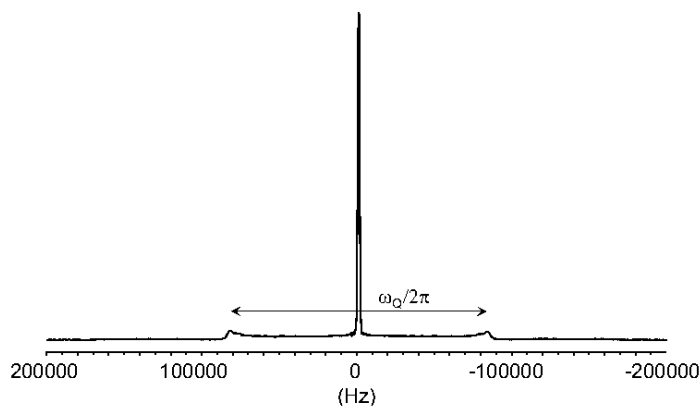


Figure 3.4: The ^{23}Na spectrum of powdered NaNO_3 . Both central $|M_I = 1/2\rangle \leftrightarrow |M_I = -1/2\rangle$ (sharp peak) and satellite $|M_I = \pm 3/2\rangle \leftrightarrow |M_I = \pm 1/2\rangle$ (broad line shape at the spectrum basis) transitions are visible. Adapted from [29].

3.4 Typical line shapes

This section is concerned with spectral lines that correspond to the central transition (second order quadrupolar interaction), as discussed in the previous section. Fig. 3.5 illustrates typical powder line shapes for different values of the quadrupolar interaction parameters. Powders are often used in solid-state NMR experiments as they are more readily available and provide enough signal (contain enough spins). In this figure the spectrum of a static (non-rotating) spin-system is given.

The difference between Figs. 3.5(a) and 3.5(b) shows that C_q determines the width of the spectral lines, while η characterises the shape. Notice that the centre of gravity of the spectral lines in both Figs 3.5(a) and 3.5(b) are shifted from zero. This is caused by the isotropic part of the quadrupolar interaction called the quadrupolar induced shift.

As was discussed in the first chapter, interaction anisotropy may be removed from the spectrum by spatial averaging. In the case of the quadrupolar interaction, magic angle spinning (MAS) can only partly reduce the line widths in the spectra, since the interaction contains higher order angular dependent terms. In second order perturbation theory of the quadrupolar interaction (Fig. 3.3), the precession frequencies for the central transition of the quadrupolar nuclei are given by the expression used in chapter 5

$$\nu_{M_I=-1/2 \rightarrow M_I=1/2} = \nu_{iso} + C_0^{I, M_I=1/2} \nu_{qis} + C_4^{I, M_I=1/2} \nu_4(\alpha, \beta). \quad (3.3)$$

Here ν_{iso} is the isotropic chemical shift, the $C_0^{I, M_I=1/2} \nu_{qis}$ essentially determines the quadrupolar induced shift, and $C_4^{I, M_I=1/2} \nu_4(\alpha, \beta)$ is the only anisotropic term left after complete spatial averaging by MAS. Additional removal of the latter contribution to the spectrum will be the subject of section 3.6.

Simulations of the line shapes of the spin system of Fig. 3.5(b) under MAS conditions are given in Fig. 3.6. Here Fig. 3.6(a) shows how incomplete averaging by MAS introduces spinning side bands in the spectrum. These side bands are separated from the central line shape in multiples of the MAS frequency, as the signal is modulated with this frequency. If the spatial averaging is complete (fast enough MAS) only the central shape remains as is shown in Fig. 3.6(b).

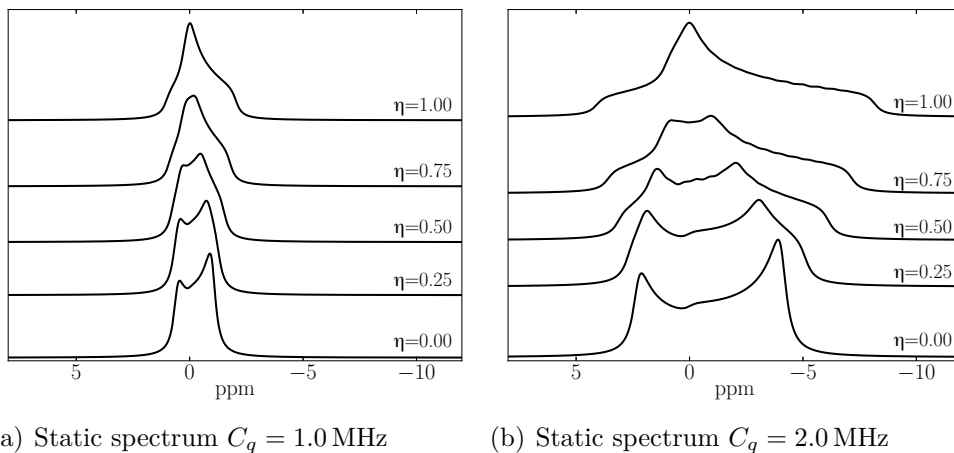


Figure 3.5: Static spectral line shapes of the central transition of a nucleus with $I = 3/2$ in a magnetic field of 500 MHz ^1H frequency as a function of η . (a) $C_q = 1.0$ MHz and (b) $C_q = 2.0$ MHz. Spectra were simulated using SIMPSON [32].

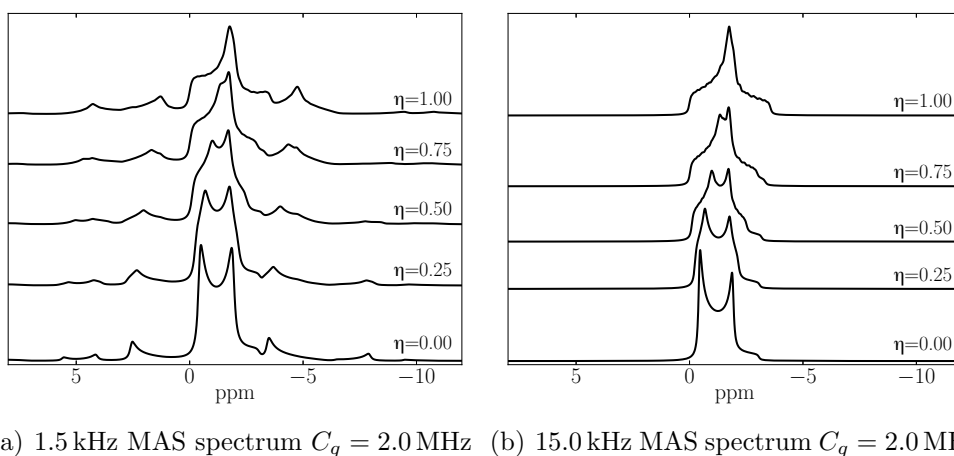


Figure 3.6: Spectra of Fig. 3.5(b) at two MAS speeds. (a) 1.5 kHz MAS, incomplete spatial averaging leads to spinning side bands on both sides of the central line shape. (b) 15 kHz MAS, complete averaging leads to a line shape for which the precession frequencies present are determined by Eq. 3.3. Spectra were simulated using SIMPSON [32].

3.5 Excitation of quadrupolar nuclei

Quadrupolar nuclei are inherently multi-level quantum systems ($2I + 1$ levels, with $I \geq 1$). The application of an rf-pulse to the nucleus leads to a complex excitation of (multi-quantum) coherences between the nuclear spin levels. This complicates the extraction of quantitative information from experimental data, the subject of chapters 4 and 5, such as relative chemical site abundances and quadrupolar interaction parameters.

Fig. 3.7 presents simulated signal intensities for the central transition of an $I = 5/2$ nucleus, after excitation by an rf-pulse with length τ_p and strength $\omega_{rf} = |\gamma B_1/2|$. Each curve corresponds to a different ratio of ω_Q (Eq. 3.2) and ω_{rf} [29]. The signal intensity is a function of the dimensionless pulse flip-angle; the angle over which the magnetisation of a spin half nucleus would rotate due to the rf-pulse [31]. This figure reveals that the signal differs substantially for different interaction strengths ω_Q . From this it follows that the relative abundance of different chemical sites in a material is not necessarily reflected by their spectral intensity! This observation will receive more attention in chapters 4 and 5.

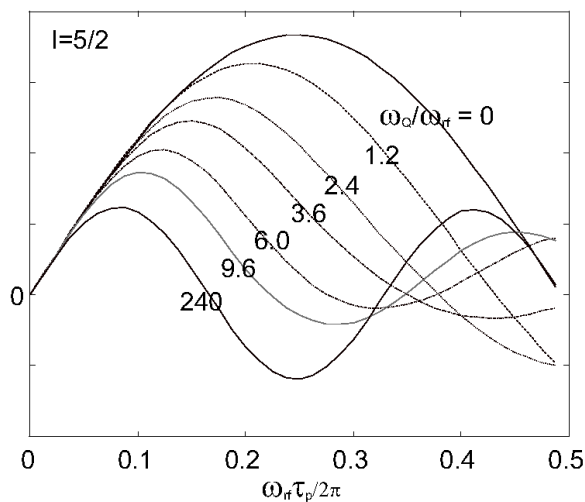


Figure 3.7: Signal intensity for spin 5/2 nucleus (powder) as a function of pulse flip-angle. The curves correspond to different ratios (ω_Q/ω_{rf}) of quadrupolar interaction and rf-field strength [29].

What may additionally be deduced from Fig. 3.7 is the excitation behaviour for the non selective ($\omega_1 \gg \omega_Q$) and selective ($\omega_1 \ll \omega_Q$) excitation regime. In both regimes

the excitation curve simplifies to a sine function. For the rf-dominated non-selective excitation regime, the time dependence of the signal intensity becomes proportional to $\sin(\omega_1\tau)$, while for the quadrupolar interaction dominated selective excitation regime this becomes $\sin([I + \frac{1}{2}]\omega_1\tau)$. Both regimes have a different signal amplitude.

In the intermediate regime of $\omega_1 \approx \omega_Q$ both the rf-field and quadrupolar interaction determine the response of the spin system. This leads to a complex excitation behaviour. Fig. 3.7, however, illustrates that all quadrupolar interaction strengths have the same linear excitation behaviour for small pulse flip-angles. In order to remain in this linear regime, the experimentalist has the opportunity to choose a set of τ_p and ω_{rf} .

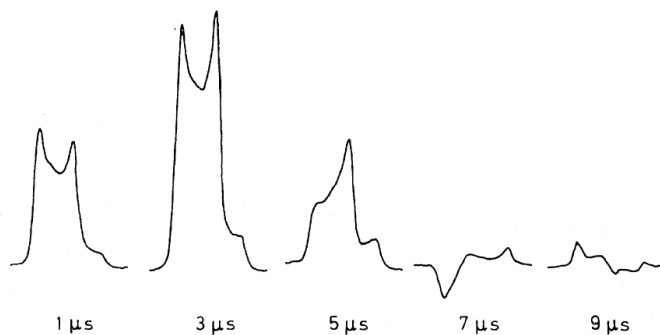


Figure 3.8: Experimental ^{55}Mn ($I = 5/2$) MAS spectra of KMnO_4 as a function of τ_p and $\omega_{rf}/2\pi = 48$ kHz. The interaction parameters are $C_q = 1.6$ MHz and $\eta = 0$. Figure is adapted from [33].

In practice ω_{rf} should be chosen sufficiently large to excite the whole line shape, which provides an upper bound for τ_p . Short pulses, however, result in a relatively large loss of potential signal, as follows from Fig. 3.7. Depending on the capabilities of the spectrometer and the strength of the quadrupolar interaction, this trade-off may result in a distorted line shape as illustrated in Fig. 3.8. The latter provides an example of the potential difficulties of obtaining accurate interaction parameters via the line shape.

3.6 Multiple Quantum Magic Angle Spinning

In section 3.4 the typical MAS line shapes for the quadrupolar interaction were discussed. These line shapes are related to the anisotropic term in Eq. 3.3 and cannot be removed from the spectrum by rotation at the magic angle. Although the line shape contains information about the quadrupolar interaction, it may also hide information about interactions of smaller magnitude, such as the chemical shift (nuclear spin - electron density interaction), or the presence of multiple chemical sites as shown in Fig. 3.9. The figure provides a good example of the need for ways to remove the remaining interaction anisotropy, to obtain the information that there are actually four sites underneath.

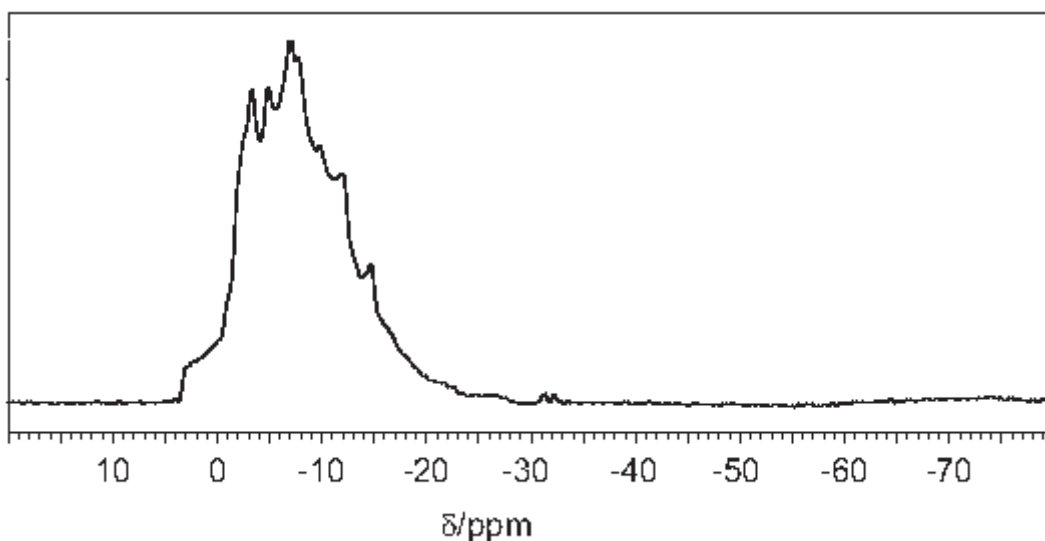


Figure 3.9: ^{23}Na MAS spectrum of $\text{Na}_4\text{P}_2\text{O}_7$. This spectrum consists of the overlapping spectra of four different ^{23}Na sites. Figure is adapted from [34].

Spatial averaging of the third term in Eq. 3.3, requires rotation of the spin system at the angle of 70.12 or 30.56 degrees in addition to MAS. This is feasible in a double rotation experiment, one rotor spinning inside another rotor, but it is relatively difficult to realise [35]. Another solution is to perform a multiple-quantum magic angle spinning (MQMAS) experiment [36]. This two-dimensional NMR experiment basically exploits the fact that the interaction anisotropy is accurately described by this one anisotropy term, for all symmetric (between states of equal $|M_I|$) coherences. For example the

symmetric triple quantum coherence frequencies in the F1 dimension are given by

$$\nu_{M_I=-3/2 \rightarrow M_I=3/2} = \nu_{iso} + C_0^{I, M_I=3/2} \nu_{qis} + C_4^{I, M_I=3/2} \nu_4(\alpha, \beta). \quad (3.4)$$

With the mathematical manipulation, called shearing, Eqs. 3.3 and 3.4 can be subtracted

$$\nu' = \nu_{M_I=-3/2 \rightarrow M_I=3/2} - \frac{C_4^{I, M_I=3/2}}{C_4^{I, M_I=1/2}} \nu_{M_I=-1/2 \rightarrow M_I=1/2}, \quad (3.5)$$

to obtain a new frequency coordinate free of the anisotropic term labelled the F1' dimension.

In practice this manipulation should be performed on experimental data in which a symmetric multiple-quantum-coherence is correlated to the single-quantum-coherence of the central transition. This data is obtained from an MQMAS experiment, elaborated on in chapter 5, with the pulse sequence as illustrated in Fig. 3.10. The sequence starts with an rf-pulse with optimised length and strength to excite a maximum triple-quantum-coherence, in this particular case. Subsequently a delay is incremented followed by a pulse that converts the multiple-quantum coherence to the measurable single-quantum-coherence.

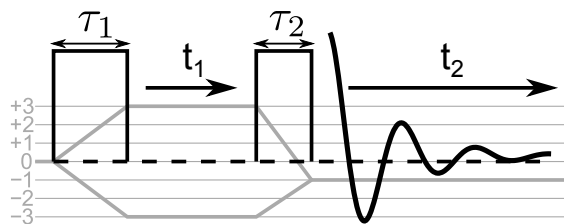


Figure 3.10: 3QMAS sequence, indirect t_1 and direct (signal acquisition) t_2 dimension are shown in black, with coherence pathways in grey. The two pulses of length τ_1 and τ_2 provide triple-quantum-coherence excitation and conversion, respectively. See also chapter 5.

Note that with ideal excitation and conversion, the MAS line shape is obtained in the direct dimension. The efficiency of excitation of quadrupolar nuclei is, however, a complex matter as was discussed in section 3.5. That is why accurate simulations of the spectra are required. Chapter 5 will be dedicated to the quantitative analysis of MQMAS spectra.

Fig 3.11(a) illustrates a simulated MQMAS spectrum, the Fourier transform of the data collected with the pulse sequence of Fig. 3.10. Both spectral dimensions have the anisotropic line shape (except for the width), visible in the projections in the figure.

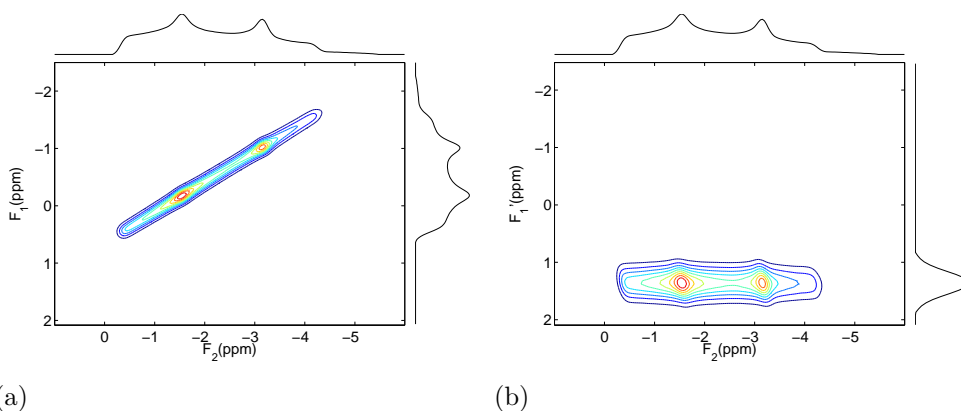


Figure 3.11: Illustration of the effect of the shearing transformation, revealing from the experimental data of (a) the isotropic spectrum in the $F1'$ dimension in (b). The projections are sum-projections.

Fig 3.11(b) shows the data of Fig 3.11(a) after the shearing transformation, that introduces the new frequency coordinate $F1'$. The spectral line shape in this dimension is a simple peak that is only determined by the isotropic part of the interaction.

To conclude, Fig. 3.12 shows the sheared 3QMAS spectrum of $\text{Na}_4\text{P}_2\text{O}_7$ of which the MAS spectrum is shown in Fig. 3.9 [34]. This two-dimensional spectrum has resolved lines, in contrast to the MAS spectrum of Fig. 3.9, that show the presence of four distinct chemical sites.

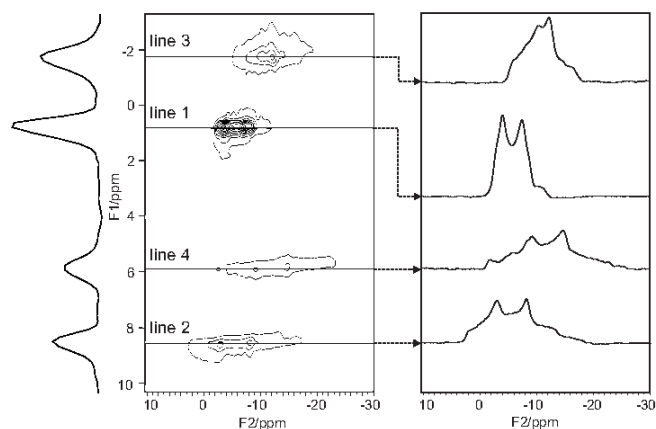


Figure 3.12: ^{23}Na 3QMAS spectrum of $\text{Na}_4\text{P}_2\text{O}_7$ [34]. The four ^{23}Na sites, which all overlapped in the MAS spectrum of Fig. 3.9, are now resolved. From left to right: the projection of the $F1'$ dimension, contours of the spectral lines, and slices through the spectrum.

CHAPTER 4

EASY-GOING deconvolution: Combining accurate simulation and evolutionary algorithms for fast deconvolution of solid-state quadrupolar NMR spectra

A fast and accurate fit program is presented for deconvolution of one-dimensional solid-state quadrupolar NMR spectra of powdered materials. Computational costs of the synthesis of theoretical spectra are reduced by the use of libraries containing simulated time/frequency domain data. These libraries are calculated once and with the use of second-party simulation software readily available in the NMR community, to ensure a maximum flexibility and accuracy with respect to experimental conditions. *EASY-GOING deconvolution* (*EGdeconv*) is equipped with evolutionary algorithms that provide robust many-parameter fitting and offers efficient parallelised computing. The program supports quantification of relative chemical site abundances and (dis)order in the solid-state by incorporation of (extended) Czjzek and order parameter models. To illustrate *EGdeconv*'s current capabilities, we provide three case studies. Given the program's simple concept it allows a straightforward extension to include other NMR interactions. The program is available *as is* for 64-bit Linux operating systems.

J. Magn. Reson. 211 (2011) 114-120

4.1 Introduction

Quadrupolar nuclear magnetic resonance is a valuable tool in materials research. The technique applies to atomic nuclei that possess a total angular momentum ≥ 1 and thereby a quadrupolar moment [37]. This concerns over two-thirds of the NMR active nuclei, hence the area of application for quadrupolar NMR is potentially large. Solid-state NMR techniques help to study the interaction between the quadrupolar moment of nuclear charge and the electrical field gradient (*efg*) generated by the chemical surroundings; the microscopic system of a nucleus and its surroundings is known as a site. The nucleus thereby acts as a probe for local structure, which typically extends over several coordination spheres [38]. This makes quadrupolar NMR a particularly sensitive technique for structural information from (partly) disordered solid-state materials, e.g. glasses, semiconductors and polymers, for example materials that cannot be studied by X-ray techniques due to their lack of long range order.

Structural information contained in the experimental spectra can be extracted by deconvolution in terms of quadrupolar interaction parameters and relative abundances of different sites. This requires a deconvolution model, which accurately describes the experiment and spin system at reasonable computational costs. Fitting programs such as DMFit [39] and QuadFit [40] have their own dedicated model, which is optimised towards low costs, but not versatility in terms of experimental conditions. Conversely, there are general purpose NMR simulation programs such as SIMPSON [32] or SPINEVOLUTION [23], that are versatile in their capabilities to mimic experimental conditions and varying spin systems, but miss dedication for spectrum fitting. In practise the quality of simulations of quadrupolar NMR spectra is mostly restrained by computational costs, for example due to the need for orientational averaging of crystallites for powder spectra. With this in mind we created a separation between the computationally intensive simulations and the actual data-fitting, by the use of second-party software, in the work presented here SIMPSON, to pre-calculate time or frequency domain libraries that are subsequently used during the fitting procedure. This approach allows, as for example in the case of $\text{Al}_{0.5}\text{Ga}_{0.5}\text{As}$ (discussed below), the calculation of a five-site spectrum, all sites with a quadrupolar parameter distribution, in less than a second on a single 2.3 GHz processor core.

A second requirement for spectrum deconvolution is the choice of a suitable algorithm to the fitting of parameters. If the experimental spectrum contains spectral lines of multiple sites that are not well resolved, the deconvolution model becomes more complex and the number of fit parameters increases. To our knowledge, only one NMR fitting program [41] is able to handle this many parameters, by the use of genetic

algorithms. In combination with SIMPSON, this program was used to fit spectra of Vanadium nuclei in haloperoxidases. It, however, is not readily available, and does not separate the fitting from the time consuming simulation step. We introduce the use of evolutionary algorithms [21], of which genetic algorithms are a sub-class, in the *EGdeconv* program. The additional advantage of these algorithms is that they can be efficiently parallelised, leading to an increased computation speed. Typical convergence rates involve 100 iterations with a population of 30 trial-solutions. Assuming the case of $\text{Al}_{0.5}\text{Ga}_{0.5}\text{As}$ (discussed below), this amounts to 35 minutes for a typical spectrum deconvolution. This calculation time is further reduced by the use of the parallelised code on all available cores (and processors).

Deconvolution of spectra from (partially) disordered materials requires accounting for distributions in interaction parameters, for example by variations in bond angles and/or distances. For the quadrupolar interaction this corresponds to retrieval of the distribution in quadrupolar coupling constant and asymmetry parameter. Czjzek *et al.* [42] were able to determine the shape of such a distribution for random ordering. By calculating the *efg* tensor components for a large number of random repositionings of surrounding charges, they determined that the components are normally distributed. Starting from this multivariate Gaussian distribution of the five independent *efg* tensor components, they could analytically derive a probability density function for the quadrupolar interaction parameters. Le Caër *et al.* [43, 44] extended this model to express the probability density function for a microscopic system with an ordered short-range and disordered long-range surroundings.

Underlying structural variations influence the shape of spectral lines. Deconvolution of the experimental spectrum assisted by these models provides a way to indicate and possibly quantify structural disorder. Currently Quadfit [40] allows the use of the Czjzek model for data-fitting, but no fit-programs are readily available that apply the extended model. Complementary to the microscopic Czjzek model, there is a more macroscopic approach to quantify (dis)order that fixes the relative site abundances given a crystal structure. This fixed set of abundances is related to an order parameter [38, 45], of which the value can be varied to range from disordered structure to a targeted crystal structure. Fitting this parameter provides an indication of the material's structure.

The remainder of this paper will describe the *EASY-GOING* (Evolutionary Algorithms Serving Your Global Optimisation Improvement Needs Gladly) *deconvolution* program, of which the name emphasises its relation to EASY-GOING DUMBO homo-nuclear decoupling [1], that used parts of the same program. We will briefly cover required theory, discuss evolutionary algorithms and the program structure, followed

by three case studies and finish with the program's technicalities. In order to learn how to use the program, the reader is referred to the up-to-date manual that is supplied together with the program and example input files at <http://egdeconv.science.ru.nl>.

4.2 Theory

4.2.1 The nuclear quadrupolar interaction

Atomic nuclei that have total angular momentum ≥ 1 , possess a none-spherical charge distribution and consequently an electric quadrupolar moment [37]. The Hamiltonian, in units of angular frequency, for the interaction of this moment of the nuclear charge distribution with the *efg* of the environment is given by [23, 46]

$$\hat{H}_Q = \sum_i \frac{2\pi C_q^i}{2I_i(2I_i - 1)} \hat{I}_i \cdot \tilde{\mathbf{V}}^i \cdot \hat{I}_i. \quad (4.1)$$

Here i is the index of the quadrupolar nuclei and \hat{I}_i and I_i the nuclear angular momentum vector operator and its quantum number. Furthermore, the reduced *efg* tensor $\tilde{\mathbf{V}}^i$ equals \mathbf{V}^i divided by its largest principal component, by definition, V_{ZZ} . C_q^i is the quadrupolar coupling constant. The general form of \mathbf{V} and C_q is

$$C_q = \frac{eQV_{ZZ}}{h} \quad \text{and} \quad V_{\alpha,\beta} = \left. \frac{\partial^2 V}{\partial r_\alpha \partial r_\beta} \right|_{r=0}, \quad (4.2)$$

with V the electric potential at the position of the nucleus, r_α its coordinates for $\alpha=x, y, z$ and eQ the nuclear quadrupolar moment. From the form of equations 4.1 and 4.2, it follows that C_q determines the strength of the coupling and additionally provides limits for the position of transition frequencies and, for powdered materials, the width of the spectral lines. For illustrative purposes we rewrite equation 4.1 for the case of a single quadrupolar nucleus in the principal axis frame (PAF) of the *efg* tensor [46]

$$\hat{H}_Q^{PAF} = \frac{2\pi C_q}{4I(2I - 1)} \left\{ 3\hat{I}_Z^2 - \hat{I}^2 + \eta(\hat{I}_X^2 - \hat{I}_Y^2) \right\}. \quad (4.3)$$

Here the asymmetry parameter η is defined as

$$\eta = \frac{V_{XX} - V_{YY}}{V_{ZZ}}. \quad (4.4)$$

It provides symmetry information of the *efg* at the nucleus. The asymmetry parameter can assume values between zero and one, adhering the convention $|V_{ZZ}| \geq |V_{YY}| \geq |V_{XX}|$. Combined with the requirement for a traceless *efg* tensor, the quadrupolar interaction is fully described with C_q and η as parameters.

The dominating Zeeman interaction in NMR makes the form of equations 4.1 and 4.3 impractical. Advanced theory for a convenient perturbation treatment of the quadrupolar interaction under magic angle spinning and radio-frequency pulse conditions is extensively treated in literature [32, 23, 46]. To conclude, it should be noted that the explicit angular dependence of the equations in this section is deliberately not shown. In simulations, the response of the powder is assumed equal to the sum of all crystallite responses. This sum will therefore include all crystallite orientations present, leaving only C_q and η to parameterise the induction decay/spectrum.

4.2.2 Parameter constraints

Reproducing data by fitting does not always lead to a better understanding of the underlying physics. Essentially the more parameters are involved the more degrees of freedom are available to provide a high quality fit. It is therefore important to search for parameter constraints. These may be obtained from other experimental data, physical limits etc. *EGdeconv* provides many ways to constrain or couple parameters, which is partly shown below and fully documented in the manual. Another possibility is to impose constraints via (physical) models, as will be introduced in the next two sections.

(Extended) Czjzek distribution

One of the subtleties is that the use of quadrupolar NMR to study disordered materials, is the experimental spectrum effectively comprises all local structure variations felt by the type of nucleus under study. The challenge in the analysis is thus to find an inverse mapping of experimental data in terms of structural information, which will in most cases be non-linear. By starting from the notion that structural variations translate into a distribution of the *efg*, a more accessible step is to find the form of this distribution.

Czjzek *et al* [42] investigated the *efg* distribution in the case of structural disorder by computer simulations. Tensor components of the *efg* at the center of randomly repositioned charges, become normally distributed in the limit towards infinite samplings. The resulting probability distribution, as a function of *efg* tensor components, is therefore a multivariate Gaussian. This distribution can be rewritten as a proba-

bility density function of quadrupolar interaction parameters C_q and η , which has the closed-form

$$f(C_q, \eta) = \frac{C_q^{d-1} \eta}{\sqrt{2\pi} \sigma^d} \left(1 - \frac{\eta^2}{9}\right) \exp\left\{-\frac{C_q^2}{2\sigma^2} \left(1 + \frac{\eta^2}{3}\right)\right\}. \quad (4.5)$$

Here σ is the standard deviation of the multivariate Gaussian probability distribution of the *efg* tensor components and d is introduced to correspond to the number of independent tensor components [38]. Normalisation of the distribution integral to one, provides the probability of finding a given set of C_q and η . Later the Czjzek model was revisited and extended by Le Caër and Brand [43, 44]. They introduced an ordered (not distributed) contribution to the *efg*, for example originating from a fixed well-defined first coordination sphere. In the *EGdeconv* program we implemented the most general form of the resulting probability density function, given by

$$\begin{aligned} f(C_q, \eta) \propto & \frac{C_q^{d-1}}{\sigma^d} \eta \left(1 - \frac{\eta^2}{9}\right) \iiint d\alpha \sin(\beta) d\beta d\gamma \\ & \times \exp\left\{-\frac{1}{2\sigma^2} \left[C_{q,o}^2 \left(1 + \frac{\eta_o^2}{3}\right) + C_q^2 \left(1 + \frac{\eta^2}{3}\right) \right. \right. \\ & \left. \left. - \frac{2}{\sqrt{3}} C_q C_{q,o} \left(\sqrt{3} a_{11} + \eta_o a_{15} + \eta \left(a_{51} + \frac{\eta_o a_{55}}{\sqrt{3}} \right) \right) \right] \right\}. \end{aligned} \quad (4.6)$$

Here $C_{q,o}$ and η_o are quadrupolar parameters for the local order contribution. The elements a_{ij} contain the angular dependence of the *efg* tensor components, as defined in [43] and the *EGdeconv* manual. Integration over all angles leaves a distribution as function of quadrupolar interaction parameters that encompasses short-range order and long-range disorder.

Order parameter models

In this section we briefly introduce the idea of an order parameter model by treating one specific example. For a more elaborate description we refer to the manual.

In structural investigations of materials, an order parameter is generally introduced to have a measure for the presence of long-range order. This measure is related to the fractional occupation of lattice sites by their preferred atom. While *EGdeconv* has the versatility to couple various parameters and thus allows the implementation of various

order parameter models, we have explicitly implemented Copper-Gold and Copper-Platinum ordering in $A_xB_{1-x}C$ systems as encountered in III-V semiconductors. We immediately introduce the form of the equations for Copper-Gold ordering, meaning a limit to order of alternating $\langle 001 \rangle$ planes of A and B atom species

$$\begin{aligned}
 p_{C[B_4]} &= (1 - r_A)^2 r_B^2 \\
 p_{C[AB_3]} &= 2r_A(1 - r_A)r_B^2 + 2(1 - r_B)(1 - r_A)^2 r_B \\
 p_{C[A_2B_2]} &= r_A^2 r_B^2 + (1 - r_B)^2 (1 - r_A)^2 \\
 &\quad + 4r_A(1 - r_B)r_B(1 - r_A) \\
 p_{C[A_3B]} &= 2r_A^2(1 - r_B)r_B + 2r_A(1 - r_B)^2(1 - r_A) \\
 p_{C[A_4]} &= (1 - r_B)^2 r_A^2.
 \end{aligned} \tag{4.7}$$

The left hand side corresponds to the probability of occurrence for the specific tetrahedral site. The variable r_A is the fractional occupation number of A atoms present in the correct plane according to the pre-determined order; therefore $1 - r_A$ is the fraction of not-A atoms present in the same plane. The first equality for $p_{C[B_4]}$ gives the probability of finding a C atom coordinated by four B atoms. With respect to the Copper-Gold ordered structure this corresponds to two B atoms present in a ‘correct’ and two in an ‘incorrect’ plane. By defining $r_A = x + \frac{1}{2}S$ and $r_B = 1 - x + \frac{1}{2}S$ we introduce the order parameter S . Changing S from zero to a maximum of $2x$ converts disorder to the maximally achievable Copper-Gold ordering.

4.3 Evolutionary algorithms

Evolutionary Algorithms (EA’s) are based upon the Darwinian theory of a natural selection process occurring by reproduction and mutation of genes in a chromosome leading to only best adapted individuals. In our case, direct translation of these concepts is achieved by accepting vectors with fit parameters as chromosomes and the discrepancy between experimental and theoretical spectrum as selection criterion. EA’s propagate/optimize typically a population of initially, randomly chosen trial solutions in their vector representation. This population-based character, inherently provides more information on search space structure, partly accounts for their global optimisation capabilities. Ultimately it is the algorithm’s mechanism to exploit this search space information that accounts for optimisation performance. *EGdeconv* currently provides the use of three different evolutionary algorithms: a genetic [47], derandomised 2 evolution strategies (DR2-ES) [48] and covariance matrix adaptation evolution strategies (CMA-ES) algorithm [16].

The genetic algorithm includes recombination via parameter vector cross-over's and applies point mutations to a small part of the population. Evolution strategies algorithms only use overall mutations, the stepsize and direction are determined by strategy parameters. For the DR2-ES algorithm, the mutative steps are determined on inherited strategy parameters from successful parent vectors. The CMA-ES algorithm in addition incorporates parameter covariance information to generate trial solutions. For more in-depth information on the algorithms, we refer to the manual and references given in this section.

4.4 *EASY-GOING deconvolution* program structure

Here we provide the reader with a brief overview of the program flow, for a more elaborate treatment we refer to the manual at <http://egdeconv.science.ru.nl>. After starting the *EGdeconv* program from the Linux command line, the input file is parsed and the libraries are read into the computer memory. Obviously the amount of computer memory provides a limit to the grid size and resolution of the library, however, *EGdeconv* provides several ways to avoid this limit, for example: by ensuring a library is only present once in the memory, or by allowing to choose the $[\eta, C_q]$ grid taken from the library or number of data points read per file. Subsequently the selected EA generates parameter vectors that are translated into theoretical spectra. These trial spectra are rated by comparing the experiment to the theory by evaluation of a cost function. There are multiple cost functions defined in *EGdeconv*, for example the use of a weighted innerproduct between the theoretical and experimental spectrum vectors. The EA effectively performs the above in an iterative fashion to reach convergence.

A theoretical spectrum is the sum of subspectra of which each corresponds to a parameter set in the input file and hence a specific chemical site. The program flow to calculate a subspectrum is illustrated in Fig. 4.1.

The figure illustrates in what order the selected library files are processed, and where the various fitting parameters are used. First step is summation of the files according to the distribution model chosen. Then depending on the type of data, time or frequency domain, the result requires additional processing in the form of apodisation and a Fourier transform. Subsequently the intensity of the subspectrum is determined either freely or according to an order parameter model. It is possible to apply a zeroth and first order phase correction to the subspectrum or to use the absolute or absolute squared value of the spectrum. The program flow is ended by positioning the subspectrum. Note that the number of fit parameters per subspectrum can vary between one and

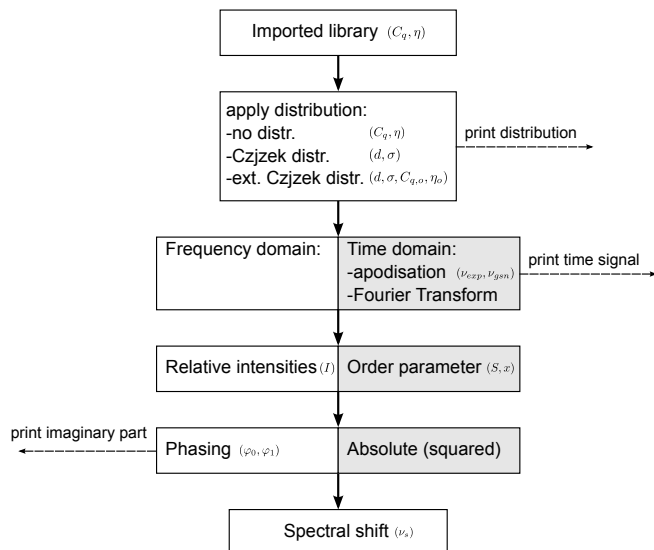


Figure 4.1: Program flow of *EGdeconv* for the calculation of a subspectrum. The grey-white blocks indicate the choices the user has in its synthesis. For each step, parameters that can be included in the fit are indicated. The definition of part of the parameters (d , σ , $\eta_{(o)}$, $C_{q,(o)}$, x and S) can be found in the Theory section. The exponential/Gaussian apodisation (ν_{exp}/ν_{gsn}) and zeroth and first order phasing (φ_0, φ_1) are defined in the manual, leaving only the trivial parameters chemical shift (ν_s) and intensity (I).

effectively ten at maximum. Whether or not *EGdeconv* will converge depends on a number of factors, for example: the parameter correlations, unique features in the experimental spectrum and of course the accuracy of the simulated library files.

Fig. 4.1 also illustrates that *EGdeconv* can print extra output. This feature provides the user with more insight in what happens during the different stages in the calculation. The amount of output is governed by appropriately setting keywords in the input file.

4.5 Examples

In this section three applications of the *EGdeconv* program are presented. They represent the program's versatility, by the use of second-party software, in this work SIMPSON [32], to handle different experimental conditions, for example: static or magic angle spinning (MAS), free induction decay or Hahn echo acquisition etc. Additionally, we show lineshape analysis with or without (extended) Czjzek distributions. Input files for these examples are provided with the installation package.

4.5.1 ^{27}Al MAS NMR spectrum of Yttrium Aluminium Garnet

Fig. 4.2 shows a hard pulse ^{27}Al MAS NMR spectrum of YAG ($\text{Y}_3\text{Al}_5\text{O}_{12}$) at 15 kHz MAS. YAG has a garnet type structure with Al occurring in a tetrahedral and an octahedral coordination in 3:2 ratio. The spectrum of powdered YAG was measured and fully characterised by Massiot *et al.* in 1990 [49]. Combination of MAS conditions and the well-defined quadrupolar interactions, indicated by the sharp lineshapes, make this a suitable benchmark study for *EGdeconv*. Massiot *et al.* established interaction constants for the tetrahedrally ($\sim 6\text{MHz}$, $\eta=0$) and octahedrally ($\sim 0.6\text{MHz}$, $\eta=0$) coordinated sites with a relative abundance ($\sim 3:2$). Given the results mentioned in the caption of Fig. 4.2, *EGdeconv* efficiently reaffirmed these findings.

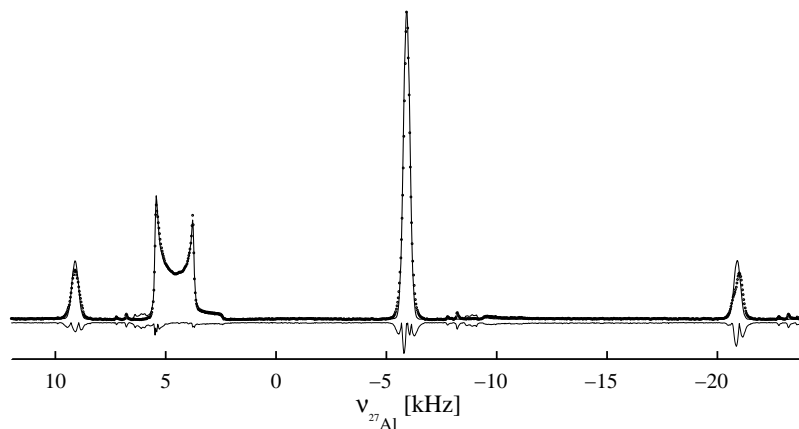


Figure 4.2: Experimental (dotted line) and theoretical (continuous line) ^{27}Al spectrum of YAG together with the negative absolute value of the difference. The spectrum consists of a broad resonance of the tetrahedral site in addition to two spinning side bands and the central transition of the octahedral site. Five independent fits with $[\eta(\text{start:step:end})-C_q(\text{start:step:end})]$ grids $[0.00:0.01:0.10-5.0:0.1:7.0]$ and $[0.00:0.01:0.10-0.3:0.1:1.0]$ obtained C_q values of 6.1 and 0.6 MHz and η values of 0.04 and 0.07 ± 0.02 , respectively, only standard deviations larger than the library stepsize are noted. The relative intensity of the respective sites, was determined 1 : (0.69 ± 0.01) .

4.5.2 Oxidation of Sodium Aluminium Hydride (NaAlH_4)

Fig. 4.3 shows the results of fitting ^{27}Al MAS spectra of NaAlH_4 's oxidation process as a function of time. All information provided here is based on [50] that contains references and more details about the data analysis. The NaAlH_4 sites in the material have

a well defined lattice without significant variations. When exposed to air, structurally disordered tetrahedrally and octahedrally coordinated oxide sites will form. From Multiple Quantum MAS experiments it was determined that the quadrupolar interaction of the tetrahedral (Al(IV)) site is distributed. Therefore the lineshape of this site was fitted with a Czjzek distribution that reproduces the asymmetric lineshape, as shown in Fig. 4.3. The octahedral site (Al(VI)) contained in addition to a distribution in quadrupolar parameters also line broadening from dipole-dipole couplings, this influence was mimicked by additional line broadening. As the NaAlH_4 has a well-defined crystal structure this line was described without a distribution in quadrupole parameters. Additional Gaussian line broadening accounted for the dipolar broadening as the spectra were obtained without proton decoupling.

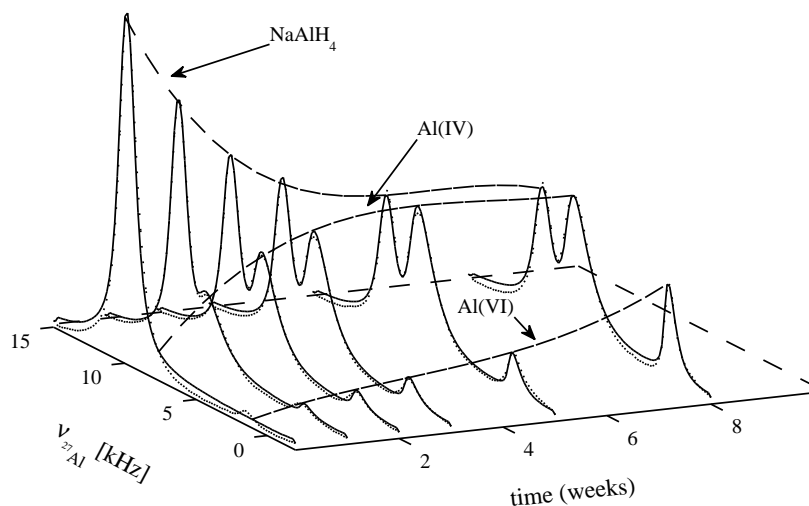


Figure 4.3: Oxidation of NaAlH_4 as a function of time. Experimental (dotted line) and theoretical spectra (continuous line) are overlaid and shown as a function of time. The dashed lines roughly connecting the peaks are qualitative guides to the eye. They emphasize the conversion of NaAlH_4 in tetrahedral Al(IV) and octahedral Al(VI) oxide sites. For the fits a $[\eta(\text{start}:\text{step}:\text{end})-C_q(\text{start}:\text{step}:\text{end})]$ grid of $[0.00:0.05:1.00-0.5:0.5:15.0]$ was used.

The aim of the spectral deconvolution here was to quantify the relative intensities of the various lines as a function of time. This allows to monitor the interconversion of the different components during oxidation as shown in Fig. 4.3, and discussed in detail in [50].

4.5.3 Static Hahn echo spectrum of Aluminium Gallium Arsenide

Fig. 4.4 shows a ^{75}As Hahn echo spectrum of powdered $\text{Al}_{0.489}\text{Ga}_{0.511}\text{As}$, one form of the widely used and well-characterised AlGaAs semi-conductor. Solid-state NMR was used to investigate the possible order or disorder in the occupation of the Al/Ga sites. The analysis of this spectrum is published in [38] and was the main driving force behind the development of *EGdeconv*.

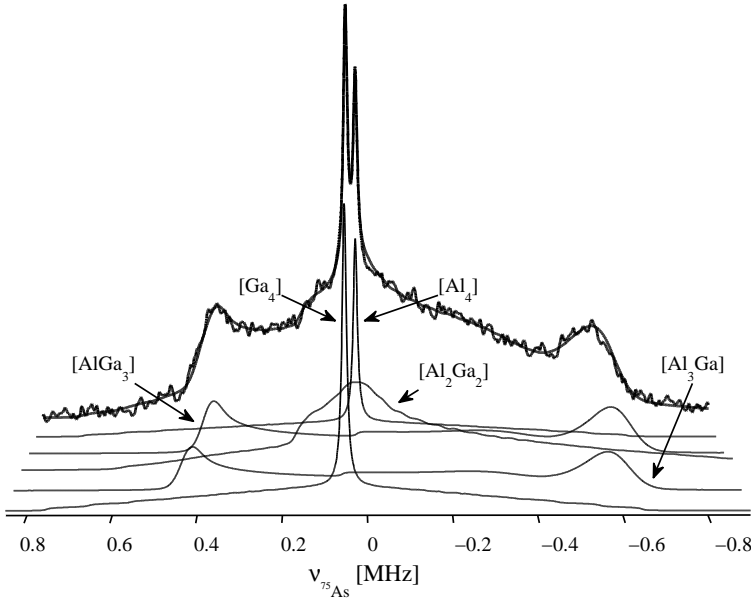


Figure 4.4: Experimental (thick dotted line) and theoretical (thick continuous line) Hahn echo spectrum of $\text{Al}_{0.489}\text{Ga}_{0.511}\text{As}$, deconvoluted in terms of subspectra corresponding to tetrahedral aluminium-gallium sites. The $[\text{Al}_4]$ and $[\text{Ga}_4]$ sites were fitted with a Czjzek distribution, the remaining sites required an extended Czjzek distribution to account for the ordered *efg* contribution in the first coordination sphere. Subspectrum intensities were fitted with respect to one subspectrum, but independently. Three libraries with $[\eta(\text{start:step:end})-C_q(\text{start:step:end})]$ grids of $[0.00:0.05:1.00-0.0:0.2:3.2]$ ($[\text{Al}_4]$ and $[\text{Ga}_4]$), $[0.00:0.01:0.10-31.0:0.1:35.0]$ ($[\text{Al}_3\text{Ga}]$ and $[\text{AlGa}_3]$) and $[0.85:0.01:1.00-28.0:0.1:35.0]$ ($[\text{Al}_2\text{Ga}_2]$) were used.

With a spectral width of 2.5 MHz and sites with small and large quadrupolar coupling constants present, this example is particularly dependent on accurately simulated excitation efficiencies. As the figure shows, the spectrum can be decomposed in terms of tetrahedral aluminium-gallium coordinations of the arsenic atoms. The centered

narrow lines correspond to the $[Al_4]$ and $[Ga_4]$ coordinations of the arsenic atoms, these sites have such a high symmetry that the efg due to the first atomic coordination shell is zero, leading to a small quadrupolar interaction strength caused by disorder in the higher coordination spheres. With respect to excitation efficiencies it should be noted that for these sites both central and satellite transitions are of importance. Due to a negligible efg contribution of the first atom coordination shell, these sites are specific probes of disorder in higher order coordination spheres. This justifies the use of a Czjzek distribution to calculate the lineshapes.

The symmetry of the remaining three sites causes a large efg contribution from the first coordination shell. The excitation efficiency of these sites is mainly selective to the central $\langle \frac{1}{2}, -\frac{1}{2} \rangle$ transition. To fit these sites an extended Czjzek distribution was applied, for which the σ parameter was set to the average of the $[Al_4]$ and $[Ga_4]$ Czjzek distribution, since the latter are probes for long range disorder. The last step in the analysis is the use of an order parameter to relate the site intensities. The resulting fit, shown in [38] and available in the installation package, matches less than that of Fig.4.4, but provides a value of S close to zero, indicating the expected structural disorder. An in-depth study of this disorder supported by DFT calculations reproducing the fitted distributions is described in [38].

4.6 Conclusions and outlook

We presented *EASY-GOING deconvolution*, a program for fast and accurate fitting of one-dimensional solid-state quadrupolar NMR spectra of powdered materials. The use of second-party software to calculate libraries as a function of quadrupolar parameters allows accurate simulation of the experiment and a low computational cost for theoretical spectrum synthesis during the fitting. This furthermore allows a straightforward extension of the program to fit other NMR interactions, such as chemical shift anisotropy and combinations thereof. The program is provided for 64-bit Linux operating systems and supports efficient parallel computing due to the nature of the incorporated evolutionary algorithms that can handle many-parameter fits. The program includes the (extended) Czjzek distribution and order parameter model to indicate and quantify structural (dis)order in materials. With three examples we showed *EGdeconv*'s versatility to manage different experiment types and quadrupolar parameter distributions. In the future the program will be extended to include the fitting of single crystal data and 2D spectra.

4.7 Experimental

4.7.1 Experimental data

The ^{27}Al spectrum of Fig. 4.2 was measured on a 14.1 T Chemagnetics Infinity NMR spectrometer, using a 2.5 mm double resonance probe. The experiment consisted of a single $0.2\ \mu\text{s}$ hard pulse at 214 kHz rf field strength, while magic angle spinning the sample at a frequency of 15 kHz.

Experimental parameters for the spectra in Fig. 4.3 were a hard pulse excitation of $0.2\ \mu\text{s}$ and 160 kHz effective rf field strength at 15 kHz MAS at 9.1 T external field. The Hahn echo experiments on AlGaAs in Fig. 4.4 were performed at 18.8 T external field with an effective rf field of 625 kHz. The first delay was set to $175\ \mu\text{s}$ and acquisition started $5\ \mu\text{s}$ after the π pulse. For more information on the latter two experiments we refer to [50] and [38], respectively.

4.7.2 How to use EASY-GOING deconvolution

This section covers the practical aspects of *EGdeconv*. Introduction of input for *EGdeconv* adheres the convention that $\langle \dots \rangle$ input is required and $[\dots]$ is optional. The words, units and abbreviations replacing the \dots help to interpret the meaning of the variable as to what should be filled in. Please note that for the full description of all topics in this section we refer to the manual at <http://egdeconv.science.ru.nl>.

Installation requirements

The *EGdeconv* program requires a 64-bit Linux operating system. The installation package includes the *EGdeconv* and OpenMPI binaries. OpenMPI is responsible for the parallel computing. The program has been tested on various Linux distributions: Fedora 9, 10 and 11, Ubuntu 10.04 (LTS) and openSUSE 11.3. Installation will proceed via a shell script as depicted on our website.

Experimental data

EGdeconv requires the one-dimensional experimental spectrum in a two-column ASCII file with the number of complex spectrum points a power of two. The first column should be the spectral frequency and the second, the real or absolute value (squared) of the spectrum.

Libraries

Before attempting to fit the experimental data, the user should calculate a library of time or frequency domain data as a function of η and C_q for the appropriate experimental conditions. This can be done with any preferred simulation program, for example SIMPSON [32] and SPINEVOLUTION [23], as long as the libraries adhere to the format given in this section. The filename format should be

$$\langle \text{sitename} \rangle - \langle C_q(\text{MHz}) \rangle - \langle \eta \rangle . \langle \text{arb. file extension} \rangle$$

for example AIO4-30.25-0.01.fid. The currently supported internal file format is that of SIMPSON. The first five lines contain, in plain text, the keywords: SIMP, NP= $\langle \# \text{points} \rangle$, SW= $\langle \text{MHz} \rangle$, TYPE= $\langle \text{FID/SPE} \rangle$ and DATA. This information is used by *EGdeconv*. The rest of the file consists of the real and imaginary parts of the calculated data in the first and second column, respectively, finalised by the keyword END. *EGdeconv* allows to regulate the size of the actual (C_q, η) -grid used for the fitting procedure, via the keyword 'speciesX' as will be discussed below. Note that spectrum files should have the same number of points as the experiment, for the time domain data this is irrelevant. Examples of libraries are included in the installation package.

Input file

The *EGdeconv* installation package contains a number of example input files. Input files for the *EGdeconv* binary consist basically of plain text containing lines with either: comments (starting with #), keywords

$$\langle \text{keyword string} \rangle = \langle \text{value(s)} \rangle / \langle \text{string} \rangle$$

or parameter settings.

$$\text{parameter} = \langle n \rangle \langle \text{name} \rangle \langle \text{start} \rangle \text{ [[lower] [upper]] [[coupling] [nset/num]] }$$

There are numerous keywords, all tabulated in the manual, enabling the choice of: EA, extra output, special weighting or removal of parts of the spectrum, etc. a few examples are

```
#relative path
experimental spectrum = expdata/spec.dat
#absolute path to library
species1 = /home/user/depart_lib/A127
#single calc with start parameters
testcalculation = 1
```

Parameter lines contain, according to the format given above, parameter: reference number, (arbitrary) name, fixed value for single spectrum calculation or during fitting in absence of boundaries, upper and lower boundaries for fitting and type of inter/intra parameter set couplings. A few examples

```
#fix value during fit
parameter = 1 d 1
#fit between 3 and 5 MHz
parameter = 2 sigma 4 3 5
#value equal to par 3 set 1
parameter = 3 qcc0 30 E 1
```

It is important to place parameter lines in order of increasing reference number; the number indicates the parameter's identity for *EGdeconv*. The *EGdeconv* parser will consider the subsequent encounter of a lower reference number as the start of a new parameter set. Parameter sets correspond to individual sites and their (sub)spectrum.

One keyword named 'speciesX' requires special attention. This is the link between the inputfile and the calculated libraries. Creative usage of this keyword can save both computation time and memory. The keyword with all options present is given by

$$\text{species}\langle X \rangle = \langle \text{path} \rangle [[\eta_b] [\eta_e] [\eta_s] [C_{q,b}] [C_{q,e}] [C_{q,s}]]$$

For a different library the value of X, starting from one, should increase by one. The subscripts: *b*(egin), *e*(nd), and *s*(tep), indicate the precise grid in η and C_q (MHz) to use from the library located at $\langle \text{path} \rangle$. If no grid is specified, *EGdeconv* will load the entire library, unless the keyword is not linked to a parameter set.

In addition to the keyword 'speciesX' there is also an equally named parameter, currently reference number 199. The start value of this parameter relates directly to X and the corresponding library. This system allows multiple parameter sets to use the same library while it is present only once in the computer memory.

A second special parameter, currently number 198, regulates the quadrupolar parameter distribution model used to calculate the (sub)spectrum for the parameter set. The name of the parameter should be either: *no_distr*, *czj_distr* or *ext_czj_distr* which are self explanatory. The choice of distribution model assigns the meaning of parameter reference numbers one to four to respectively (η, C_q) , (d, σ) and $(d, \sigma, C_{q,o}, \eta_o)$. More information on the available parameters and their couplings is available in the *EGdeconv* manual. Working examples are also supplied with the installation package.

Program output

EGdeconv facilitates various outputs during, and at the end of the fitting procedure or calculation using only parameter start values for a test spectrum. During the fitting, a file is written and updated to summarise the current best fit parameters and the cost function value. At the end of the procedure a new file is created that contains the columns: frequency, best fit spectrum, experimental data and subspectra. Additionally a final file is made that summarises the results of the fit. We refer to the manual for a complete description of the (optional) output.

Acknowledgements

The authors thank Paulus J. Knijn, Ernst R.H. van Eck and Margriet W.H. Verkuijlen for providing experimental spectra for analysis using *EGdeconv*. We thank Gerrit C. Groenenboom for useful discussions on theoretical considerations and testing of the program. The Netherlands Organisation for Scientific Research (NWO) are acknowledged for their financial support of the solid-state NMR facility for advanced material science.

CHAPTER 5

EASY-GOING deconvolution: automated MQMAS NMR spectrum analysis based on a model with analytical crystallite excitation efficiencies

The *EASY-GOING deconvolution* (*EGdeconv*) program is extended to enable fast and automated fitting of multiple quantum magic angle spinning (MQMAS) spectra guided by evolutionary algorithms. We implemented an analytical crystallite excitation model for spectrum simulation. Currently these efficiencies are limited to two-pulse and z-filtered 3QMAS spectra of spin $3/2$ and $5/2$ nuclei, whereas for higher spin-quantum numbers ideal excitation is assumed. The analytical expressions are explained in full to avoid ambiguity and facilitate others to use them. The *EGdeconv* program can fit interaction parameter distributions. It currently includes a Gaussian distribution for the chemical shift and an (extended) Czjzek distribution for the quadrupolar interaction. We provide three case studies to illustrate *EGdeconv*'s capabilities for fitting MQMAS spectra. The *EGdeconv* program is available *as is* on our website <http://egdeconv.science.ru.nl> for 64-bit Linux operating systems.

J. Magn. Reson. 228 (2013) 116-124

5.1 Introduction

Multi-dimensional NMR of quadrupolar nuclei is a powerful spectroscopic tool to provide spectral insight into nucleus-environment interactions at the molecular level [39]. A good example and immediate focus of this paper is the routinely used MQMAS experiment for half-integer quadrupolar nuclei [36, 51]. This technique aids in distinguishing the contribution of the anisotropic part of the quadrupolar interaction from the isotropic chemical shift and quadrupolar induced shift in the F2 and F1 spectral dimensions. In practice this is especially useful for the analysis of one-dimensional spectra that have (strongly) overlapping lines.

Furthermore, NMR is a robust method for studying disordered materials, *e.g.*, glasses and semiconductors, since it probes the local atomic environment of NMR active nuclei. This disorder is reflected in the MQMAS line shapes, and can be translated into interaction parameter distributions. In the last ten years there has been an increasing interest to quantify this disorder [52, 43, 44]. A model developed by Czjzek *et al.* [42] and extended by Le Caër *et al.* [43, 44] is promising for describing the quadrupolar interaction parameter distribution resulting from this structural disorder. These models basically translate the distribution in electric field gradients, caused implicitly by variations in bond lengths and angles or disorder in the higher coordination spheres [38], to a distribution in interaction parameters.

In the NMR community the analysis of MQMAS spectra is currently facilitated by two programs; DMfit [39] for fitting with a simplified model, assuming ideal crystallite excitation, and SIMPSON [32] for accurate simulation incorporating all interactions. Regarding spectrum fitting, the computational cost for a single spectrum of the SIMPSON program is high. The main cause is the costly numerical integration of the Liouville-Von Neumann equation. The DMfit program is less broadly applicable, due to the assumption of ideal excitation of all crystallites, but allows spectrum fitting including a Czjzek distribution [52]. Another approach would be to use the GAMMA framework [53] that provides a versatile set of functionalities to simulate NMR experiments. It will require the user to program the NMR experiment and then connect it to a fitting routine. The presence of a Python interface (PyGAMMA) should make this procedure relatively easy.

This work aims to aid the quantitative analysis of MQMAS spectra [54] by the introduction of a fast fit-model that includes analytical crystallite excitation efficiencies. An approach that can be considered to partially fill the gap between SIMPSON and DMfit. The excitation efficiency model is available for 3QMAS spectra of spin $3/2$ (${}^7\text{Li}$, ${}^{23}\text{Na}$, ${}^{39,41}\text{K}$, ${}^{75}\text{As}$, ${}^{87}\text{Rb}$,...) and $5/2$ nuclei (${}^{17}\text{O}$, ${}^{25}\text{Mg}$, ${}^{27}\text{Al}$, ${}^{85}\text{Rb}$,...). For higher spin

quantum numbers an ideal excitation model is provided. Expressions were derived for a two-pulse and z-filtered MQMAS experiment in the infinitely fast MAS limit, thereby excluding simulation of spinning side bands. This approach enables a sub-second calculation of an MQMAS line shape, including a Gaussian chemical shift distribution, on a regular desktop computer, whereas a single-core SIMPSON simulation exceeds one hour. Accounting for a distribution in quadrupolar parameters and multiple chemical sites is consequently relatively inexpensive. Furthermore, we provide parallel computation support and robust convergence of the fit by offering a choice between three evolutionary algorithms [55, 41] to guide the fitting. A combination of MQMAS and one-dimensional NMR data can form a self-consistent data set for quantitative analysis, both supported by *EGdeconv* as is shown in the examples below.

The extension of *EGdeconv* [55] for MQMAS spectrum fitting has most functionalities of the one-dimensional fitting program, but excludes most importantly the library approach, thereby removing the second-party software dependence. In the remainder of this paper we will discuss the theory, the program structure and three case studies. Please note that this paper is not intended as a user manual for the program. A separate and up-to-date manual [56] is provided at our website <http://egdeconv.science.ru.nl>, where we also provide the input files for the examples.

5.2 Theory

The theory that follows is worked out specifically for spin $3/2$ and $5/2$ quadrupolar nuclei subjected to a two-pulse [36] or a z-filtered [51] 3QMAS scheme. Both experiments are illustrated in Fig. 5.1. The figures show how both experiments start with a radio frequency (rf) block-pulse to excite triple-quantum-coherence. Subsequently an incremented delay follows that forms the indirect dimension, after which a conversion pulse-scheme is used to obtain a detectable single quantum coherence to form the direct dimension. Finally the whole pulse scheme is phase cycled to exclusively obtain the required coherence pathway, all under MAS conditions.

Our aim is to present the analytical expressions in full for others to use without ambiguity. The manual [56] contains the expressions as they are actually implemented. We assume a static sample during the pulses and infinitely-fast MAS during the free evolution of the coherences. The implications of ignoring the time dependence of the crystallite orientations has been addressed in numerous papers [54, 57, 58, 59, 60, 61, 62]. It most of all concerns not simulating the redistribution of the spectral intensity in the spinning side bands in both dimensions. In our case studies we show how we can

still obtain accurate and reliable interaction parameters and relative site abundances for these type of spectra. In the discussion section we will elaborate more on the range of validity of the model.

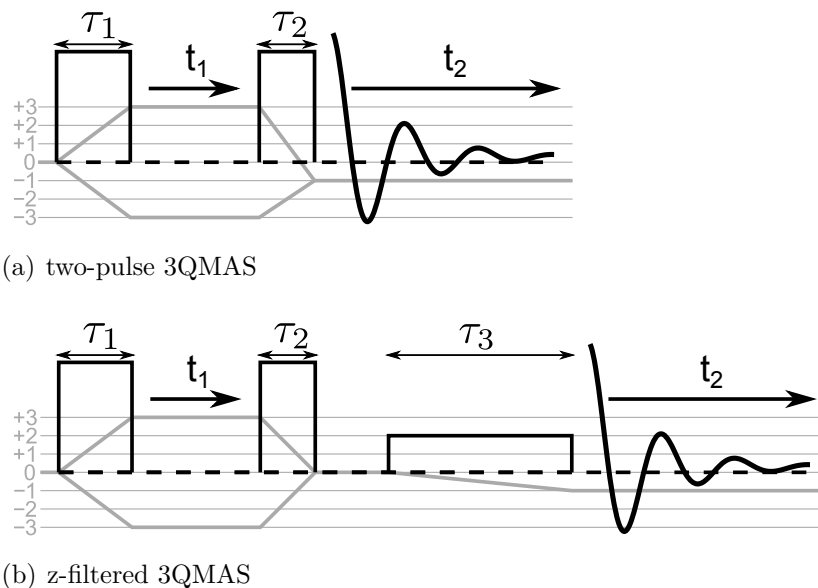


Figure 5.1: Triple quantum magic angle spinning pulse sequences. The pulse sequences with their indirect t_1 and direct t_2 dimension are shown in black. Coherence pathways are shown in grey. (a) The two pulses of length τ_1 and τ_2 provide the triple-quantum-coherence excitation and conversion, respectively. (b) In the z-filtered 3QMAS experiment, the triple-quantum-coherence is excited and subsequently converted to zero-quantum-coherence. A third low-amplitude rf-pulse of width τ_3 provides a selective excitation of the detectable single-quantum-coherence.

In our approach, the MQMAS spectrum is described directly in the frequency domain. The contribution of every crystallite orientation to the spectrum is constructed by determining its frequency coordinate and the efficiency of the excitation before adding it to the powder average. We will refer to the model without excitation efficiency as the ideal excitation model.

5.2.1 Crystallite spectral position

The spectrum of a crystallite in the infinitely-fast MAS case, is a single peak positioned at a two-dimensional frequency coordinate with components of the form [29]

$$\nu_{-m \rightarrow m} = 2m\nu_{iso} + C_0^{I,m}\nu_{qis} + C_4^{I,m}\nu_4(\alpha, \beta). \quad (5.1)$$

In the case of a 3QMAS experiment, the magnetic quantum numbers are $m = 1/2, 3/2$ for the direct and indirect dimension, respectively. I is the total nuclear angular momentum quantum number and the coefficients of the isotropic and anisotropic term of the quadrupolar interaction frequency are given by

$$C_0^{I,m} = 2m(I(I+1) - 3m^2) \quad (5.2)$$

$$C_4^{I,m} = 2m(18I(I+1) - 34m^2 - 5) \cdot P_4(\cos(\Theta_M)). \quad (5.3)$$

The fourth order Legendre polynomial term $P_4(\cos(\Theta_M))$, equal to $-7/18$ with Θ_M the magic angle, is a MAS averaged scaling factor. Furthermore ν_{iso} , ν_{qis} and $\nu_4(\alpha, \beta)$ in Eq. 5.1 are the isotropic chemical and quadrupolar induced shift and the anisotropic frequency contribution of the quadrupolar interaction. The latter two depend on the quadrupolar interaction parameters η (asymmetry) and C_q (quadrupolar coupling constant), two parameters we described in our previous *EGdeconv* paper [55], which are connected to Eq. 5.1 via

$$\nu_{qis} = -\frac{C_q^2(3 + \eta)}{40\nu_0 I^2(2I - 1)^2} \quad (5.4)$$

and

$$\begin{aligned} \nu_4(\alpha, \beta) = \frac{9C_q^2}{448\nu_0 I^2(2I - 1)^2} \cdot \left\{ \frac{7}{18} [3 - \eta \cos(2\alpha)]^2 \sin^4(\beta) \right. \\ \left. + 2 \left[\eta \cos(2\alpha) - 2 - \frac{\eta^2}{9} \right] \sin^2(\beta) + \frac{2}{45} \eta^2 + \frac{4}{5} \right\}. \end{aligned} \quad (5.5)$$

Here $\nu_0 = -\gamma B_0/2\pi$ is the Larmor frequency of the quadrupolar nucleus, and α and β the Euler angles that connect the principal axes frame of the quadrupolar interaction to the MAS rotor frame, see 5.7.4.

5.2.2 Crystallite excitation efficiency

We now proceed with the derivation of the crystallite excitation efficiencies. The approach consists of solving the time dependent Liouville-Von Neumann equation for the

density operator involving both the multiple-quantum-coherence excitation pulse and the coherence-conversion pulse scheme. In addition to the assumptions of infinitely-fast MAS during free coherence-evolution and a static sample during pulsing, we neglect any rf-field offset [59, 60]. An assumption that relies on the relatively strong quadrupolar interaction compared to practical rf-offsets, as will be addressed in the discussion section.

The relevant part of the density operator at thermal equilibrium in the rotating frame of the Zeeman interaction at time τ_0 , is given by $\hat{\rho}(\tau_0) = \hat{I}_z$ and transforms after a block-pulse of length τ_1 , see Fig. 5.1, according to

$$\hat{\rho}(\tau_1) = \exp \left\{ -i\hat{H}\tau_1 \right\} \hat{\rho}(\tau_0) \exp \left\{ i\hat{H}\tau_1 \right\} . \quad (5.6)$$

\hat{H} is the Hamiltonian operator, in units of angular frequency, during an rf block-pulse. The Hamiltonian includes the rf-field and the first order quadrupolar interaction

$$\hat{H} = -\omega_1 \hat{I}_x + \frac{\Omega_Q(\theta, \varphi)}{6} [3\hat{I}_z^2 - \hat{I}^2], \quad (5.7)$$

with $2\omega_1 = -\gamma B_{rf}$ and the quadrupolar frequency

$$\Omega_Q(\theta, \varphi) = \frac{\omega_Q}{2} \left[3 \cos^2(\theta) - 1 + \eta \sin^2(\theta) \cos(2\varphi) \right] . \quad (5.8)$$

Here $\omega_Q = 6\pi C_q/[2I(2I - 1)]$ and φ and θ are the Euler angles that connect the principal axes frame of the quadrupolar interaction to the laboratory frame, see 5.7.4.

We now express the density operator in a basis of eigen functions $|I, m\rangle$ of the Zeeman Hamiltonian, and calculate matrix element indices according to

$$\rho_{I+m'+1, I+m+1} \equiv \langle I, m' | \hat{\rho} | I, m \rangle . \quad (5.9)$$

To obtain the triple-quantum-coherence excited by the first pulse, we need to determine the triple-quantum-coherence matrix element at time τ_1 . This requires the analytical diagonalisation of the Hamiltonian matrix given by Eq. 5.7 expressed in the appropriate Zeeman basis. Eq. 5.6 in the basis of eigen functions of the Hamiltonian directly returns the density matrix at time τ_1 . After transformation back to the $|I, m\rangle$ basis we obtain the triple-quantum-coherence term after the excitation pulse. Using Mathematica [63] we obtained for a spin $3/2$ nucleus

$$\begin{aligned}
 \rho_{41}(\tau_1) &= -\rho_{14}(\tau_1) = \\
 &\frac{3i \cos(\omega_1 \tau_1)}{\omega_+^2 - \omega_-^2} \left[\left\{ \Omega_Q \omega_- + \omega_1 \omega_+ \right\} \sin(\omega_+ \tau_1) \right. \\
 &\quad \left. - \left\{ \Omega_Q \omega_+ + \omega_1 \omega_- \right\} \sin(\omega_- \tau_1) \right] \\
 &+ \frac{3i \sin(\omega_1 \tau_1)}{2(\omega_+^2 - \omega_-^2)} \left[\left\{ \omega_-^2 - \omega_+^2 - \Omega_Q^2 \right\} \cos(\omega_+ \tau_1) \right. \\
 &\quad \left. + \left\{ \omega_-^2 - \omega_+^2 + \Omega_Q^2 \right\} \cos(\omega_- \tau_1) \right]
 \end{aligned} \tag{5.10}$$

that clearly shows the involved sum and difference frequencies

$$2\omega_{\pm} = \sqrt{\Omega_Q^2 - 2\Omega_Q\omega_1 + 4\omega_1^2} \pm \sqrt{\Omega_Q^2 + 2\Omega_Q\omega_1 + 4\omega_1^2}. \tag{5.11}$$

as well as the conventional pulse flip-angle $\omega_1 \tau_1$.

We also obtained expressions for spin $I = 5/2$ where the Mathematica-based Hamiltonian diagonalisation of Man [64] was used. The symmetrical triple-quantum-coherence elements are

$$\rho_{52}(\tau_1) = -\rho_{25}(\tau_1) = \frac{i}{2} \sum_{m=1}^3 \sum_{n=1}^3 \frac{k_{mn}}{Q_{m+} Q_{n-}} \sin\left((\omega_{m+} - \omega_{n-}) \tau_1\right). \tag{5.12}$$

The definitions of the variables are

$$Q_{m\pm} = \left[1 + \frac{5\omega_1^2}{4\left(\frac{10}{3}\Omega_Q - \omega_{m\pm}\right)^2} + \frac{2\omega_1^2}{\left(\frac{8}{3}\Omega_Q \pm \frac{3}{2}\omega_1 + \omega_{m\pm}\right)^2} \right] \tag{5.13}$$

and

$$\begin{aligned}
 k_{mn} &= \left[3 + \frac{25\omega_1}{4\left(\frac{10}{3}\Omega_Q - \omega_{m+}\right)\left(\frac{10}{3}\Omega_Q - \omega_{n-}\right)} \right. \\
 &\quad \left. + \frac{2\omega_1}{\left(\frac{8}{3}\Omega_Q \pm \frac{3}{2}\omega_1 + \omega_{m+}\right)\left(\frac{8}{3}\Omega_Q \pm \frac{3}{2}\omega_1 + \omega_{n-}\right)} \right].
 \end{aligned} \tag{5.14}$$

The eigenvalues of the Hamiltonian matrix are

$$\begin{aligned}\omega_{1\pm} &= \mp \frac{\omega_1}{2} + 2\sqrt{\frac{s_{\pm}}{3}} \cos\left(\frac{\phi_{\pm}}{3}\right) \\ \omega_{2\pm} &= \mp \frac{\omega_1}{2} - 2\sqrt{\frac{s_{\pm}}{3}} \cos\left(\frac{\pi}{3} - \frac{\phi_{\pm}}{3}\right) \\ \omega_{3\pm} &= \mp \frac{\omega_1}{2} - 2\sqrt{\frac{s_{\pm}}{3}} \cos\left(\frac{\pi}{3} + \frac{\phi_{\pm}}{3}\right),\end{aligned}\tag{5.15}$$

with

$$\cos(\phi_{\pm}) = \frac{\Omega_Q}{18s_{\pm}} \sqrt{\frac{3}{s_{\pm}}} (160\Omega_Q^2 \mp 36\Omega_Q\omega_1 - 144\omega_1^2)\tag{5.16}$$

and

$$s_{\pm} = \frac{84}{9}\Omega_Q^2 \pm 4\Omega_Q\omega_1 + 4\omega_1^2.\tag{5.17}$$

In the case of two-pulse 3QMAS data we are interested in the single-quantum-coherence created by the second pulse shown in Fig. 5.1(a). By applying the approach for the first pulse to $\hat{\rho}(\tau_1)$ we obtained for spin $I = 3/2$

$$\begin{aligned}\rho_{23}(\tau_1 + \tau_2) &= \frac{3\omega_1^2}{2(\omega_+^2 - \omega_-^2)} \left[\rho_{14}(\tau_1) - \rho_{41}(\tau_1) \right] \\ &\times \cos(\omega_1\tau_2) \sin\left(\frac{1}{2}(\omega_+ + \omega_-)\tau_2\right) \sin\left(\frac{1}{2}(\omega_+ - \omega_-)\tau_2\right).\end{aligned}\tag{5.18}$$

The same procedure was applied for spin $I = 5/2$ resulting in the following expression

$$\begin{aligned}\rho_{34}(\tau_1 + \tau_2) &= \omega_1^2 \left[\rho_{25}(\tau_1) - \rho_{52}(\tau_1) \right] \\ &\times \sum_{m=1}^3 \sum_{n=1}^3 \frac{\cos\left((\omega_{m+} - \omega_{n-})\tau_2\right) (Q_{m+}Q_{n-})^{-1}}{\left(\frac{8}{3}\Omega_Q + \frac{3}{2}\omega_1 + \omega_{m+}\right) \left(\frac{8}{3}\Omega_Q - \frac{3}{2}\omega_1 + \omega_{n-}\right)}.\end{aligned}\tag{5.19}$$

In the case of z-filtered 3QMAS experiments, see Fig. 5.1(b), we consider the efficiency directly proportional to the population difference of the central-transition states. For a spin $I = 3/2$ this is

$$\rho_{22}(\tau_1 + \tau_2) - \rho_{33}(\tau_1 + \tau_2) = -2i \tan(\omega_1\tau_2) \rho_{23}(\tau_1 + \tau_2).\tag{5.20}$$

This assumes ideal conversion of the zero-quantum coherence to single-quantum coherence during the selective third pulse of length τ_3 in the experiment, feasible by choosing the appropriate rf-field [65, 66]. For spin $I = 5/2$ the expression for $\rho_{33}(\tau_1 + \tau_2) - \rho_{44}(\tau_1 + \tau_2)$ is equal to the right hand side of Eq. 5.19 multiplied by $-2i$ and the cosine function replaced with a sine [56].

5.2.3 Ideal crystallite excitation

In this work we define ideal crystallite excitation as that the spectral line shape is determined directly by the number of crystallite orientations that are mapped to each two-dimensional frequency coordinate with components given by Eq. 5.1. In other words, the excitation efficiency has a negligible angular dependence. In general this situation is created by using short pulses, so no differentiation in coherence-evolution of the crystallites during the pulse takes place. Additionally there should be sufficient field strength to fully cover the spectral width of the line shape, and a negligible rf-offset dependence.

5.3 The program

As noted above, the model for MQMAS spectrum simulation is build into the *EGdeconv* program [55], a framework that provides parallelised evolutionary algorithms to guide the data fitting. Therefore we will only describe the MQMAS simulation model here, and refer to the previous paper [55] and the accompanying manual [56] for further information on the parameters and keywords used in the input file of the *EGdeconv* program.

We now proceed with the description of the synthesis of a subspectrum. A subspectrum corresponds to a chemical site and the sum of subspectra is the simulated spectrum that is used to fit the experimental data. Fig. 5.2 shows the different steps of the calculation. All variables presented in the figure are directly controlled via a parameter set in the *EGdeconv* input file. The heart of the simulation in Fig. 5.2 is the crystallite spectrum. It is created by combining the frequency coordinate components given by Eq. 5.1 and the corresponding, but optional, excitation efficiency Eq.'s 5.18, 5.19 or 5.20. The program allows to apply a shearing transformation [29] as a function of λ according to

$$\nu_{-m \rightarrow m}^{sheared} = \nu_{-m \rightarrow m} - \lambda \nu_{-1/2 \rightarrow 1/2}. \quad (5.21)$$

A crystallite spectrum is generated per C_q, η pair and subsequently summed over all orientations in a powder average. Currently only the ZCW (Zaremba, Conroy, Wolfsberg) averaging scheme [67] is implemented. Two-angle sets are used, with an equidistant integration over the third angle described in appendix 5.7.4 and [56]. The quadrupolar interaction parameters may be distributed, currently supported by the (extended) Czjzek distribution, which involves a weighted sum over the generated powder spectra.

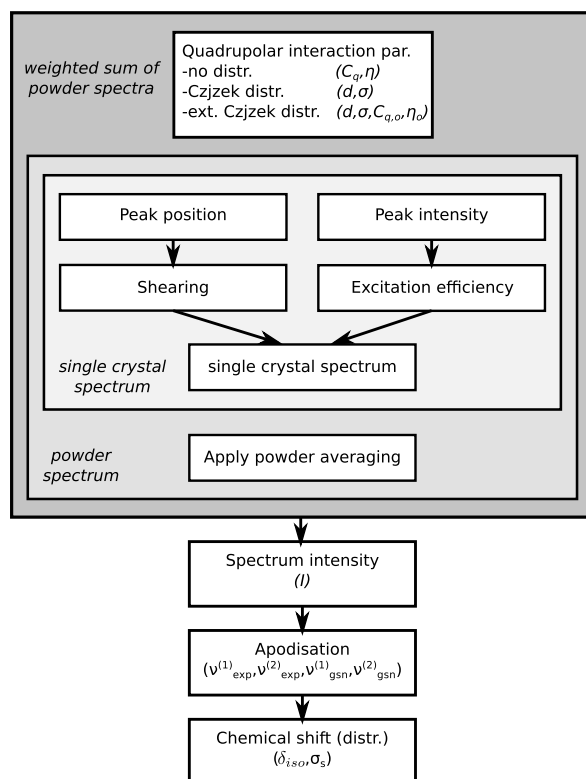


Figure 5.2: The scheme used by *EGdeconv* to compute a subspectrum corresponding to a chemical site. If the quadrupolar interaction parameters have a distribution, crystallite spectra are summed per C_q, η pair to form a powder spectrum and subsequently summed according to a distribution over C_q, η pairs. Furthermore, the subspectrum receives a relative intensity, line broadening and a convolution with a Gaussian distribution for the chemical shift. Parameters that are indicated in the figure are available in each parameter set in the input file.

After all summations are done, the subspectrum is multiplied with an overall intensity factor that corresponds to the relative abundance of a chemical site in the material. Additionally the two-dimensional line shape can be broadened with a Gaussian and/or exponential apodisation to, *e.g.*, match the data processing or include the dephasing effects of dipolar couplings. The final step is the convolution of the spectrum with an optional (Gaussian) chemical shift distribution. This distribution has a mean δ_{iso} and a width σ_s [56].

5.4 Examples

In this section we present the results of several case studies each of which represents a different part of the program’s capabilities. We start by benchmarking *EGdeconv* by fitting several ^{27}Al 3QMAS spectra, nuclear spin $5/2$, of aluminium alkoxides. Quadrupolar interaction parameters of the alkoxides were determined by fitting one-dimensional data [68]. Their 3QMAS data was used to determine the isotropic chemical shifts. In this case study we show how we obtain all these parameter values directly from the 3QMAS spectra and how spinning side bands are handled.

Subsequently we present the fit of ^{87}Rb 3QMAS data, nuclear spin $3/2$, of rubidium-nitrate measured under experimental conditions that lead to non-ideal excitation, thereby putting our fitting model with analytical excitation efficiencies to the test. In addition to reproducing the interaction parameters of [69], we prove that we can reproduce the line shape and relative site intensities where the ideal excitation model does not.

To conclude we show the analysis of the 3QMAS spectrum of an yttrium-sialon glass. This spectrum reflects a distribution in both quadrupolar interaction parameters and chemical shift, that we try to model with respectively a Czjzek and Gaussian distribution and the analytical excitation efficiencies. We show how we can fit the line shapes of three sites simultaneously to obtain their interaction distribution parameters. The interaction parameters can subsequently be used to deconvolute the one-dimensional spectrum, and obtain the relative site abundances.

All fits include the excitation efficiencies, unless stated otherwise, and were performed with the Covariance matrix adaptation evolution strategies (CMA-ES) algorithm [16]. The *EGdeconv* input files of all MQMAS examples are available on our website <http://egdeconv.science.ru.nl>.

5.4.1 Aluminium Alkoxides

In Fig. 5.3 the ^{27}Al sheared 3QMAS data fits of three different alkoxides coordinated to aluminium are presented. All spectra were measured and analysed in ref. [68] on the basis of one-dimensional and 3QMAS data. Table 5.1 summarises our resulting parameter values from the 3QMAS fit, alongside their values from the previous study [68]. In all spectra the sum-projections in both direct and indirect dimensions of the two-dimensional experimental and simulated data are shown. A least-squares fit [56] between these projections was used as a measure of fit-quality for the CMA-ES algorithm. The obvious benefit of the sum-projections is that the intensity of the spinning side

bands is added to that of the central transition in the δ_2 dimension, which can be more readily simulated. The δ_1 dimension sum-projection provides in these spectra an extra feature to determine the isotropic position of the central transition during the fitting.

	δ_{iso} [ppm]		C_q [MHz]		η	
ethoxide	35.5	<i>35.5</i>	9.58	<i>9.65</i>	0.37	<i>0.39</i>
butoxide	48.5	<i>48.5</i>	13.03	<i>13.14</i>	0.64	<i>0.61</i>
isoprop. (IV)	60.0	<i>61.5</i>	12.20	<i>12.37</i>	0.14	<i>0.14</i>
(VI)	0.8	<i>2.5</i>	0.6	<i>1.9</i>	0.0	<i>0.0</i>

Table 5.1: Fitted interaction parameters for the alkoxide spectra in Fig. 5.3, values from [68] are in italics. In the fit of isopropoxide, η of the octahedral site was fixed at 0.

The spectrum of aluminium ethoxide, Fig. 5.3(a), that corresponds to a five-coordinated aluminium, shows a good match between the sum-projections in the (δ_2) dimension. The main difference at high δ_2 values in the figure is caused by an Al_2O_3 impurity. For the case of aluminium butoxide, Fig. 5.3(b), with a tetrahedral aluminium surroundings the fitted spectrum also closely resembles the sum-projection of the experimental data. The line shape at $\delta_1 \approx 250$ ppm is an aliased spinning side band. Table 5.1 shows that we obtained interaction parameters that agree with the findings of [68] on the basis of MQMAS and one-dimensional data for both spectra.

The spectrum of aluminium isopropoxide in Fig. 5.3(c) reveals tetrahedral (IV) and octahedral (VI) sites that posed the opportunity to determine relative site abundances. From the fit of these relative intensities we obtained the ratio (IV):(VI)=1:2.7 which was determined 1:3 by [68] on the basis of one-dimensional data. It should be noted that there is a negligible difference between the fitted relative intensities, whether the analytical excitation efficiencies are accounted for or not. This means that with the current pulse widths both sites are excited with similar efficiency. The difference for C_q of the octahedral site (VI) is due to a lack of quadrupolar features in the sharp line.

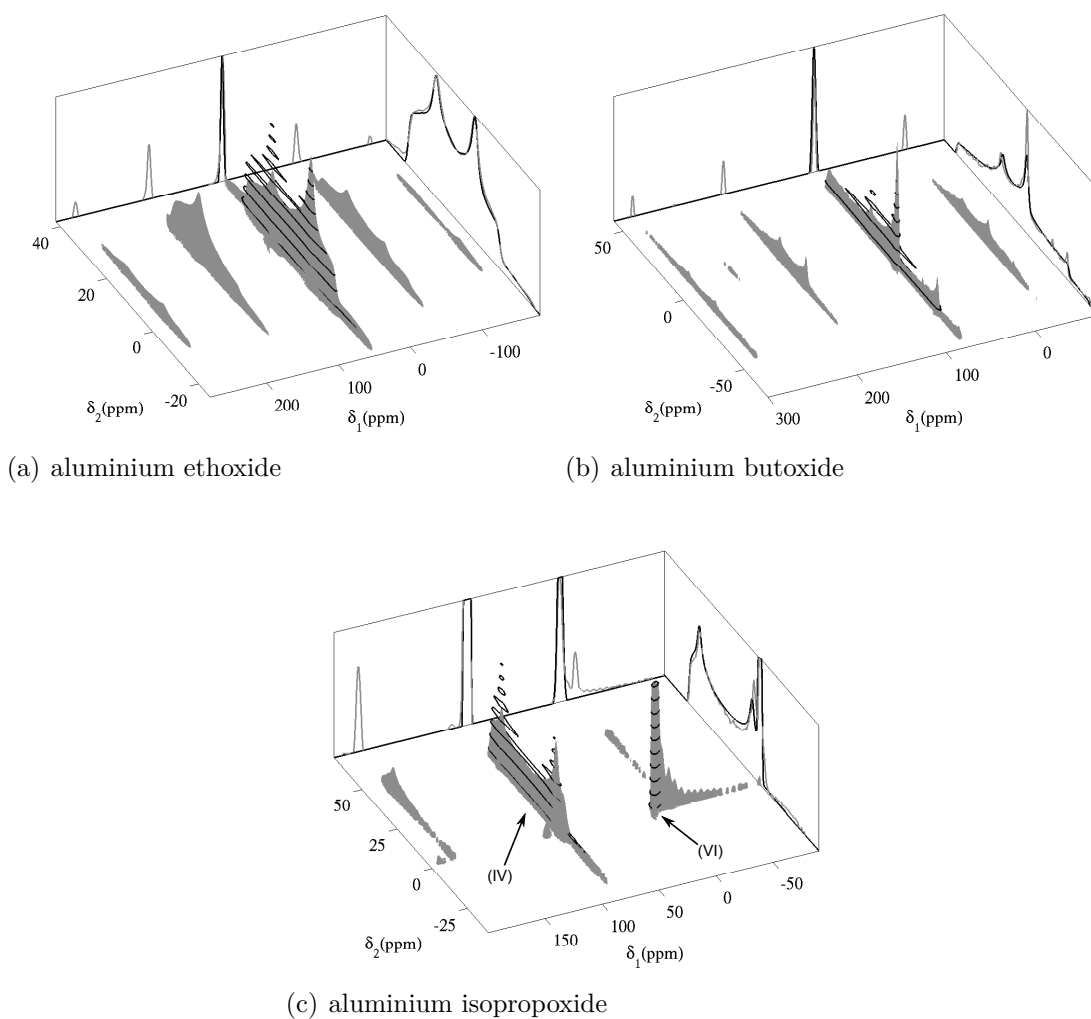


Figure 5.3: ^{27}Al z-filtered 3QMAS spectra ($\omega_1/2\pi=310$ kHz, $\tau_1=1.3$ μs , $\tau_2=0.45$ μs , and $\tau_3=4$ μs with $\omega_1/2\pi=21$ kHz), experiment (grey) and fit (black), for three aluminium alkoxides [68]. The spectra are normalised based on their integrals, and their sum-projections are scaled with their integrals to be visible on the intensity scale of the spectrum. In the isopropoxide spectrum we zoomed in on the tetrahedral (IV) site, this is the reason for the cut of the octahedral (VI) site peak. Data was sheared after the fit.

5.4.2 Rubidium-nitrate

Rubidium-nitrate (RbNO_3), as the guinea pig for MQMAS experiments, has three well-defined sites with: equal abundance, similar quadrupolar coupling constants, but different asymmetry parameters as given in the most to the right column in table 5.2.

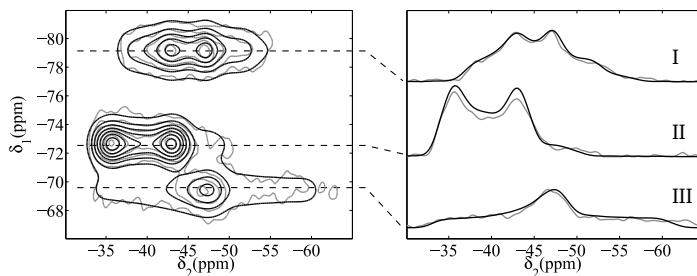
To further test the analytical excitation efficiency model and distinguish it from the ideal excitation model, two ^{87}Rb 3QMAS spectra of RbNO_3 were measured. One spectrum was obtained using relatively short pulses and strong rf-field strength and represents the ideal excitation case (Fig. 5.4(a)), as discussed in section 5.2.3. The second spectrum was obtained with complementary settings to evoke non-ideal excitation (Fig. 5.4(b) and 5.4(c)). By measuring the spectrum at a magnetic field of 300 MHz proton frequency we also encountered overlapping lines as an additional challenge for the fitting.

A fit of the ideal excitation spectrum using either model results in Fig. 5.4(a). The least squares difference between the two-dimensional experimental and simulated spectra was used [56] as the quality measure for the CMA-ES algorithm. Table 5.2 shows that the fitted parameter values are nearly equal to those from literature [70]. This is confirmation that the assumption of ideal excitation is valid in this case.

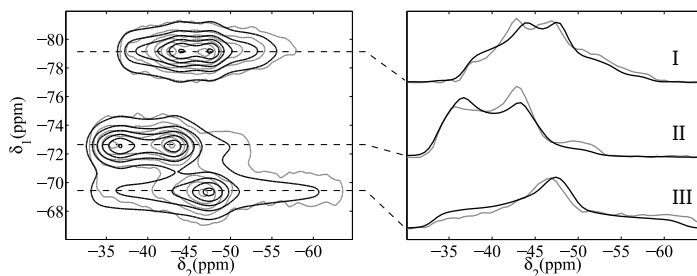
Fitting the second spectrum resulted in a different fit for each model as shown in Figs 5.4(b) and 5.4(c). Incorporation of the (analytical) excitation efficiencies provides a better description of especially line shapes I and II. This is reflected in a difference in η parameter for both fits as shown in table 5.2. Particularly line shape II is different from that in Fig. 5.4(a). The intensity of the left peak appears to move into the right shoulder of the line.

site	pars	(Fig. 5.4(a)) ideal	(Fig. 5.4(b)) eff. off	(Fig. 5.4(c)) eff. on	[70]
I	C_q [MHz]	1.75	1.77	1.74	1.77
	η	0.54	0.60	0.55	0.54
II	C_q [MHz]	1.72	1.75	1.73	1.72
	η	0.19	0.27	0.16	0.19
	I	0.97	0.90	1.06	1.00
	integral	1.14	0.93	0.93	–
III	C_q [MHz]	1.99	1.99	1.99	2.01
	η	0.89	0.93	0.91	0.90
	I	1.00	0.85	0.99	1.00
	integral	0.93	0.87	0.87	–

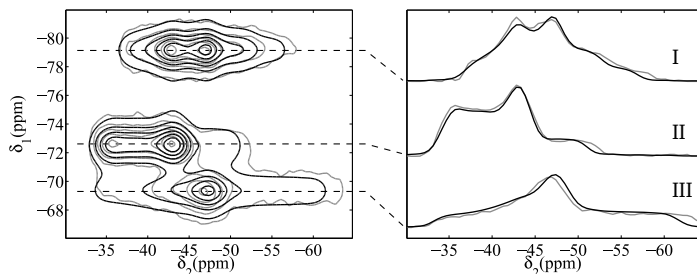
Table 5.2: Fitted parameter values of the ^{87}Rb 3QMAS spectra of rubidium-nitrate in Fig. 5.4. I , as indicated in Fig. 5.2, stands for relative intensity, in this case with respect to site I. For comparison the parameter values obtained by [70] at 29.3°C are given in the most to the right column.



(a) excitation efficiency model fit to ideal excitation data



(b) ideal excitation model fit to non-ideal excitation data



(c) excitation efficiency model fit to non-ideal excitation data

Figure 5.4: Simulations (black) of the z-filtered ^{87}Rb 3QMAS spectrum of rubidium-nitrate (grey). Integrals of the spectra are set equal, contour lines are drawn at the same intensities. (a) ideal excitation spectrum ($\omega_1/2\pi=211$ kHz, $\tau_1=2.6$ μs , $\tau_2=0.9$ μs) fitted with excitation efficiency model. (b) and (c) the non-ideal excitation spectrum ($\omega_1/2\pi=108$ kHz, $\tau_1=5.2$ μs , $\tau_2=2.6$ μs) fitted with and without analytical excitation efficiencies.

With respect to the prediction of relative site abundances, it follows from table 5.2 that the excitation model fit comes closest to the actual ratio. Especially if we compare the sum of the intensities (due to the overlap of the line shapes), we obtain the ratios 1:2.05 and 1:1.75. The ideal excitation model appears to follow the trend of the line shape integrals, which leads to an underestimation of the intensities of lines II and III.

5.4.3 Yttrium-sialon glass

Sialon glasses doped with rare-earth metals are interesting for photo-electric applications. Glasses are disordered systems which makes quantification in terms of interaction constants tedious. The benefit of having MQMAS data is that it aids in effectively separating chemical shift and quadrupolar interaction contributions to the spectrum, that would otherwise not be visible in the one-dimensional data.

In practice this means that, after shearing, a distribution in chemical shift will become visible as a broadened line in the F1 dimension. For a distribution in quadrupolar interaction parameters, the line shape is influenced in both dimensions by the (isotropic) quadrupolar induced shift. However, only the F2 dimension is influenced by the anisotropic part of the interaction. The two-dimensional spectrum thereby provides enough features to distinguish and fit interaction parameter distributions, and potentially relative site abundances as discussed in the rubidium-nitrate case study.

Fig. 5.5(a) shows the fitted ^{27}Al 3QMAS spectrum of an yttrium-sialon glass [71] (named after the atomic constituents: silicium, aluminium, oxygen and nitrogen), using the inner product cost function [56] between the two-dimensional spectra as the quality measure. In both dimensions of the spectrum we see broadened lines which indicates that both chemical shift and quadrupolar interactions are distributed. In the two-dimensional plane, the lines are separated which is useful to avoid ambiguity in the fit. Note that the one-pulse spectrum of the sialon material in Fig. 5.5(b) does not provide these insights.

The three distinct lines of the chemical sites in the spectrum are probably broadened due to structural variations in bond angles and lengths deviating from: tetrahedral, trigonal bipyramidal and octahedral coordinations in the material [72]. Fig. 5.5(a) shows how a combination of the Czjzek distribution for the quadrupolar interaction

coordination	δ_{iso} [ppm]	σ_s [ppm]	σ [MHz]	2D integral	2D I	1D I
tetrahedral	62.6	17.0	4.03	1.00	1.00	1.00
trigon. bip.	27.7	13.6	4.04	0.21	0.20	0.30
octahedral	-2.4	11.4	3.65	0.03	0.04	0.05

Table 5.3: The parameter values from the fit of the yttrium-sialon glass (Fig. 5.5). Parameters δ_{iso} , σ_s are the mean and width of the Gaussian chemical shift distribution, σ the width of the Czjzek distribution (power factor $d=5$), 2D integrals of the lines in Fig. 5.5(a), I the relative intensities of Figs 5.5(a) and 5.5(b).

parameters and a Gaussian distribution for the chemical shift can approximate the line shapes in the spectrum. Only at the basis of the largest peak a mismatch is visible between the more triangular basis of the experimental data and the more rounded simulated spectrum. Table 5.3 presents the fitted parameter values. It should be noted that a fit with either ideal or excitation efficiency model did not change the results. Together with the fact that the intensities match with the line integrals, we may conclude ideal excitation of the material.

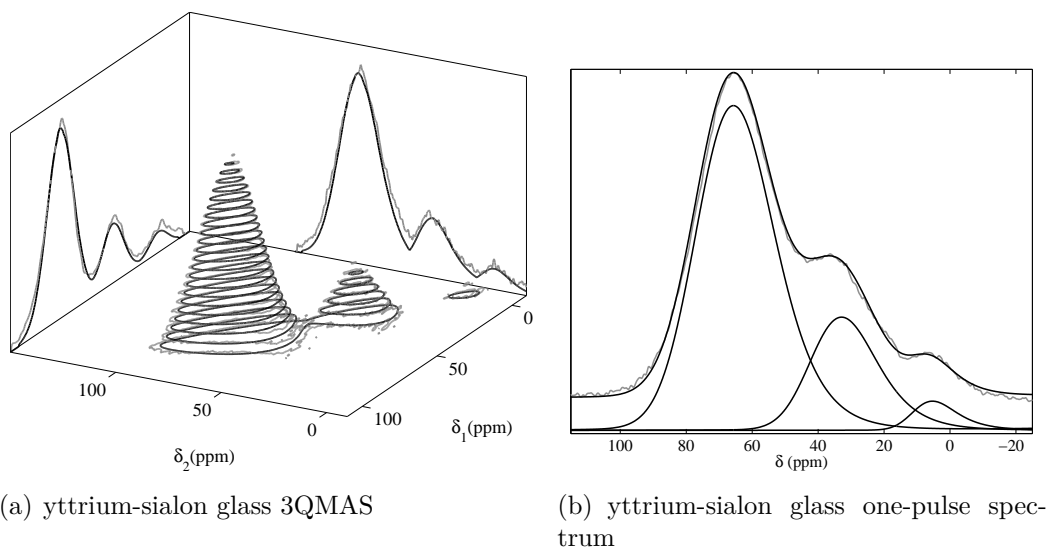


Figure 5.5: Experimental data is shown in grey, simulated results are in black. (a) Fitted ^{27}Al 3QMAS spectrum of an yttrium-sialon glass with skyline projections. Three chemically distinct sites are shown that correspond to variations in, from bottom to top: tetrahedral, trigonal bipyramidal and octahedral surroundings. A Czjzek and Gaussian distribution is used for the quadrupolar interaction and chemical shift, respectively. Fitted parameter values are given in table 5.3. (b) Fit of the one-pulse spectrum. Czjzek distribution parameter values from the 3QMAS fit are used (table 5.3). The subspectra that constitute the simulated spectrum are plotted below the base line.

The fitted interaction parameters of the 3QMAS were used to fit the one-pulse spectrum of the yttrium-sialon glass. This led to a good and stable fit as shown in Fig. 5.5(b). Note that the asymmetric line shape of the subspectra is caused by the Czjzek distribution. Table 5.3 shows the fitted relative intensities of the lines. There is a significant difference for the MQMAS and 1D fit with respect to the tetrahedral and trigonal bipyramidal site intensity ratios. This difference we explain by the different

effective $T_1 > 2s$ of the two sites in combination with the cycle delay of 4 seconds that was used to limit the time needed for the 3QMAS experiment. The one-pulse data should be quantitative since only a short pulse, and therefore a small flip-angle, is used.

5.5 Discussion

A large part of this paper is focussed on the analytical excitation efficiencies to extend the accuracy of fast MQMAS spectrum simulation. Here we would like to elaborate on the limits of the validity of the theory by using physical arguments and tests we performed.

One of the first assumptions is that the spin system can be treated as static during the pulsing. An important argument in favour of this, is the order of magnitude difference between the pulse widths of several μs (equivalent to hundreds of kHz) and the MAS speeds of several tens of kHz. In addition to the argument of a small γ angle rotation (5.7.4) of the MAS rotor, typically of the order of 10 degrees, the positions of the crystallites along the direction of rotation are interchanged. This leads to a further indistinction for the crystallite excitation efficiency. If the pulse becomes too long or the MAS speed too high, the excitation efficiency will be influenced, and our model will no longer be valid. Pulse lengths can be shortened by increasing the rf-field strength [29]. Whether or not the use of our model is valid should be assessed per experiment. For the case study of the sialon glass, at 37 kHz MAS, the line shapes could be reproduced accurately.

For testing purposes we used SIMPSON as well as our own numerical integration routine to solve the Liouville-Von Neumann equation including the full quadrupolar interaction Hamiltonian, rf-field and sample rotation for a single crystallite. Although we did not thoroughly study all of the parameter dependencies, for typical pulse widths and interaction parameters, related to the examples, our perturbative method did not significantly deviate from the exact solution. SIMPSON additionally accounts for MAS and second order quadrupolar coupling. The results started to deviate for MAS speeds above 30 kHz and pulse widths larger than 10 μs . This shows our model is realistic for a wide range of experimental settings.

Secondly we assume an ideal zero to single quantum conversion pulse in a z-filtered 3QMAS experiment. Which should be acceptable with a properly chosen rf-field for the z-filter pulse [65, 66]. We experimentally verified the correctness of the assumption by comparing two-pulse data with z-filtered data at different rf-field strengths for the

rubidium-nitrate. Additionally our testing program showed that the explicit incorporation of the third pulse does not alter the results for typical experimental settings.

Thirdly we disregard rf-offset, which is acceptable considering that the tilt angle of the nutation does not deviate much for line widths of several kHz and rf-field strengths of hundred kHz or more. If necessary, it is possible to implement analytical excitation efficiencies including rf-offset [59, 60].

The assumption that proves the most difficult to handle is the infinitely-fast spinning limit. Spinning side bands are often visible in the spectrum, so this immediately proves this assumption is incorrect. In order to still obtain reliable results it is important to have all spinning side bands present in the spectrum, so all spectral intensity can be regained in the sum-projections. These projections can then used for the fitness function as was discussed in the alkoxides example. A practical solution may be to perform rotor synchronised detection experiments [73], in order for all side bands to fold back on top of the central peak.

To conclude, in addition to obtaining the correct line shape and thereby the quadrupolar interaction parameters, it is also feasible to obtain the relative abundance of the sites directly from the MQMAS data, as was shown in the rubidium-nitrate example. In the yttrium-sialon case study, however, we encountered a problem due to the requirement of a relatively long cycle delay in the experiment due to the different effective T_1 's of the sites. In such cases it is easier to obtain the interaction parameter information from the MQMAS data and use these to fit a one-pulse spectrum to obtain quantitative relative intensities.

5.6 Conclusions

We have shown the capabilities of the *EGdeconv* program to fit, guided by evolutionary algorithms, MQMAS spectra using an analytical crystallite excitation efficiency model. We presented the theory for the model in full detail to avoid ambiguity and to facilitate others to use it. In three case studies we showed how to obtain quantitative information from fitting 3QMAS spectra with: spinning side bands, multiple sites, interaction parameter distributions and non-ideal excitation. The ideal excitation model encompasses all quadrupolar nuclei and multiple-quantum-coherence excitation, while excitation efficiencies are available for $I = 3/2, 5/2$ nuclei and two-pulse and z-filtered 3QMAS.

5.7 Experimental

5.7.1 1D sialon fit

For the fit of the 1D spectrum of the yttrium-sialon glass with the *EGdeconv* program, a library size of 609 files, simulated with SIMPSON, was used with C_q ranging from 1 to 15 MHz in steps of 0.5 MHz and η from 0 to 1 in steps of 0.05.

5.7.2 Yttrium-sialon

The single-pulse and MQMAS experiments were performed on an 850 MHz Varian spectrometer at a MAS frequency of 37 kHz, with $\text{AlCl}_3(\text{aqua})$ as reference compound for ^{27}Al at 221 MHz.

A pulse length of 1.4 μs and a rf-field strength of 20 kHz was used in the single-pulse experiment. The z-filtered 3QMAS experiment was performed with an rf-field strength of 150 kHz for the excitation and conversion pulses with a pulse length of 2.4 and 0.8 μs respectively. The z-filter pulse was 5 μs long at an rf-field of 20 kHz.

Both single-pulse and MQMAS spectrum were corrected for aluminium background of the rotor. The rotor signal was measured with the same experimental settings and subsequently subtracted from the spectra.

5.7.3 Rubidium-nitrate

The ^{87}Rb z-filtered 3QMAS spectrum was measured on a 300 MHz Varian spectrometer at 12.5 kHz MAS. The non-ideal excitation data was obtained using an rf-field strength of 105 kHz for the excitation and conversion pulses with lengths 5.2 and 1.8 μs , respectively. For the ideal excitation data the rf-field settings were: 211 kHz field strength and pulse widths of 2.6 and 0.9 μs . The z-filter pulse had a strength of 10 kHz and width of 11 μs . A reference of $\text{RbCl}(\text{aqua})$ was used for ^{87}Rb at 96 MHz.

5.7.4 Frame interconversion

Eq.'s 5.1 and 5.7 for the position and intensity of a single crystal spectrum are defined with respect to the MAS and laboratory reference frame, respectively. Figure 5.6 illustrates how the Euler angles relate the principal axes frame (x,y,z) of the quadrupolar interaction tensor to a reference frame, either the MAS frame (Z along the MAS axis) with α , β , γ or laboratory frame (Z along the magnetic field) where we use φ , θ , ψ in this work.

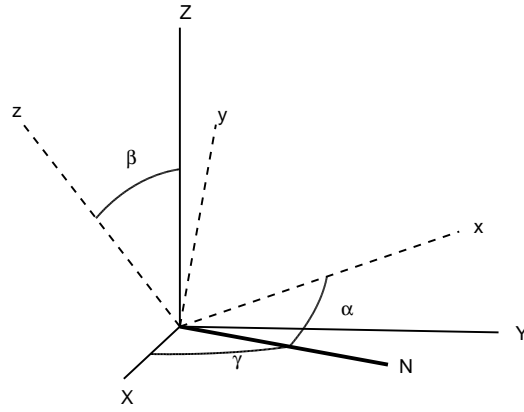


Figure 5.6: Definition of the Euler angles (α , β , γ) that relate the interaction's principal axes frame (x, y, z) to the reference frame (X, Y, Z). Note that the vector N is normal to the plane of the z and Z axes.

It is the infinitely-fast MAS assumption and cylindrical symmetry of the magnetic field that render Eq. 5.1 and 5.7 invariant to the γ and ψ angle. However, if we want to relate a frequency coordinate to an excitation efficiency, the angles need to be related to each other. We worked out the following relations

$$\begin{aligned}\cos(\theta) &= -\sin(\Theta_M) \sin(\beta) \cos(\gamma) + \cos(\Theta_M) \cos(\beta) \\ \cos(\varphi) &= \sin(\Theta_M) [\cos(\alpha) \cos(\beta) \cos(\gamma) - \sin(\alpha) \sin(\gamma)] \\ &\quad + \cos(\Theta_M) \cos(\alpha) \sin(\beta),\end{aligned}\tag{5.22}$$

from which we can construct all terms in Eq. 5.8 using goniometric identities.

Acknowledgements

D.G. thanks Wim J. van der Zande for suggestions during the preparation of this paper's manuscript. The authors thank Dr. Bert H.T.J.M. Hintzen (TU/e) for providing the yttrium-sialon material.

Pressure broadening in the impact approximation

In the second part of this thesis we move to molecular spectroscopy. Where the interaction between nuclear spin and electromagnetic radiation is the key in NMR experiments, the field of molecular spectroscopy uses the interaction of radiation with other molecular degrees of freedom: rotation, vibration, and electronic structure. The focus of the current and the following chapter is the theoretical description of the influence of collisions on the absorption of radiation by molecular oxygen. What is so special about the approach discussed here, is that the theory is parameter free. Experimentally observable quantities are predicted by a theoretical model that is based on fundamental constants and the laws of physics.

6.1 Absorption of radiation by a molecular gas

The transmitted intensity of electromagnetic radiation that travelled a path length l through a cell filled with gas is described by the Lambert-Beer law. For radiation of angular frequency ω and intensity $I_0(\omega)$, the relation is given by

$$I_{\text{tr}}(\omega) = I_0(\omega) \exp\{-ln\sigma(\omega)\}. \quad (6.1)$$

Here is n the number of particles per volume (number density), and $\sigma(\omega)$ the absorption cross section (in unit length squared). This cross section is determined by the

properties of the gas and may originate from several mechanisms. The latter will be discussed in the next chapter for the case of molecular oxygen. For an infinitesimally small path length l and a molecule with a magnetic transition dipole moment, the absorbed radiation intensity becomes directly proportional to the integrated line cross section [74, 75]

$$I_{f \leftarrow i} = \int_{-\infty}^{\infty} \sigma(\omega) d\omega = \frac{2\pi\omega_{i,f}}{(4\pi\epsilon_0)3\hbar c^4} |\langle f | \hat{\boldsymbol{\mu}} | i \rangle|^2, \quad (6.2)$$

in unit length per molecule. The constants ϵ_0 , c , and \hbar are respectively: the vacuum permittivity, the speed of light, and Planck's reduced constant. The matrix element $\langle f | \hat{\boldsymbol{\mu}} | i \rangle$ is that of the magnetic transition dipole moment operator, which is responsible for absorption of radiation of frequency $\omega_{i,f}$, and the transition from initial state $|i\rangle$ to final state $|f\rangle$ of the molecule.

6.2 Change in absorption by elastic particle collisions

This section discusses the change in radiation absorption by elastic collisions of a molecule with a magnetic transition dipole moment. Hence, the state of the light-absorbing molecule can only change its relative phase by the collisions. To specialise this discussion even further towards the case of molecular oxygen in the next chapter, an electronic magnetic dipole transition is considered. The particles that collide with the absorber are structureless, *i.e.*, they have no internal degrees of freedom that can change due to collisions or absorption of light.

To reduce the complexity of the theory and to show the fundamental aspects of the pressure broadening theory, additional restrictions are used. Part of these restrictions will be lifted in section 6.4. The restrictions are:

1. The motion of the absorber is not taken into account, *e.g.*, no Doppler effect.
2. Perturbing particles do not interact with each other.
3. Interaction potentials between absorber and perturber are scalar additive.
4. The Born-Oppenheimer approximation [76] is used for the particle-absorber interaction potentials, which leads to a separate potential for each electronic state of the absorber.

With these restriction, the wavefunction describing the absorber-perturber system can be written as a product

$$|x\rangle = \psi_x^{(a)}(\mathbf{r}) \prod_{m=1}^N \psi_{x,\mathbf{k}_m}^+(\mathbf{r}_m). \quad (6.3)$$

Here $x = i, f$ represent the initial and final electronic transition state of the molecule. The absorber states $\psi_x^{(a)}(\mathbf{r})$ are eigenfunctions of the Schrödinger equation containing the molecular Hamilton operator $\hat{H}^{(a)}$ according to

$$\hat{H}^{(a)}\psi_x^{(a)}(\mathbf{r}) = E_x^{(a)}\psi_x^{(a)}(\mathbf{r}), \quad (6.4)$$

with $x = i, f$, and $E_x^{(a)}$ the state energies. The coordinate \mathbf{r} represents all internal coordinates of the molecule. The motion of the perturbers in the potential of the absorber is treated quantum mechanically. Their translational states are the scattering wavefunctions $\psi_{x,\mathbf{k}_m}^+(\mathbf{r}_m)$, which are solutions of Schrödinger equations of the form

$$[\hat{T}_m + \hat{V}_x]\psi_{x,\mathbf{k}_m}^+(\mathbf{r}_m) = \varepsilon_{x,\mathbf{k}_m}\psi_{x,\mathbf{k}_m}^+(\mathbf{r}_m), \quad (6.5)$$

with \hat{T}_m the kinetic energy operator for the m -th perturber, \hat{V}_x ($x = i, f$) the interaction potential with either the initial or final (electronic) state of the absorbing molecule. The vector \mathbf{r}_m connects the centres of mass of the two particles. The solutions of Eq. 6.5 are the scattering wave functions $\psi_{x,\mathbf{k}_m}^+(\mathbf{r}_m)$, normalised to the volume of the gas cell V , with asymptotic wave vector \mathbf{k}_m and energy $\varepsilon_{x,\mathbf{k}_m}$.

To determine the change in light absorption of the molecule due to collisions, the whole system of the absorbing molecule and the structureless perturbers should be considered in the $|i\rangle$ and $|f\rangle$ states of Eq. 6.2. Substitution of the product state of Eq. 6.3 into Eq. 6.2 leads to the expression for radiation absorption of the system

$$I_{f \leftarrow i}(\mathbf{k}'_1, \dots, \mathbf{k}'_N, \mathbf{k}_1, \dots, \mathbf{k}_N) = \frac{2\pi\omega_{if}|\langle\psi_f^{(a)}|\hat{\boldsymbol{\mu}}|\psi_i^{(a)}\rangle|^2}{(4\pi\varepsilon_0)3\hbar c^4} \prod_{m=1}^N |\langle\psi_{f,\mathbf{k}'_m}^+|\psi_{i,\mathbf{k}_m}^+\rangle|^2, \quad (6.6)$$

at frequency

$$\omega_{if} = \hbar^{-1}[E_f^{(a)} - E_i^{(a)} + \varepsilon_{f,\mathbf{k}'_1} - \varepsilon_{i,\mathbf{k}_1} + \dots + \varepsilon_{f,\mathbf{k}'_N} - \varepsilon_{i,\mathbf{k}_N}]. \quad (6.7)$$

These expressions show that the absorption intensity at spectral frequency ω_{if} depends on a complex interference in the inproducts of the elastic scattering wavefunctions. In the potentials of the initial and final electronic states the perturbing particles may gain and lose translational energy, and the absorption frequency changes relative to the pure molecular transition frequency.

6.3 Absorption line shape in the impact approximation

In the previous section the absorption intensity for a molecular system with a completely determined quantum state was given. The next step is to obtain the spectral

line shape $F(\omega)$ that can be determined experimentally. This line shape follows from Eq. 6.6 by averaging over initial wave vectors \mathbf{k}_m with weight $p_{\mathbf{k}_m}$ (the Boltzmann factor), and integrating over final wave vectors \mathbf{k}'_m

$$F(\omega) = \int d\mathbf{k}_1 \dots \int d\mathbf{k}_N \int d\mathbf{k}'_1 \dots \int d\mathbf{k}'_N \times p_{\mathbf{k}_1} \dots p_{\mathbf{k}_N} I_{f \leftarrow i}(\mathbf{k}_1, \dots, \mathbf{k}_N, \mathbf{k}'_1, \dots, \mathbf{k}'_N) \delta(\omega - \omega_{if}), \quad (6.8)$$

$$= \frac{2\pi\omega |\langle \psi_f^{(a)} | \hat{\boldsymbol{\mu}} | \psi_i^{(a)} \rangle|^2}{(4\pi\epsilon_0) 3\hbar c^4} \frac{1}{2\pi} \int dt e^{i\omega t} e^{-i/\hbar(E_f^{(a)} - E_i^{(a)})t} [\phi(t)]^N. \quad (6.9)$$

Here $\delta(\omega - \omega_{if})$ is a Dirac delta function. Moving from Eq. 6.8 to Eq. 6.9 the line shape is written as the Fourier transform of a time dependent function $\phi(t)$ raised to the power of the number of perturbers N . This result is still exact under the restrictions posed in the previous section, and if the interaction potentials for all N perturbers are the same. Hence, the effect of one perturber on the absorber is used to extrapolate to the case of N perturbers. In other words, in this theory the line shape follows from the consideration of one binary collision. We define

$$\phi(t) \equiv \int d\mathbf{k} \int d\mathbf{k}' p_{\mathbf{k}} |\langle \psi_{f,\mathbf{k}'}^+ | \psi_{i,\mathbf{k}}^+ \rangle|^2 e^{-i/\hbar(\epsilon_{f,\mathbf{k}'} - \epsilon_{i,\mathbf{k}})t}, \quad (6.10)$$

$$= \int d\mathbf{k} p_{\mathbf{k}} \langle \psi_{i,\mathbf{k}}^+ | e^{i[\hat{T} + \hat{V}_f]t} e^{-i[\hat{T} + \hat{V}_i]t} | \psi_{i,\mathbf{k}}^+ \rangle. \quad (6.11)$$

The Fourier transform of function $\phi(t)$ essentially provides the line shape that results from one binary collision. Since the perturber is most of the time far away from the absorber, this line shape is expected to closely resemble a delta function. Hence $\phi(t)$ is approximately constant, with a correction that is proportional to the probability of the collision taking place. In a gas cell of volume V , very large compared to the particle size, a probability on the order of V^{-1} is expected. At this point the stage is set for an elegant limit towards a large number of perturbers [77]

$$\lim_{N \rightarrow \infty} [\phi(t)]^N = \lim_{N \rightarrow \infty} [1 - V^{-1}g(t)]^N = \exp[-ng(t)]. \quad (6.12)$$

Here $n = N/V$ is the number density, number of perturbers per volume. The exact form of $g(t)$ is given without further derivation [77]

$$g(t) = \int d\mathbf{k} p_{\mathbf{k}} \left\{ i \langle \psi_{f,\mathbf{k}}^+ | \hat{V}_i - \hat{V}_f | \psi_{i,\mathbf{k}}^+ \rangle t + \int \frac{d\mathbf{k}'}{8\pi^3} |\langle \psi_{f,\mathbf{k}'}^+ | \hat{V}_i - \hat{V}_f | \psi_{i,\mathbf{k}}^+ \rangle|^2 \frac{1 - \exp[-i(\epsilon - \epsilon')t]}{(\epsilon - \epsilon')(\epsilon - \epsilon' - i\eta)} \right\}. \quad (6.13)$$

Here i is the imaginary number, ε , and ε' are the corresponding energies of states $|\psi_{i,\mathbf{k}}^+\rangle$ and $|\psi_{f,\mathbf{k}'}^+\rangle$. Each of the two terms in $g(t)$ represents a different part of the collision dynamics. The first term only describes completed collisions. This is visible due to the fact that the \mathbf{k} vectors for both scattering states are the same. Hence there is no uncertainty in the energy balance before and after collision, this is related to long time dynamics via the uncertainty principle. The second term in $g(t)$ contains an oscillatory integral over \mathbf{k}' vectors. In contrast to the first term, this term represents the more short time dynamics. It poses a formidable challenge to compute, and to our knowledge this type of calculations have only been performed by atomic physicists [78, 79, 80, 81].

The *impact approximation* states that it takes many weak collisions to obtain an appreciable change to the absorber's wavefunction, or that strong collisions are well separated in time [82]. This behaviour is captured by the first term in $g(t)$ in Eq. 6.13. The matrix element in this term can be worked out exactly in terms of scattering amplitudes that are obtained from solving the Lippmann-Schwinger equation [83]. These elements represent what part of the free particle state $|\mathbf{k}\rangle$ is scattered by the potential. The function $g(t)$ without the second term becomes [77]

$$g(t) \approx \int d\mathbf{k} p_{\mathbf{k}} \left\{ i[\langle \mathbf{k} | \hat{V}_i | \psi_{i,\mathbf{k}}^+ \rangle - \langle \psi_{f,\mathbf{k}}^+ | \hat{V}_f | \mathbf{k} \rangle + 2\pi i \int d\mathbf{k}' \langle \psi_{f,\mathbf{k}}^+ | \hat{V}_f | \mathbf{k}' \rangle \delta(\varepsilon_{f,\mathbf{k}'} - \varepsilon_{i,\mathbf{k}'}) \langle \mathbf{k}' | \hat{V}_i | \psi_{i,\mathbf{k}}^+ \rangle] t \right\}, \quad (6.14)$$

$$\equiv i\langle v\sigma \rangle t \quad (6.15)$$

The Dirac delta function $\delta(\varepsilon_{f,\mathbf{k}'} - \varepsilon_{i,\mathbf{k}'})$ ensures the total energy before and after collision remains the same, also called on-the-energy-shell scattering. The off-the-energy-shell matrix elements are required for the second term in Eq. 6.13. Additionally, a notation is defined for the average over \mathbf{k} vectors. The symbol $\langle v\sigma \rangle$ stands for the thermal average over collision energies of the collisional cross section σ . In the next chapter it is given explicitly.

Substitution of Eq. 6.15 in Eq. 6.12 leads via the Fourier transform in Eq. 6.9 to the collisional line shape

$$F(\omega) = \frac{2\pi\omega}{(4\pi\varepsilon_0)3\hbar c^4} \frac{1}{\pi} \text{Im} \left[\frac{|\langle \psi_f^{(a)} | \hat{\boldsymbol{\mu}} | \psi_i^{(a)} \rangle|^2}{\omega - \omega_{if} - in\langle v\sigma \rangle} \right], \quad (6.16)$$

$$= \frac{2\pi\omega}{(4\pi\varepsilon_0)3\hbar c^4} \frac{1}{\pi} \frac{|\langle \psi_f^{(a)} | \hat{\boldsymbol{\mu}} | \psi_i^{(a)} \rangle|^2 [n\langle v\sigma \rangle_{\text{Re}}]}{[\omega - \omega_{if} + n\langle v\sigma \rangle_{\text{Im}}]^2 + [n\langle v\sigma \rangle_{\text{Re}}]^2}. \quad (6.17)$$

It is a Lorentzian line shape with the width and shift determined by the real and imaginary part of the rate $\langle v\sigma \rangle$ defined in Eq. 6.15. Given that the long time behaviour

of function $g(t)$ in Eq. 6.13 is correctly described in the impact approximation, this line shape is valid close to the line centre. In what frequency range it is valid exactly, is different per molecular system [84, 85, 86].

6.4 Multiple transitions and inelastic collisions

The treatment of a single absorption line may be extended to incorporate multiple lines and inelastic collisions [82]. This is still possible within the impact approximation. One important difference with respect to the treatment discussed in the previous sections, is that the wavefunction that describes the whole system may not immediately be written as the product of Eq. 6.3. This product was partly the result of only allowing elastic collisions and perturber-absorber potentials that are scalar additive. Based on this wavefunction the collisional line broadening could be described directly in terms of binary collisions in section 6.3.

With the inclusion of inelastic collisions and possibly perturber-absorber potentials that do not add in a scalar fashion, the product wavefunction of Eq. 6.3 is only true if the collisions are disentangled [82]. Fortunately, this is exactly what happens naturally in the impact approximation that states that there should be a long time between strong collisions. The line shape is thus still described in terms of binary collisions [82].

A more convenient mathematical representation for the pressure broadening theory is obtained with standard angular momentum theory [87]. The equations may be reduced by imposing that the absorbing molecule is surrounded by an isotropic gas [88]. What remains is an expression in terms of standard scattering matrix elements similar to Eq. 6.13 that can be found by solving the coupled-channels equations [89, 90]. The resulting expression for a multi-line spectrum with rotational transitions between states with quantum numbers j_α and j_β is given by [91]

$$F(\omega) = \frac{2\pi\omega}{(4\pi\epsilon_0)3\hbar c^4} \frac{1}{\pi} \text{Im} \left[\sum_{j'_\alpha, j'_\beta; j_\alpha, j_\beta} \langle j'_\alpha || \mu || j'_\beta \rangle^* \langle j_\alpha || \mu || j_\beta \rangle \rho_{j_\alpha} [\mathbf{A}^{-1}]_{j'_\alpha, j'_\beta; j_\alpha, j_\beta} \right], \quad (6.18)$$

$$A_{j'_\alpha, j'_\beta; j_\alpha, j_\beta} = (\omega - \omega_{j_\alpha, j_\beta}) \delta_{j_\alpha, j'_\alpha} \delta_{j_\beta, j'_\beta} - in \langle v \sigma_{j'_\alpha, j'_\beta; j_\alpha, j_\beta} \rangle. \quad (6.19)$$

Here ρ_{j_α} is the population of state j_α , and $\delta_{j_\alpha, j'_\alpha}$ is a Kronecker delta. The element $\langle j_\alpha || \mu || j_\beta \rangle$ is a Wigner-Eckart reduced matrix element according to the convention [92]

$$\langle j_\alpha m_\alpha | \hat{\mu}_m | j_\beta m_\beta \rangle = (-1)^{j_\alpha - m_\alpha} \begin{pmatrix} j_\alpha & 1 & j_\beta \\ -m_\alpha & m & m_\beta \end{pmatrix} \sqrt{2j_\alpha + 1} \langle j_\alpha || \mu || j_\beta \rangle, \quad (6.20)$$

with the large parentheses indicating a Wigner 3j symbol.

The main differences between Eqs. 6.17 and 6.19 are the presence of primed quantum numbers and that $\langle v\sigma \rangle$ becomes a matrix, named the relaxation matrix [93]. The primes indicate that the initial and final states of different transitions may be coupled by inelastic collisions. Spectral lines can exchange intensity, which is called line-mixing [94, 95], and the spectrum will then deviate from a sum of Lorentzian line shapes. With this introduction the reader should be prepared enough to read the final paper of this thesis.

CHAPTER 7

A theoretical and experimental study of pressure broadening of the oxygen A-band by helium

The rotationally resolved spectrum of the oxygen A-band $b^1\Sigma_g^+(v=0) \leftarrow X^3\Sigma_g^-(v=0)$ perturbed by collisions with helium was studied theoretically using the impact approximation. To calculate the relaxation matrix, scattering calculations were performed on a newly computed helium-oxygen ($b^1\Sigma_g^+$) interaction potential as well as on a helium-oxygen ($X^3\Sigma_g^-$) interaction potential from the literature. The calculated integrated line cross sections and broadening coefficients are in good agreement with experimental results from the literature. Additionally, cavity ring-down experiments were performed in the wings of the spectral lines for a quantitative study of line-mixing, *i.e.*, the redistribution of rotational line intensities by helium-oxygen collisions. It is shown that inclusion of line-mixing in the theory is required to reproduce the experimentally determined absolute absorption strengths as a function of the helium density.

(in preparation)

7.1 Introduction

The near-infrared (≈ 760 nm) A-band extinction of molecular oxygen is of increasing atmospheric importance. It is used extensively for the calibration of satellite instru-

ments that help to determine atmospheric temperature and pressure [96, 97]. The extinction of light by atmospheric oxygen in the A-band region is understood to come from: Rayleigh scattering, collision induced and magnetic dipole absorption [98]. Much effort has been invested to quantify the contribution of these mechanisms experimentally [99, 100, 101]. This includes mixtures of oxygen with other collision partners, such as nitrogen and noble gases.

Rayleigh scattering is the elastic scattering of light on subwavelength particles. Collision induced absorption (CIA) involves absorption of light by a transient electric dipole moment, induced by a collision with a perturber [102, 103, 104]. These mechanisms add broad features to the extinction in the A-band region as will be shown below. The strongest and sharpest features in the A-band are the *P* and *R* branch of the forbidden magnetic dipole transitions (electronic spin angular momentum change $\Delta S = 1$ and molecular symmetry change $\Sigma^- \leftrightarrow \Sigma^+$). The electric dipole transitions are doubly forbidden as well ($\Delta S = 1$ and $g \leftrightarrow g$), but it is spin-orbit coupling that makes only the magnetic dipole absorption allowed [105]. Regarding electric quadrupole transitions, that spectrum would have an *O* and *S* branch with the same order of magnitude as the *P* and *R* branch [105]. Only the *P* and *R* branch are observed.

To our knowledge, there is no first principles prediction of an electronic magnetic dipole absorption spectrum of molecular oxygen influenced by collisions with a foreign gas present in the literature. In a broader perspective, there is no fully quantum mechanical treatment available in the literature that treats an electronic transition of a molecule perturbed by collisions. The reason may very well be the requirement for an accurate interaction potential of the perturbing particle with the electronically excited state of the absorbing molecule.

These considerations motivated our choice to start with a relatively simple system of molecular oxygen perturbed by helium atoms. This first of all reduces the quite extensive scattering calculations required to obtain the spectral line shapes in the impact approximation. Secondly, we have access to a cavity ring-down setup to measure the absolute absorption intensities for this system as a function of pressure. The cavity ring-down technique is capable of measuring minute absorptions due to the long path length created for the radiation by the highly reflective mirrors that are used. We used this characteristic to quantitatively study the shape of the lines relatively far from the line centre. These regions provide information about the deviation of the spectrum from a sum of Lorentzian line shapes commonly named line-mixing [94, 95]. The impact approximation theory should describe line-mixing correctly if the participating spectral lines are not spaced too far apart.

In the following sections of this paper, we start with a review of the theory of

the rotationally resolved spectroscopy of the oxygen A-band. The expression for the absorption spectrum in the impact approximation will be given. Followed by the description of the calculation of the interaction potential for the helium atom with the oxygen b state, and the performed scattering calculations. Then the cavity ring-down experiments will be described, including the processing of the data to remove the contribution of Rayleigh scattering and CIA. Finally, the results are presented and discussed. Firstly, the quantities that are relatively insensitive to the effects of line-mixing are given and compared to their experimental values taken from the literature. These are the integrated line cross sections and pressure broadening coefficients. Line-mixing is neglected in the calculation of these quantities. Subsequently, the line-mixing mechanism is put to the test by studying pressure-dependent absolute absorption strengths in the valleys between spectral lines. Calculated results that either include or neglect line-mixing are compared to the cavity ring-down data. These results show the importance of including line-mixing to describe the absorption spectrum correctly.

7.2 Theory

7.2.1 Rotational structure of the $X^3\Sigma_g^-$ and $b^1\Sigma_g^+$ states of O_2

The electronic ground state of molecular oxygen is an open shell state with term symbol $X^3\Sigma_g^-$. In this work the rotronic structure of this state is required, and the vibrational part of the wavefunction is considered later. The relatively weak coupling between nuclear rotation and electronic spin (Tab. 7.1), warrants the expansion of the ground state fine structure states $|F_i JM_J; ^3\Sigma_g^- \rangle$ (laboratory frame) in a Hund's case b basis

$$\begin{aligned}
 |F_i JM_J; ^3\Sigma_g^- \rangle = & \sum_{N=J-1}^{J+1} a_N^{F_i} \sum_{M_N, M_S} \sqrt{\frac{2N+1}{4\pi}} D_{M_N, \Lambda=0}^{N, *}(\alpha, \beta, 0) \\
 & \times |^3\Sigma_g^-, S=1, M_S \rangle \langle NM_N SM_S | JM_J \rangle.
 \end{aligned} \tag{7.1}$$

The two-angle normalised Wigner D-functions $\sqrt{(2N+1)/4\pi} D_{M_N, \Lambda=0}^{N, *}(\alpha, \beta, 0)$, nuclear rotation eigenfunctions, are coupled to the electronic spin by the Clebsch-Gordan coefficient $\langle NM_N SM_S | JM_J \rangle$, and mixed by the expansion coefficients $a_N^{F_i}$. Here α and β are azimuthal and altitudinal angles, respectively. Quantum number $\Lambda = 0$ is the projection of the orbital angular momentum of the $|^3\Sigma_g^-, S=1, M_S \rangle$ electronic state on the molecular axis.

The fine structure label F_i has three possible values: F_1 , F_2 , or F_3 . According to

the convention used in [106] the expansion coefficients $a_N^{F_i}$ in Eq. 7.1 are of the form

$$a_{N=J-1}^{F_1} = a_{N=J+1}^{F_3} = \cos \phi, \quad (7.2)$$

$$a_{N=J}^{F_2} = 1, \quad (7.3)$$

$$a_{N=J+1}^{F_1} = -a_{N=J-1}^{F_3} = \sin \phi, \quad (7.4)$$

and they follow from diagonalisation of the molecular Hamiltonian [107]. Eq. 7.2 shows that the F_1 and F_3 functions are respectively constructed only from $N = J - 1$ and $N = J + 1$ rotation states. The mixing-angle ϕ will decrease if states of higher N are involved.

Note that N has only odd values. This results from the Pauli principle that states that the total wave function given in Eq. 7.1 should not change sign under the permutation operator $\hat{P}_{1,2}$ of the spin zero (bosonic) nuclei. Thus the product of the nuclear and electronic state parity should be positive. The parity of the nuclear wavefunctions is $(-1)^N$. With respect to the electronic wavefunction, is permutation of the nuclei equal to reflection of the electron coordinates in the body-fixed frame. This results in an odd parity (Σ^-) for the oxygen ground state electronic wavefunction.

For the b state we write

$$|NM_N; {}^1\Sigma_g^+\rangle = \sqrt{\frac{2N+1}{4\pi}} D_{M_N, \Lambda=0}^{N,*}(\alpha, \beta, 0) |{}^1\Sigma_g^+\rangle. \quad (7.5)$$

Here N has only even values, since the parity of the electronic wave function with respect to $\hat{P}_{1,2}$ has a different sign (Σ^+).

7.2.2 Magnetic transition dipole matrix elements

The rovibronic transitions between the states $|F_i; JM_J; {}^3\Sigma_g^-\rangle$ and $|NM_N; {}^1\Sigma_g^+\rangle$ (both vibrational ground states) have magnetic dipole character despite the selection rules $- \leftrightarrow +$ and $\Delta S = 0$ [105]. The mechanism responsible for the non-zero transition probability is spin-orbit coupling [108]. Both electric dipole and quadrupole transitions are not present in the spectrum as discussed in the introduction.

To further explain the magnetic dipole transition mechanism we first rewrite the oxygen ground state from Eq. 7.1 in a Hund's case a basis

$$\begin{aligned} |F_i; JM_J; {}^3\Sigma_g^-\rangle &= \sum_{N=J-1}^{J+1} a_N^{F_i} \sum_{\Sigma, \Omega} \sqrt{\frac{2N+1}{4\pi}} D_{M_J, \Omega}^{J,*}(\alpha, \beta, 0) \\ &\quad \times |{}^3\Sigma_{g, \Omega}^-, S=1, \Sigma\rangle \langle N \Lambda = 0 S \Sigma | J \Omega \rangle, \end{aligned} \quad (7.6)$$

for which we used

$$|{}^3\Sigma_g^-, SM_S\rangle = \sum_{\Sigma} |{}^3\Sigma_g^-, S\Sigma\rangle \langle {}^3\Sigma_g^-, S\Sigma | {}^3\Sigma_g^-, SM_S\rangle, \quad (7.7)$$

$$= \sum_{\Sigma} |{}^3\Sigma_g^-, S\Sigma\rangle D_{M_S, \Sigma}^{S, *}(\alpha, \beta, 0), \quad (7.8)$$

and the standard rule for a product of two Wigner D-functions [87]. Here Σ is the body-fixed spin projection on the molecular axis, and $\Omega = \Lambda + \Sigma$ ($\Lambda = 0$ in this case). The electronic orbital angular momentum part of the ${}^3\Sigma_g^-$ wavefunction remains unchanged, since the function is by definition body-fixed.

The electronic magnetic dipole operator is given by

$$\hat{\mu} = \sum_i \frac{\mu_B}{\hbar} (\hat{l}_i + g_e \hat{s}_i), \quad (7.9)$$

with \hat{l}_i and \hat{s}_i the orbital and spin angular momentum of electron i , μ_B the Bohr magneton, $g_e \approx 2.0$ the electron g-factor, and \hbar Planck's reduced constant. Absorption intensities are directly proportional to the square of the space-fixed (SF) transition dipole moments, which in turn are related to the body-fixed (BF) dipole operator via the transformation

$$\hat{\mu}_m^{SF} = \sum_k \hat{\mu}_k^{BF} D_{m, k}^{1, *}(\alpha, \beta, 0). \quad (7.10)$$

The combination of Eq. 7.5, 7.6 and 7.10, leads to an expression for the transition dipole matrix elements

$$\begin{aligned} \langle F_i J M_J; {}^3\Sigma_g^- | \hat{\mu}_m^{SF} | N M_N; {}^1\Sigma_g^+ \rangle &= \sum_{M_J} (-1)^{J-M_J} \sqrt{2J+1} \\ &\times \begin{pmatrix} J & 1 & N \\ -M_J & m & M_N \end{pmatrix} \langle F_i J; {}^3\Sigma_g^- || \mu || N; {}^1\Sigma_g^+ \rangle, \end{aligned} \quad (7.11)$$

with the reduced matrix element

$$\begin{aligned} \langle F_i J; {}^3\Sigma_g^- || \mu || N; {}^1\Sigma_g^+ \rangle &= \sum_{N', \Omega} a_{N'}^{F_i} \sqrt{(2N+1)(2N'+1)} \begin{pmatrix} J & 1 & N \\ -\Omega & \Omega & \Omega'=0 \end{pmatrix} \\ &\times \begin{pmatrix} J & 1 & N' \\ -\Omega & \Omega & \Lambda=0 \end{pmatrix} \langle {}^3\Sigma_{g, \Omega=\Sigma}^- | \hat{\mu}_{k=\Omega}^{BF} | {}^1\Sigma_g^+ \rangle. \end{aligned} \quad (7.12)$$

We use these reduced matrix elements to calculate integrated line cross sections [74]

$$I_{F_i,J,N} = \frac{8\pi^3 \tilde{\nu}_{F_i,J,N}}{(4\pi\epsilon_0)3hc^3 Z} (2J+1) \exp\left\{\frac{-hc\tilde{\nu}_{F_i,J}^{(X)}}{k_B T}\right\} |\langle F_i, J; {}^3\Sigma_g^- || \mu || N; {}^1\Sigma_g^+ \rangle|^2, \quad (7.13)$$

that can be compared to experimental results. Here $I_{F_i,J,N}$ is in unit length per molecule, $\tilde{\nu}_{F_i,J,N}$ the wavenumber of the transition, h Planck's constant, c the speed of light, ϵ_0 the vacuum permittivity constant, Z the partition sum of molecular oxygen [109], $hc\tilde{\nu}_{F_i,J}^{(X)}$ the energy of state $|F_i J; {}^3\Sigma_g^- \rangle$, k_B the Boltzmann constant, and T the absolute temperature.

The final step is the calculation of the body-fixed electronic $\langle {}^3\Sigma_{g,\Omega=\Sigma}^- | \hat{\mu}_{k=\Omega}^{BF} | {}^1\Sigma_g^+ \rangle$ matrix element, which is extensively treated in [108]. For completeness, we include part of the explanations for notational consistency. Spin-orbit coupling will perturb both electronic states in the matrix element of Eq. 7.12. Other states are mixed in according to the selection rules of the spin-orbit operator [110], relevant to this case are: $\Delta\Omega = 0, \Delta S = 0, \pm 1$ and $g \leftrightarrow g$. Together with the selection rules of the magnetic dipole operator [105], among others $\Delta S = 0, g \leftrightarrow g, + \leftrightarrow +$ and $- \leftrightarrow -$ the states of importance can be determined.

For the orbital momentum part of the magnetic dipole operator of Eq. 7.9, the matrix element (including spin-orbit coupling to first order in the wavefunction) is given by

$$\begin{aligned} \langle {}^3\Sigma_{g,\Omega}^- | \sum_i \hat{l}_{\pm,i} | {}^1\Sigma_g^+ \rangle &= \sum_{n,n'} \frac{\langle {}^3\Sigma_{g,\Omega=\pm 1}^- | \hat{H}_{SO} | n, {}^1\Pi_{g,\Omega=\pm 1}^+ \rangle}{E_X - E_{\Pi}(n)} \langle n, {}^1\Pi_{g,\Omega=\pm 1}^+ | \sum_i \hat{l}_{\pm,i} | {}^1\Sigma_g^+ \rangle \\ &+ \langle {}^3\Sigma_{g,\Omega=\pm 1}^- | \sum_i \hat{l}_{\pm,i} | n', {}^3\Pi_{g,\Omega=0}^- \rangle \frac{\langle n', {}^3\Pi_{g,\Omega=0}^- | \hat{H}_{SO} | {}^1\Sigma_g^+ \rangle}{E_{\Pi}(n') - E_b}. \end{aligned} \quad (7.14)$$

Here E_X and E_b are the energies of the ground and b states of oxygen, $E_{\Pi}(n)$ and $E_{\Pi}(n')$ are energies of the $n(n')$ -th Π state of the corresponding symmetry. The explanation for this result is as follows; if the end state of the transition dipole element is the ${}^1\Sigma_g^+$ state, the ${}^3\Sigma_{g,\Omega=0}^-$ ground state should obtain $+, g$, and $S = 0$ character. Consequently, Λ should be ± 1 for a non-zero matrix element of the $\sum_i \hat{l}_i$ operator. This leads to the ${}^1\Pi_g^+$ state symmetry. Starting from the spin-orbit perturbed b state, the requirements are: $-, g, \Omega = 0, \Lambda = \pm 1, S = 1$. The intermediate state should have ${}^3\Pi_{g,\Omega=0}^-$ state symmetry.

For the spin part of the magnetic dipole operator only matrix elements with the spin-orbit perturbed b state can lead to a non-zero result for the $\sum_i \hat{s}_i$ operator. This

leads to the requirements: $-, g, \Omega = 0, S = 1,$ and $\Lambda = 0$. The spin-orbit coupled state is ${}^3\Sigma_{g,\Omega=0}^-$. The main intensity borrowing of the magnetic dipole transition is due to this contribution

$$\langle {}^3\Sigma_g^- | \sum_i \hat{s}_{\pm,i} | {}^1\Sigma_g^+ \rangle = \langle {}^3\Sigma_{g,\Omega=\pm 1}^- | \sum_i \hat{s}_{\pm,i} | {}^3\Sigma_{g,\Omega=0}^- \rangle \frac{\langle {}^3\Sigma_{g,\Omega=0}^- | \hat{H}_{SO} | {}^1\Sigma_g^+ \rangle}{E_X - E_b}. \quad (7.15)$$

The calculation of this matrix element, including averaging over the vibrational coordinate, is done in [108]. Their matrix elements are related to ours via

$$\mp \langle {}^3\Sigma_{g,\Omega=\pm 1}^- | \sum_i \hat{l}_{\pm,i} + g_e \hat{s}_{\pm,i} | {}^1\Sigma_g^+ \rangle = \langle X {}^3\Sigma_{g,y}^- | L_x + g_e S_x | b {}^1\Sigma_g^+ \rangle = 0.0268 \mu_B. \quad (7.16)$$

7.2.3 Spectrum in the impact approximation

The rotationally resolved A-band magnetic dipole absorption spectrum concerns transitions of the type $|N; {}^1\Sigma_g^+ \rangle \leftarrow |F_i, J; {}^3\Sigma_g^- \rangle$, both vibrational ground states. In the impact approximation it is assumed that strong collisions, which change the absorber's wavefunction significantly, are well separated in time [84]. This approximation is combined with the assumption that the perturbing particles do not interact with each other, and that the absorbers experience an isotropic gas surroundings. Collisional effects on the spectrum are then described in terms of binary collisions of absorber and perturber. The collision dynamics is captured in elastic and inelastic scattering amplitudes. The expression for the spectrum becomes invariant with respect to the magnetic quantum levels. This leads to the expression for the magnetic dipole absorption spectrum in unit length squared per molecule [74, 88, 89, 91, 111]

$$F(\tilde{\nu}) = \frac{1}{\pi} \frac{8\pi^3 \tilde{\nu}}{(4\pi\epsilon_0)3hc^3} \text{Im} \left\{ \sum_{F'_i, J', N'; F_i, J, N} \langle F'_i, J'; {}^3\Sigma_g^- | |\mu| | N'; {}^1\Sigma_g^+ \rangle^* \right. \\ \left. [\mathbf{A}^{-1}]_{F'_i, J', N'; F_i, J, N} P_{F_i, J} \langle F_i, J; {}^3\Sigma_g^- | |\mu| | N; {}^1\Sigma_g^+ \rangle \right\}. \quad (7.17)$$

$\text{Im}\{\dots\}$ means the imaginary part of the expression in the brackets, see Eq. 7.13 for further explanation of the constants. A set of quantum numbers F_i, J, N identifies a spectral line as the initial and final state of the transition. The primed version of these quantum numbers indicates the coupling of two spectral lines by inelastic collisions known as line-mixing.

The elements of the population matrix are given by

$$P_{F_i, J} \equiv \frac{(2J+1)}{Z} \exp \left\{ -\frac{hc\tilde{\nu}_{F_i, J}^{(X)}}{k_B T} \right\} \delta_{J, J'} \delta_{F_i, F'_i}, \quad (7.18)$$

with ground state energies $hc\tilde{\nu}_{F_i, J}^{(X)}$ from diagonalisation of the molecular Hamiltonian [107], with spectroscopic constants given in Tab. 7.1, and $\delta_{X, X'}$ a Kronecker delta.

The elements of matrix \mathbf{A} in Eq. 7.17 are given by

$$A_{F'_i, J', N'; F_i, J, N} = [\tilde{\nu} - \tilde{\nu}_{F_i, J, N}] \delta_{J, J'} \delta_{F_i, F'_i} \delta_{N, N'} - \frac{in}{2\pi c} \left\langle v\sigma_{F'_i, J', N'; F_i, J, N} \right\rangle, \quad (7.19)$$

with i the imaginary number, n the number density (particles per unit volume) of the perturbers, c the speed of light, $\tilde{\nu}_{F_i, J, N}$ transition wavenumbers, and $\langle v\sigma_{F'_i, J', N'; F_i, J, N} \rangle$ the relaxation matrix elements (unit volume per second), including a thermal average over collision energies E_c according to

$$\langle v\sigma_{\dots} \rangle = \left(\frac{8k_B T}{\mu\pi} \right)^{1/2} \left(\frac{1}{k_B T} \right)^2 \int_0^\infty E_c [\sigma_{\dots}^+(E_c) + \sigma_{\dots}^-(E_c)] \exp \left\{ -\frac{E_c}{k_B T} \right\} dE_c, \quad (7.20)$$

with $\dots = F'_i, J', N'; F_i, J, N$, and the cross sections given by

$$\begin{aligned} \sigma_{F'_i, J', N'; F_i, J, N}^\pm(E_c) &= \frac{\pi}{2\mu E_c} \sum_{J_{\text{tot}}^{(b)}, J_{\text{tot}}^{(X)}, l'_\pm, l_\pm} (-1)^{J-J'} \sqrt{\frac{2J'+1}{2J+1}} \\ &\times (2J_{\text{tot}}^{(b)}+1)(2J_{\text{tot}}^{(X)}+1) \begin{Bmatrix} J & 1 & N \\ J_{\text{tot}}^{(b)} & l_\pm & J_{\text{tot}}^{(X)} \end{Bmatrix} \begin{Bmatrix} J' & 1 & N' \\ J_{\text{tot}}^{(b)} & l'_\pm & J_{\text{tot}}^{(X)} \end{Bmatrix} \\ &\times \left[\delta_{F_i, F'_i} \delta_{J, J'} \delta_{N, N'} \delta_{l_\pm, l'_\pm} - S_{N', l'_\pm; N, l_\pm}^{J_{\text{tot}}^{(b)}, *}(E_c) S_{F'_i, J', l'_\pm; F_i, J, l_\pm}^{J_{\text{tot}}^{(X)}}(E_c) \right]. \end{aligned} \quad (7.21)$$

Here μ is the reduced mass of the perturber-absorber complex, l_+ and l_- are even and odd partial wave quantum numbers, and $J_{\text{tot}}^{(X)}$ and $J_{\text{tot}}^{(b)}$ are the total angular momentum quantum numbers of the collisional complexes with the two relevant electronic states of oxygen. The scattering matrix elements $S_{\dots}^{\dots}(E_c)$ contain the dynamics information of the binary collisions and are the product of solving the coupled-channels equations [107]. S matrix elements for both potentials should be calculated at exactly the same collision energy E_c , with respect to the initial and final states of the magnetic dipole transition.

Note that the incoming l and outgoing l' partial waves are the same for both oxygen states, this is a consequence of the assumption that the absorbing molecule is in an isotropic gas [88, 89]. Solutions of the coupled-channels equations for our problem have a well defined parity of $(-1)^{N+l+1}$ for the ground state and $(-1)^{N+l}$ for the b state, which allows a separate scattering calculation for odd and even parity. Consequently, this is also possible for Eq. 7.21. This is the reason for the distinction between even l_+ and odd l_- partial wave quantum numbers.

To conclude, the spectrum that follows from Eq. 7.17 becomes a complex shape if spectral lines are coupled to each other by inelastic collisions, represented by non-zero off-diagonal relaxation matrix elements (Eqs. 7.20 and 7.21). If, however, spectral lines are not coupled to each other, Eq. 7.17 becomes a sum of Lorentzian line shapes

$$F(\tilde{\nu}) = \frac{1}{\pi} \frac{8\pi^3 \tilde{\nu}}{(4\pi\epsilon_0)3hc^3} \sum_{F_i, J, N} \frac{|\langle F_i, J; {}^3\Sigma_g^- || \mu || N; {}^1\Sigma_g^+ \rangle|^2 P_{F_i, J}}{(\tilde{\nu} - \tilde{\nu}_{F_i, J, N} + nd_{F_i, J, N})^2 + (nw_{F_i, J, N})^2}. \quad (7.22)$$

The width $w_{F_i, J, N}$ and shift $d_{F_i, J, N}$ of these lines are equal to the real and imaginary parts of $\langle v\sigma_{F_i, J, N; F_i, J, N} \rangle / 2\pi c$ in Eq. 7.19.

7.3 He-O₂(*b*¹Σ_g⁺) interaction potential

7.3.1 *Ab initio* methods

The potential was calculated using the MOLPRO [114] package. A basis set consisting of an augmented correlation consistent triple zeta (aug-cc-pVTZ) basis [115, 116, 117] on the He and O atoms, and an additional set of (*3s3p2d1f*) bond functions defined by Tao and Pan [118] was used. These bond functions are placed on the intersection of the vector R , see Fig. 7.1, and the ellipse that is chosen such that the bond functions

constant	$X^3\Sigma_g^-$ [112]	$b^1\Sigma_g^+$ [113]
B_0	1.437675	1.391247
D_0	$4.790 \cdot 10^{-6}$	$5.375 \cdot 10^{-6}$
λ_{SS}	1.984751	–
λ_{NS}	$-8.425 \cdot 10^{-3}$	–

Table 7.1: Spectroscopic constants in cm⁻¹ used in this work. B_0 and D_0 are the rotational and distortion constant of the vibrational ground state, and λ_{SS} and λ_{NS} the spin-spin and spin-rotation coupling constants.

are centered at the midpoint of R in the T-shape geometry and at the midpoint of the smallest O-He distance in the linear geometry. We apply a correction for the basis set superposition error with the Boys and Bernardi counterpoise procedure [119].

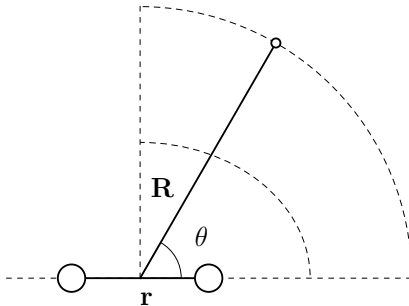


Figure 7.1: Coordinate system for the $\text{He-O}_2(b^1\Sigma_g^+)$ potential, where R and θ parameterise the vector that connects the centre of mass of the oxygen molecule to the helium atom. The interatomic distance r is fixed in the calculation of the interaction potential. The position of the bond functions is indicated by the inner dashed ellipse.

The ground state potential, which was taken from the literature [120], was calculated with the partially spin-restricted open-shell single and double excitation coupled cluster method [121] with perturbative triples [122] [RCCSD(T)] method. This is, however, not possible for the b state since two states of A' symmetry (C_s point group) are involved that correlate with the $^1\Sigma_g^+$ and $^1\Delta_g$ states of the free oxygen molecule. To obtain an interaction potential of approximately the RCCSD(T) quality, a correction was devised as discussed below.

We used the complete active space self consistent field [123, 124] (CAS-SCF) program to distinguish the 4 lowest states of oxygen: $X^3\Sigma_g^-$, $a^1\Delta_g$ (A' and A'' symmetry), and $b^1\Sigma_g^+$. All core orbitals were used in the active space to avoid problems with the convergence of the calculation at small He- O_2 distances. The resulting orbitals of a CAS-SCF calculation were used as starting orbital guess for each subsequent geometry, starting at large He- O_2 distance. The canonical orbitals corresponding to the He- $\text{O}_2(a^1\Delta_g)$ and He- $\text{O}_2(b^1\Sigma_g^+)$ complexes with A' symmetry were used as input for a state-averaged complete active space second order perturbation theory [125] (CASPT2) calculation. For every grid point the energy corresponding to the state with the highest reference energy was used for the He- $\text{O}_2(b^1\Sigma_g^+)$ potential. To obtain a potential of approximately RCCSD(T) quality, the difference in energy between the CASPT2

and RCCSD(T) calculations for He-O₂(X³Σ_g⁻) was subtracted from the CASPT2 He-O₂(b¹Σ_g⁺) potential at each geometry.

7.3.2 *Ab initio* grid

The interaction energy was calculated for 532 geometries. A rotational constant of $B_0=1.3912 \text{ cm}^{-1}$ [113] was used to fix the vibrational coordinate r to a value of $r_0=2.326 \text{ a}_0$. The radial grid (in atomic units) was spaced with steps of 0.2 from 2.9 to 8.1 and extended logarithmically with $R_{i+1}/R_i=1.1$ from 8.5 to 20.05, with one extra point at 25. The angular grid was confined to the range of 0° to 90°, and consisted of 14 Gauss-Legendre quadrature points.

7.3.3 The fit of the potential

The interaction potential $V(R, \theta)$ was first expanded in Legendre polynomials of even order,

$$V(R, \theta) = \sum_{l=0,2,\dots}^{12} C_l(R) P_l(\cos \theta). \quad (7.23)$$

The radial coefficients were obtained via a Gauss-Legendre quadrature

$$C_l(R) = \sum_{i=1}^{14} (2l+1) w_i V(R, \theta_i) P_l(\cos \theta_i), \quad (7.24)$$

with $0 \leq \theta_i \leq \frac{\pi}{2}$ and w_i the quadrature points and their corresponding weights. After performing the 14-point quadrature of Eq. 7.24, the *ab initio* points could be reproduced via Eq. 7.23 with relative errors on the order of 0.1% in the barrier at small R and 0.01% and less near the potential well and at larger R .

To obtain a fit of the radial coefficients $C_l(R)$, the fit function was split in a long range part $C_l^{(\text{lr})}(R)$ and short range part $C_l^{(\text{sr})}(R)$

$$C_l(R) = C_l^{(\text{sr})}(R) + C_l^{(\text{lr})}(R). \quad (7.25)$$

The long range part is given by

$$C_l^{(\text{lr})}(R) = -\frac{c_{nl} f_n(\beta R)}{R^{-n}}, \quad (7.26)$$

where $n = l + 4$, except for $l = 0$ for which $n = 6$. These are the leading terms in the multipole expansion [126]. The f_n 's are Tang-Toennies damping functions [127]

$$f_n(x) = 1 - e^{-x} \sum_{k=0}^n \frac{x^k}{k!}. \quad (7.27)$$

To obtain a reliable fit of the c_{nl} coefficients in Eq. 7.26, we set the damping functions to 1 and performed a weighted least squares fit of $C_l(R)$ for $R \geq 10 a_0$. The weighting function was set to R^n with n in accordance with Eq. 7.26. The first three coefficients are given in Tab. 7.2. We then chose $\beta = 2.0$ for $C_l^{(\text{lr})}(R)$ in Eq. 7.26 and obtained

l	n	$c_{n,l}$
0	6	10.26
2	6	2.44
4	8	-3.19

Table 7.2: Fitted leading term coefficients of Eq. 7.26 in E_h/a_0^n .

$C_l^{(\text{sr})}(R)$ in Eq. 7.25, by subtraction of $C_l^{(\text{lr})}(R)$ from the *ab initio* points. For the short range part, the reproducing kernel Hilbert space (RKHS) method with the reproducing kernel for distance-like variables was used [128, 129]. The RKHS parameter m was set to the leading term parameter n minus 1 and the RKHS smoothness parameter was set to 2.

After the RKHS fitting, reconstruction of $V(R, \theta)$ via Eqs. 7.23 and 7.25 reproduced the *ab initio* points with a relative error of the order of 0.01% or better for R larger than $4 a_0$. This was also the case for 35 randomly chosen geometries not used for the fit. In the region of $2.9 < R < 4.0 a_0$ the largest relative error is 0.49%, the barrier to the unphysical region below $2.9 a_0$ of the fitted potential is $\geq 0.05 E_h$ ($\approx 11,000 \text{ cm}^{-1}$).

Figure 7.2 presents contour plots of the newly computed interaction potential for the b state and the potential for the ground state. The b state potential in Fig. 7.2(a) is slightly more anisotropic than the ground state potential of Fig. 7.2(b). The unphysical region of the excited state potential is indicated in grey. The global minimum for the excited state potential is at the T-shaped geometry at $R = 5.9 a_0$ with dissociation energy $D_e = 152.2 \mu E_h$, and for the ground state $D_e = 127.1 \mu E_h$ at $R = 6.0 a_0$. The local minimum for the excited state at the linear geometry has a well depth of $123.7 \mu E_h$ at $R = 6.9 a_0$, and for the ground state $116.7 \mu E_h$ at $R = 6.9 a_0$.

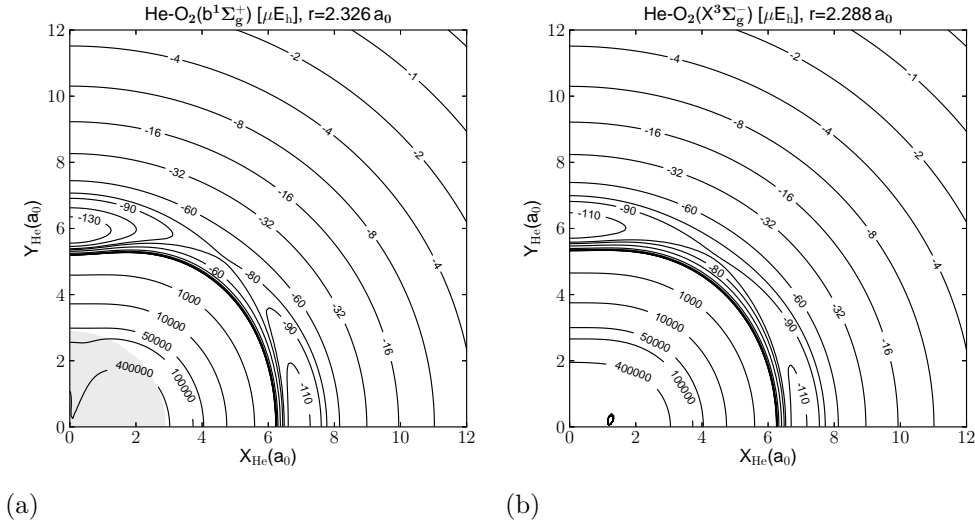


Figure 7.2: The two potential surfaces, in μE_h , used in the scattering calculations, with the O–O distance r indicated in the titles. The molecular axis of the oxygen molecule is parallel to the X_{He} axis. (a) The computed $\text{He-O}_2(b^1\Sigma_g^+)$ interaction potential, unphysical region indicated in grey. (b) The $\text{He-O}_2(X^3\Sigma_g^-)$ interaction potential from [120].

7.4 Scattering calculations

In order to obtain the S matrix elements needed for Eq. 7.21 we solved the coupled-channels equations using the renormalised Numerov method [130], with matrix elements in a Hund’s case b basis as provided in [107]. All scattering code was written in MATLAB [131]. The equations were integrated per parity, see section 7.2.3, and per J_{tot} in a Hund’s case b basis. The solutions were then matched to asymptotic boundary conditions in a basis of channel eigen functions. The same code was used for the scattering calculations of helium with both the oxygen b and X state.

To test our scattering code we calculated the inelastic cross sections reported in [106] for the ground state potential as a function of collision energy. This resulted in good agreement for cross sections of the type $N, F_1 \leftarrow 1, F_1$ and $N, F_3 \leftarrow 1, F_1$. The cross sections of type $N, F_2 \leftarrow 1, F_1$, however, disagreed with an overall factor. The difference in these results could be explained by a mistake in the code used for the work of [106], an erratum will be published.

Both ground and b state S matrix elements should be calculated at the same collision energy. A full scattering calculation was thus required per target state, initial or final

state of the transition, per collision energy. The total energy, the sum of the target state energy and the collision energy, determined the basis set size used for the scattering calculations. For the ground state we used the same settings as in [106], and for the b state we used $N \leq 12$ for total energies up to 30 cm^{-1} , $N \leq 14$ for total energies up to 50 cm^{-1} , $N \leq 16$ for total energies up to 100 cm^{-1} , $N \leq 18$ for total energies up to 200 cm^{-1} , $N \leq 22$ for total energies up to 300 cm^{-1} , $N \leq 24$ for total energies up to 500 cm^{-1} , $N \leq 26$ for total energies up to 750 cm^{-1} , $N \leq 30$ for total energies up to 1000 cm^{-1} and $N \leq 32$ for total energies up to 2500 cm^{-1} .

The step size for the propagation was set to 10 steps per de Broglie wavelength and the maximum propagation radius was set to $20 a_0$ for collision energies $\leq 600 \text{ cm}^{-1}$, $18 a_0$ for $\leq 1600 \text{ cm}^{-1}$, and $16 a_0$ for $>1600 \text{ cm}^{-1}$. The propagation radii were determined by visual inspection of the convergence of the diagonal S matrix elements as a function of the propagation radius for a range in J_{tot} 's and a selection of total energies. This criterion is used since S matrix elements for both potentials should be of the same quality. The convergence criterion was a change in magnitude of the complex number that is less than 10^{-4} and ϕ for the complex phase less than 3 degrees. The highest target state incorporated in the calculations of the spectrum are for the oxygen ground state $J = 16$, and for the b state $N = 16$.

The convergence criterion for J_{tot} during the scattering calculations, was that the average absolute value of the transition matrix elements $(1-S)$ should become smaller than 10^{-4} for two values of J_{tot} separated by a preset step size. This convergence criterion is sensitive to the magnitude of the S matrix elements, and was chosen regarding that a product of S matrix elements for both potentials is present in Eq. 7.21. The J_{tot} step size for the ground state scattering was set to 5 and for the b state to 6. Typical maximum values of J_{tot} were 20 for scattering energies on the order of 10 wave number, and 150 for scattering energies above 1600 wave number, depending on the target state.

The spectrum, Eq. 7.17, requires a thermal average over collision energies of the relaxation matrix Eq. 7.21. For this averaging a grid of collision energies in cm^{-1} was used that started at 1 in steps of 0.5 up to 50 and from 50 in steps of 5 to 200, from 200 in steps of 25 to 1000 and from 1000 in steps of 100 to 1900. This grid was used for a trapezoidal integration to obtain the thermally averaged relaxation matrix elements.

7.5 Cavity ring-down experiments*

7.5.1 The experimental setup

The cavity ring-down spectroscopy [132, 133] setup used in this experiment is illustrated in Fig. 7.3, and is almost identical to the setup used in [134]. An optical cavity was constructed inside a pressure cell using two mirrors with a reflectivity above 99.99% (Research electro optics) that are separated by approximately 350 mm, resulting in an effective absorption path length of 3.5 km. The mirrors have a radius of curvature of 1000 mm. As a light source, we used a continuous wave external cavity diode laser (Toptica DL100) with a power of about 50 mW and a wavelength around 770 nm. The line width of this laser is on the order of 10^{-4} cm^{-1} . The line width and wavenumber of the laser were determined with a wavelength meter (Ångström HighFinesse WS/R7-11).

Each measurement commenced with emptying our pressure cell to a pressure of a few millibar using a membrane pump (Pfeifer Vacuum MVP 055-3). Subsequently, we slowly filled the pressure cell with a mixture of 14.65% O₂ (Linde gas, 99.9999% purity) and 85.35% He (Linde gas, 99.999% purity) using two flow controllers (Bronkhorst High-Tech). Additional measurements were performed using an in-house premixed bottle containing $1.00 \pm 0.01\%$ O₂ in helium. During measurements, the wavelength is kept fixed at a position where the contribution of spectral lines of the molecular oxygen isotopologues is expected negligible. We achieved coupling of the light to the cavity modes using small current variations in the diode, as well as small variations in the cavity alignment created by slowly filling the cell with gas. This procedure adds an uncertainty in the wavelength of about one free spectral range of the cavity (0.016 cm^{-1}). We continuously measured the pressure inside the cell with a diaphragm pressure detector (Pfeiffer Vacuum D-35614), accuracy 0.3%. We detected the light leaking out of the cavity with an avalanche photodiode (APD, Licel GmbH LP-1A series). When the intensity behind the cavity reaches a threshold of approximately 40% of the maximum possible intensity in the cavity, the laser was disabled within $1 \mu\text{s}$ for a period of approximately $200 \mu\text{s}$ by a home-built electronic switch. We simultaneously recorded the ring-down signal, the pressure, and the laser current with an oscilloscope (HP infinium). All experiments were performed at a temperature of $293 \pm 1 \text{ K}$.

*All cavity ring-down experiments were performed by Dr. Frans R. Spiering.

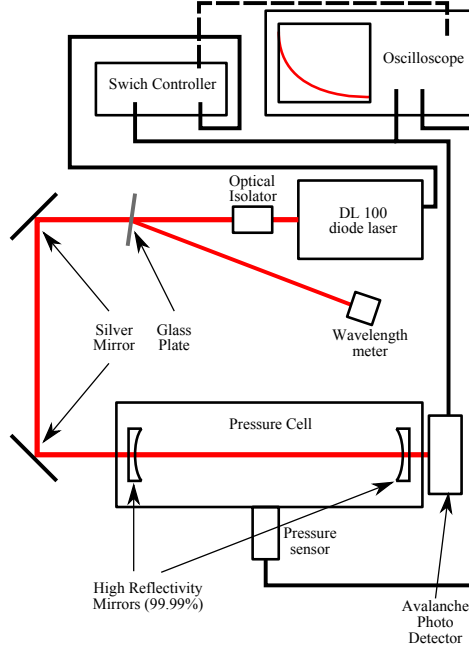


Figure 7.3: The cavity ring-down setup used for the determination of pressure dependent extinction. Light from the DL100 laser diode is coupled into the optical ring-down cavity, and is partly used for the determination of the wavelength. The light leaking out of the cavity is detected using an avalanche photo diode. When the detected signal reaches a threshold, the switch controller switches the laser off and provides a trigger for the oscilloscope. The oscilloscope captures the exponentially decaying signal detected by the avalanche photo diode as well as the pressure measured by the pressure sensor.

7.5.2 Data processing

The ring-down signals as a function of time t and threshold laser intensity $I_0(\tilde{\nu})$ were fitted by an exponent of the form [98]

$$I(t) = I_0(\tilde{\nu}) \exp \left\{ -\frac{t}{\tau(\tilde{\nu})} \right\}, \quad (7.28)$$

with $\tau(\tilde{\nu})$ the characteristic ring-down time given by

$$\tau(\tilde{\nu}) = \frac{d}{c} \frac{1}{|\ln(\mathcal{R})| + \kappa(\tilde{\nu})d}. \quad (7.29)$$

Here d is the cavity length, c the speed of light, \mathcal{R} the reflectivity of the mirrors and $\kappa(\tilde{\nu})$ the extinction coefficient. The extinction coefficient is understood to consist of

contributions from: Rayleigh scattering [135], collision induced absorption (CIA) [102], and magnetic dipole absorption, that are summed respectively [98]

$$\kappa(\tilde{\nu}) = \sigma(\tilde{\nu})n_{\text{O}_2} + c(\tilde{\nu})n_{\text{O}_2}^2 + \alpha(\tilde{\nu}). \quad (7.30)$$

Here n_{O_2} is the number density in amagat of molecular oxygen, and $\sigma(\tilde{\nu})$ and $c(\tilde{\nu})$ are coefficients that are known from the literature for the Rayleigh scattering and CIA, respectively. To provide the reader with a feeling for the contribution of each mechanism to the spectrum, Fig. 7.4 illustrates the construction of the pure oxygen A-band extinction based on the sum of the data of each of these contributions. The illustration was taken from [98].

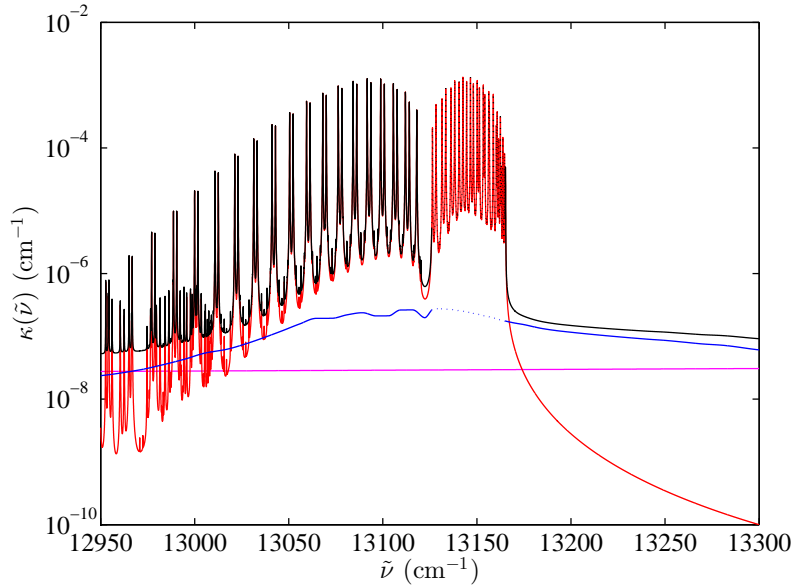


Figure 7.4: Construction of the extinction $\kappa(\tilde{\nu})$ of molecular oxygen gas (black) at a density of 1 amagat in the A-band region from the summed contributions of: Rayleigh scattering (purple), magnetic dipole absorption (red), and CIA (blue). The dashes in the region of the R branch indicate the CIA is not determined here. The illustration was taken from [98].

To obtain the magnetic dipole absorption $\alpha(\tilde{\nu})$ from Eq. 7.30 we subtracted the Rayleigh scattering and CIA for oxygen. For the index of refraction and the King correction factor (molecular anisotropy) [136], the paper by Bates [137] was used. This data is validated to give the correct scattering intensities [138, 139, 140]. Due to the low

refractive index of helium, its Rayleigh scattering is negligible. The CIA contribution was subtracted from the data by Tran *et al.* [100]. Their data was interpolated using a cubic spline, and has been validated by independent measurements [98, 101]. The CIA of helium-oxygen is neglected, based on yet unpublished data measured with our cavity ring-down setup. Coefficients $\sigma(\tilde{\nu})$ and $c(\tilde{\nu})$ used for Eq. 7.30 are tabulated in the Results section.

7.6 Results and Discussion

In this section the calculated results for the rotationally resolved A-band spectrum are presented. The first focus is on the predictions of the integrated line cross sections for molecular oxygen that are compared to experimental results from the literature. These integrated cross sections depend on the magnetic dipole transition matrix elements for molecular oxygen only, and do not include collisional effects.

Subsequently, the calculated results for the pressure broadening coefficients are shown and compared to experimental results from the literature. The width of the spectral lines is relatively insensitive to the effect of line-mixing, hence line-mixing is not included in these calculations.

Finally, the effect of the line-mixing mechanism is studied by the prediction of pressure-dependent absolute absorption strengths in the valleys between spectral lines. As will be shown, the difference between including and neglecting the line-mixing becomes most pronounced in these regions. When the line-mixing is neglected, the spectrum is a sum of Lorentzian line shapes according to Eq. 7.22. The results of the calculations are compared to the cavity ring-down data.

For the discussion a designation of the spectral lines of transition type $|N'M'_N; {}^1\Sigma_g^+\rangle \leftarrow |F''_i J'' M''_j; {}^3\Sigma_g^-\rangle$ (section 7.2.2) should be defined. Here we use ${}^{\Delta N} \Delta J(N'')$, with N'' the nuclear rotation quantum number in Eqs. 7.2, 7.3, and 7.4, depending on the choice for F_i as the initial state of the magnetic dipole transition. Furthermore, $\Delta N \equiv N' - N''$ and $\Delta J \equiv N' - J''$, with $\Delta X = -1, 0, 1$ corresponding to P, Q, R , respectively. Hence designations, such as ${}^P Q(3)$ or ${}^R R(3)$.

7.6.1 Integrated line cross sections

Table 7.3 shows a comparison between our integrated line cross sections calculated with Eq. 7.13, and experimentally determined cross sections for the P branch [141]. These integrated cross sections test the magnetic dipole transition matrix elements for molecular oxygen, excluding any collisional effects. The experiments were performed

in a pressure range from 1.4 to 4.6 kPa (≈ 0.013 to 0.045 atm) on a 2% oxygen mixture with nitrogen. The partition sum $Z = 215.77$ (at a temperature of 296 K) and the transition wavenumbers $\tilde{\nu}_{F_i, J, N}$ of Eq. 7.13 were taken from the literature [109, 142] based on data from the Hitran database. Calculated and experimental values agree to within 1% for line positions close to the A-band origin, and deviate increasingly for line positions further in the P branch. The maximum disagreement is 2.5% for the ${}^PQ(15)$ line.

line	${}^PQ(3)$	${}^PP(3)$	${}^PQ(5)$	${}^PP(5)$	${}^PQ(7)$	${}^PP(7)$	${}^PQ(9)$
[141]	3.901(8)	5.738(8)	5.974(9)	7.557(9)	7.098(9)	8.423(10)	7.256(8)
calc.	3.887	5.717	5.966	7.558	7.093	8.400	7.263
line	${}^PP(9)$	${}^PQ(11)$	${}^PP(11)$	${}^PQ(13)$	${}^PP(13)$	${}^PQ(15)$	
[141]	8.262(8)	6.667(7)	7.437(7)	5.608(5)	6.113(5)	4.338(4)	
calc.	8.276	6.661	7.402	5.575	6.088	4.303	

Table 7.3: Comparison of experimental [141] and calculated (Eq. 7.13, $T = 296$ K) integrated line intensities in units of 10^{-24} cm molecule $^{-1}$. Numbers in parenthesis are 1σ standard deviations in the unit of the last digit.

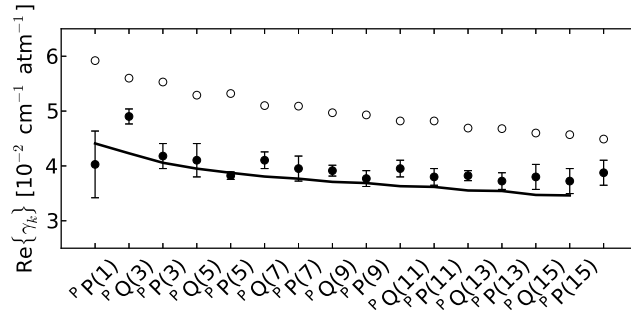
7.6.2 Pressure broadening coefficients

The first test for collisional effects is the prediction of helium-O₂ broadening and shifting coefficients of the spectral lines in the A-band spectrum. These coefficients represent the linear dependence of the line widths and shifts on the, in this case, helium density. The broadening coefficients have been determined experimentally, and are reported in the literature [143]. The line shift coefficients, however, were too small to determine accurately. The effect of line-mixing on the line widths is expected to be negligible, since there is no significant overlap between spectral lines at the relatively low pressures for which the experiments were carried out (0.26 atm O₂ partial pressure and a range of 0.13 to 0.52 atm helium pressure). If line-mixing is neglected the spectrum becomes a sum of Lorentz lines as given in Eq. 7.22. The widths and shifts of these lines are the real and imaginary parts of the diagonal elements of the calculated relaxation matrix of Eq. 7.20. We define the coefficients γ_k for the k -th spectral line in units of cm $^{-1}$ atm $^{-1}$ for comparison with the experiment (k corresponds to a set of quantum numbers N' ,

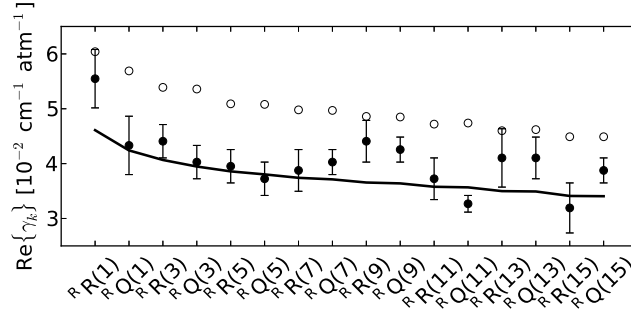
F_i'', J'' of the transition)

$$\gamma_k \equiv \frac{1}{2\pi c} \frac{1}{p_0} \frac{T_0}{T} N_L \langle v \sigma_{k;k} \rangle. \quad (7.31)$$

Here $p_0 = 1$ atm, $T_0 = 273.15$ K, N_L is Loschmidt's number ($2.6867774 \cdot 10^{25}$ particles m^{-3} for an ideal gas at 0°C and 1 atm), and $\langle v \sigma_{k;k} \rangle$ is $\langle v \sigma_{F_i, J, N; F_i, J, N} \rangle$ of Eq. 7.20. The real and imaginary part of γ_k represent the broadening and shifting coefficients of spectral line k .



(a) P branch pressure broadening coefficients



(b) R branch pressure broadening coefficients

Figure 7.5: Comparison between experimentally determined line broadening coefficients for helium- O_2 [143] (closed black dots with 1σ error bars), and the real part of Eq. 7.31 (black line), with $T = 298$ K for the P and R branches of the spectrum. The open black dots are experimentally determined oxygen self-broadening coefficients [144]. These are used in the calculations of the absorption strengths in section 7.6.3. Uncertainties for these coefficients [144] are of the order $10^{-4} \text{ cm}^{-1} \text{ atm}^{-1}$ and are not visualised.

Figure 7.5 shows that the calculated broadening coefficients follow a smooth line and capture the trend and magnitude of the experimentally determined coefficients. The apparent structure in the experimental points of Fig. 7.5 is not reproduced, but it is not obvious that this structure is significant. One argument in favour of our calculated trend, is that the measured oxygen self-broadening coefficients, indicated with the open black dots, display the same trend (almost by an overall factor of 4/3). The reported uncertainties for these coefficients [144] are of the order $10^{-4} \text{ cm}^{-1} \text{ atm}^{-1}$ and are not visualised. These self-broadening coefficients will be used for the calculation of the absolute absorption strengths in section 7.6.3.

The pressure shifts that follow from the imaginary part of Eq. 7.31 are shown in Fig. 7.6. All shift coefficients have the same sign, and have a magnitude smaller than what could experimentally be determined by the spectrometer used by [143]. It should be noted that the present theory does not exactly satisfy detailed balance. This is known to affect the imaginary part of the relaxation matrix in particular [85, 86].

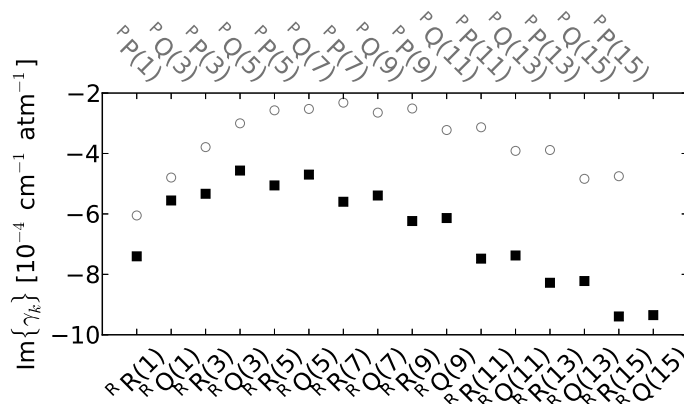


Figure 7.6: Calculated pressure shift coefficients, the imaginary part of Eq. 7.31 at $T = 298 \text{ K}$. Coefficients for the P and R branch are indicated in grey open dots and black closed dots respectively.

7.6.3 Pressure-dependent absorption strengths

The results shown so far, prove that the strong absorption features of the calculated and experimental spectrum are in good agreement. The next step is to study the weak features of the spectrum, that are most sensitive to the effects of line-mixing. A

comparison between theory and experiment will put the line-mixing incorporated in the current theory to the test. Here one tests the formalism and especially the off-diagonal elements in the relaxation matrix.

For this comparison one should look at the spectrum to find out where line-mixing becomes most apparent. Hereto, we calculated a part of the A-band spectrum using Eq. 7.17. The transition wavenumbers $\tilde{\nu}_{F_i, J, N}$ for the spectrum, required in Eq. 7.13, were taken from the literature [109, 142] and are based on data from the Hitran database. Since the collisional effects on the experimental spectrum are not solely from the helium-O₂ collisions, but also from O₂-O₂ collisions, the relaxation matrix elements of Eq. 7.19 should be amended to include O₂ self-broadening. The corrected matrix elements, proportional to the helium density n_{He} in amagat, are

$$n \langle v \sigma_{F'_i, J', N'; F_i, J, N}^{\text{He-O}_2, \text{O}_2\text{-O}_2} \rangle \equiv 2\pi c p_0 \frac{T}{T_0} n_{\text{He}} \left(\gamma_{k', k}^{\text{He-O}_2} + \frac{x_{\text{O}_2}}{1 - x_{\text{O}_2}} \gamma_k^{\text{O}_2\text{-O}_2} \delta_{k', k} \right) \quad (7.32)$$

with

$$\gamma_{k', k}^{\text{He-O}_2} \equiv \frac{1}{2\pi c} \frac{1}{p_0} \frac{T_0}{T} N_L \langle v \sigma_{k', k} \rangle, \quad (7.33)$$

with $\langle v \sigma_{k', k} \rangle$ the *ab initio* helium-O₂ relaxation matrix of Eq. 7.20 including off-diagonal elements. The $\gamma_k^{\text{O}_2\text{-O}_2}$ are the experimentally determined oxygen self-broadening coefficients from the literature [144] and are shown in Fig. 7.5. These coefficients only contribute to the relaxation matrix diagonal, which is indicated by the Kronecker delta $\delta_{k', k}$. The x_{O_2} is the fraction of oxygen in the gas mixture used in the experiment. The calculated spectrum is shown as the black line in the central panel of Fig. 7.7. This figure provides the cross sections of oxygen molecules surrounded by helium at a pressure of 5 atm to accentuate the collisional effects. The fraction of x_{O_2} was set to zero.

In Fig. 7.7 we determined the effect of line-mixing by also showing the ratio of this spectrum divided by the spectrum without line-mixing, Eq. 7.22, as a continuous grey line. The ratios 1.0 and 0.7 are indicated as dashed horizontal grey lines. One observes that the effect of line-mixing is strongest in between the lines. Clearly, the strongest effect is found in between the *P* branch (below 13120 cm⁻¹) and the *R* branch (above 13128 cm⁻¹), where line-mixing reduces the absorption cross section. In other minima line-mixing increases the absorption cross section.

Although being a small effect, it is not necessarily insignificant in practice. For example, the maximum of each peak is fully saturated in the Earth's atmosphere that contains about 20% oxygen; hence variations in oxygen content become noticeable by absorption changes in between the lines. To accurately measure the absorption cross sections in between the lines, we employ cavity ring-down spectroscopy as explained in

$\tilde{\nu}$ cm ⁻¹	$c(\tilde{\nu})$ 10 ⁻⁷ cm ⁻¹ amagat ⁻²	$\sigma(\tilde{\nu})$ 10 ⁻⁸ cm ⁻¹ amagat ⁻¹
13081.30	1.90	2.87
13103.13	1.79	2.89
13112.48	1.76	2.89
13116.11	1.87	2.90
13122.48	2.00	2.90
13125.92	1.98	2.91

Table 7.4: Coefficients $c(\tilde{\nu})$ and $\sigma(\tilde{\nu})$ used in Eq. 7.30 to subtract the contributions of CIA and Rayleigh scattering, respectively, from the measured pressure dependent extinction $\kappa(\tilde{\nu})$ at wavenumber $\tilde{\nu}$.

section 7.5. Here the absorption strength expressed in cm⁻¹ is determined as a function of density (pressure) with a sensitivity of about 10⁻⁷ cm⁻¹. By measuring absorption strengths at spectral positions that our theory predicts as sensitive to the effect of line-mixing, we will prove the added value of including line-mixing in the simulation.

The central panel in Fig. 7.7 contains six numbered arrows indicating the spectral positions where the pressure-dependent cavity ring-down measurements were performed. Each numbered arrow has a panel either above or below the central panel that contains the corresponding number in the lower right corner. The fraction of oxygen in the gas mixture is indicated in the upper left corner. Each grey dot in the figure corresponds to one measured ring-down curve. As was discussed in section 7.5, each curve is fitted to obtain the extinction coefficient $\kappa(\tilde{\nu})$. There are between 1000 and 3000 points per panel.

At small n_{He} the points are distributed around zero absorption, which is caused by an offset determined by the reflectivity of the cavity mirrors. The contribution of CIA and Rayleigh scattering were subtracted from these points, as described in section 7.5. The values of the coefficients used for Eq. 7.30 are given in Tab. 7.4. What remains after these corrections is the magnetic dipole absorption strength $\alpha(\tilde{\nu})$. Here the experimental data is shown as a function of the helium density n_{He} .

Each panel contains a continuous line with the absolute predictions of the absorption strength including line-mixing. To link the spectrum $F(\tilde{\nu})$ to the absorption strength we used the relation

$$\alpha(\tilde{\nu}) = x_{\text{O}_2} \frac{T_0}{T} \frac{p}{p_0} N_L F(\tilde{\nu}), \quad (7.34)$$

where the pressure p is directly measured in the cavity ring-down experiment. Note that Eq. 7.32 is used to compute $F(\tilde{\nu})$. The dashed line ignores the line-mixing, the

off-diagonal elements of the relaxation matrix, and comes from a spectrum built as a sum of Lorentzian line shapes. A third line is generated using a semi-empirical model, named Tonkov model after the scientist who developed the model [94, 95]. This model constructs the effect of line-mixing using diagonal properties (observed line broadening parameters) as a basis for predicting the effect of line-mixing, the off-diagonal influence. This model is empirical but highly predictive.

In a number of cases the difference between the present purely *ab initio* and the empirical model is very small. The fifth panel is taken in the minimum of the spectrum of Fig. 7.7, where the effect of line-mixing is largest. Here the experiment positively agrees with the two models that include line-mixing. The difference between the full *ab initio* model and the empirical model is not large enough to allow an experimental test.

7.7 Conclusions

The pressure broadening of the rotationally resolved oxygen A-band spectrum by helium was studied theoretically. To our knowledge this is the first time pressure broadening of an electronic transition of a molecule is treated with a fully quantum mechanical description. A new interaction potential for helium–O₂($b^1\Sigma_g^+$) was computed. This potential and a helium–O₂($X^1\Sigma_g^+$) potential taken from the literature were used for the scattering calculations required to calculate line broadening in the impact approximation. Regarding the spectroscopy of molecular oxygen, accurate integrated line cross sections for 13 spectral lines in the *P* branch were obtained. The line broadening coefficients predicted by the impact approximation treatment are in good agreement with experimental values from the literature. From cavity ring-down experiments absolute absorption strengths were obtained between several spectral lines. Experimental results are in quantitative agreement with those of the calculations. In particular in the region between the *P* and *R* branch it is proven that off-diagonal elements in the relaxation matrix, responsible for line-mixing, are important to obtain a correct description of the absorption strength.

Acknowledgements

The authors thank Ad van der Avoird and Leo Meerts for their aid and suggestions. Francois Lique is thanked for his aid in tracking the source of the difference between his and our scattering results. Leander Gerritsen is thanked for preparation of the gas mixtures used in the experiments.

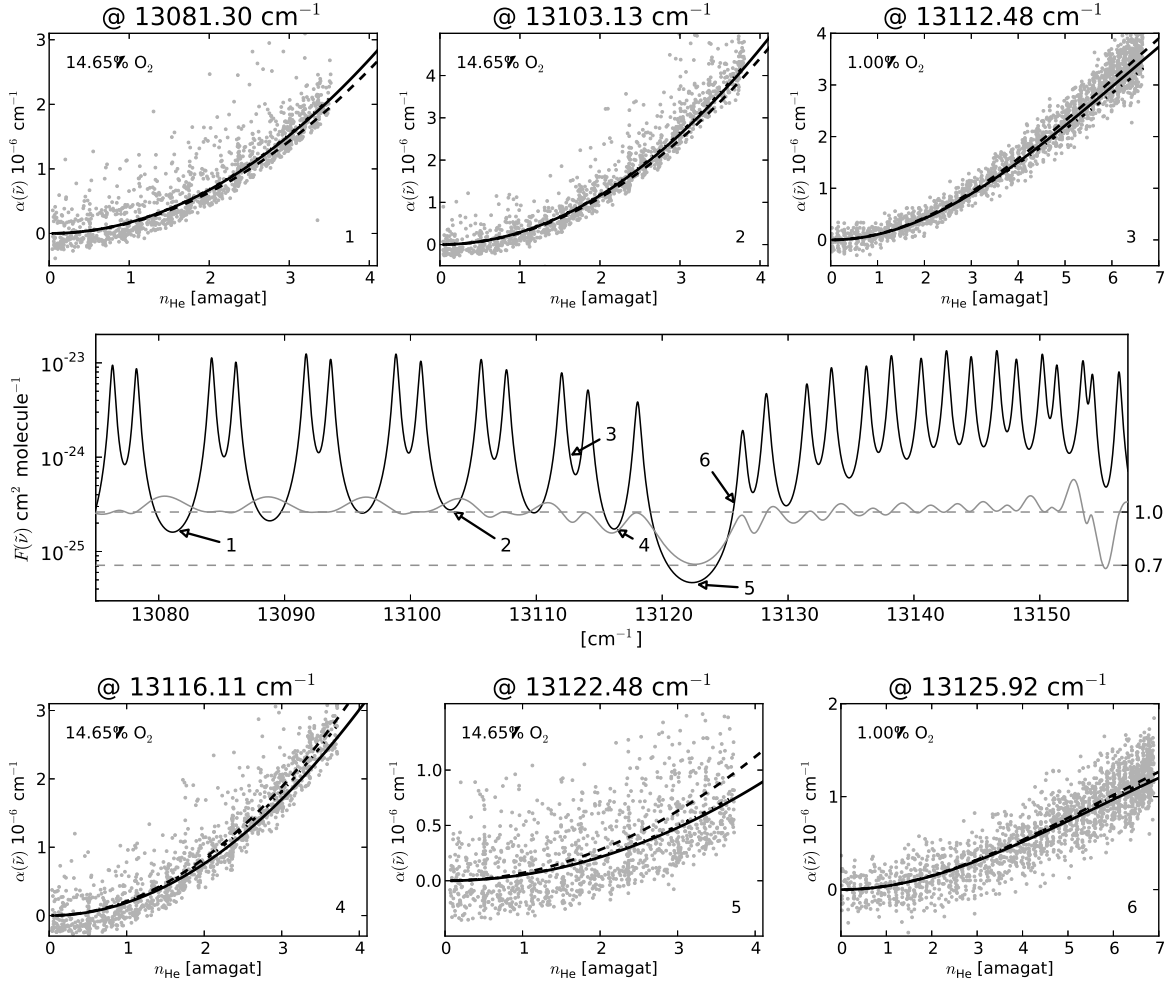


Figure 7.7: The central figure shows the calculated absorption spectrum, including line-mixing (Eq. 7.17), on a logarithmic intensity scale at $T=293 \text{ K}$ and a partial helium pressure of 5 atmosphere. The continuous grey line presents the division of this spectrum by the spectrum without line-mixing, with the dashed grey lines indicating the ratios 1.0 and 0.7. The numbered arrows indicate the spectral position of the corresponding experimental data shown in the numbered surrounding figures. In these figures grey points are measured absorption $\alpha(\tilde{\nu})$ (section 7.5) as a function of helium density n_{He} . Other lines are line-mixing (continuous), no line-mixing (dashed) and the Tonkov model (dash-dotted).

Bibliography

- [1] D. L. A. G. Grimminck, S. K. Vasa, W. L. Meerts, A. P. M. Kentgens, and A. Brinkmann, *Chem. Phys. Lett.* **509**, 186 (2011).
- [2] A. Brinkmann, S. K. Vasa, H. Janssen, and A. P. M. Kentgens, *Chem. Phys. Lett.* **485**, 275 (2010).
- [3] S. P. Brown, *Prog. NMR Spectrosc.* **50**, 199 (2007).
- [4] M. Mehring and J. S. Waugh, *Phys. Rev. B* **5**, 3459 (1972).
- [5] A. Bielecki, A. C. Kolbert, and M. H. Levitt, *Chem. Phys. Lett.* **155**, 341 (1989).
- [6] M. H. Levitt, A. C. Kolbert, A. Bielecki, and D. J. Ruben, *Solid State NMR* **2**, 151 (1993).
- [7] J. Ashida and D. Rice, *Magnetic Moments* **8**, 19 (1996), a Varian publication.
- [8] B. M. Fung, K. Ermolaev, and Y. Yu, *J. Magn. Reson.* **138**, 28 (1999).
- [9] E. Vinogradov, P. K. Madhu, and S. Vega, *Chem. Phys. Lett.* **314**, 443 (1999).
- [10] P. K. Madhu, X. Zhao, and M. H. Levitt, *Chem. Phys. Lett.* **346**, 142 (2001).
- [11] N. Khaneja, T. Reiss, C. Kehlet, T. Schulte-Herbrüggen, and S. J. Glaser, *J. Magn. Reson.* **172**, 296 (2005).
- [12] D. Sakellariou, A. Lesage, P. Hodgkinson, and L. Emsley, *Chem. Phys. Lett.* **319**, 253 (2000).
- [13] A. Lesage, D. Sakellariou, S. Hediger, B. Eléna, P. Charmont, S. Steuernagel, and L. Emsley, *J. Magn. Reson.* **163**, 105 (2003).
- [14] B. Elena, G. de Paëpe, and L. Emsley, *Chem. Phys. Lett.* **398**, 532 (2004).
- [15] E. Salager, J.-N. Dumez, R. S. Stein, S. Steuernagel, A. Lesage, B. Elena-Herrmann, and L. Emsley, *Chemical Physics Letters* **498**, 214 (2010).

- [16] N. Hansen and A. Ostermeier, *Evolutionary Computation* **9**, 159 (2001).
- [17] A. J. Vega, *J. Magn. Reson.* **170**, 22 (2004).
- [18] M. Leskes, S. Steuernagel, D. Schneider, P. Madhu, and S. Vega, *Chem. Phys. Lett.* **466**, 95 (2008).
- [19] I. Rechenberg, *Evolutionsstrategie - Optimierung technischer Systeme nach Prinzipien der biologischen Evolution*, Frommann-Holzboog, Stuttgart, 1973.
- [20] N. Hansen and S. Kern, Evaluating the CMA evolution strategy on multimodal test functions, in *Parallel Problem Solving from Nature PPSN VIII*, edited by X. Yao et al., volume 3242 of *LNCS*, pages 282–291, Springer, Berlin/Heidelberg, 2004.
- [21] W. L. Meerts and M. Schmitt, *Int. Rev. Phys. Chem.* **25**, 353 (2006).
- [22] U. Haeberlen, *High Resolution NMR in Solids. Selective Averaging.*, volume Suppl. 1 of *Advances in Magnetic Resonance*, Academic Press, New York, USA, 1976.
- [23] M. Veshtort and R. G. Griffin, *J. Magn. Reson.* **178**, 248 (2006).
- [24] J. M. Griffin, C. Tripon, S. Ago, C. Filip, and S. P. Brown, *Magn. Reson. Chem.* **45**, 198 (2007).
- [25] C. A. C. Coello, *Knowledge and Information Systems* **1**, 269 (1999).
- [26] E. Salager, R. S. Stein, S. Steuernagel, A. Lesage, B. Elena, and L. Emsley, *Chem. Phys. Lett.* **469**, 336 (2009).
- [27] M. Leskes, P. K. Madhu, and S. Vega, *The Journal of Chemical Physics* **128**, 052309 (2008).
- [28] Z. Gan, P. Madhu, J.-P. Amoureux, J. Trébosc, and O. Lafon, *Chemical Physics Letters* **503**, 167 (2011).
- [29] A. P. M. Kentgens, *Geoderma* **80**, 271 (1997).
- [30] C. P. Slichter, *Principle of magnetic resonance*, Springer, 3rd edition, 1989.
- [31] M. H. Levitt, *spin dynamics: Basics of Nuclear Magnetic Resonance*, 2001.
- [32] M. Bak, J. Rasmussen, and N. Nielsen, *J. Magn. Reson.* **147**, 296 (2000).
- [33] A. Samoson and E. Lippmaa, *Phys. Rev. B* **28**, 6567 (1983).
- [34] G. Engelhardt, A. P. M. Kentgens, H. Koller, and A. Samoson, *Solid State Nuc. Mag.* **15**, 171 (1999).
- [35] A. Samoson, E. Lippmaa, and A. Pines, *Mol. Phys.* **65**, 1013 (1988).
- [36] L. Frydman and J. S. Harwood, *J. Am. Chem. Soc.* **117**, 5367 (1995).
- [37] A. Abragam, *The principles of nuclear magnetism*, The international series of monographs on physics, Oxford University Press, 1967.
- [38] P. J. Knijn et al., *Phys. Chem. Chem. Phys.* **12**, 11517 (2010).
- [39] D. Massiot, F. Fayon, M. Capron, I. King, S. Le Calvé, B. Alonso, J. Durand,

- B. Bujoli, Z. Gan, and G. Hoatson, *Magn. Reson. Chem.* **40**, 70 (2002).
- [40] T. F. Kemp and M. E. Smith, *Solid State Nucl. Magn. Reson.* **35**, 243 (2009).
- [41] M. Wächtler, A. Schweitzer, T. Gutmann, H. Breitzke, and G. Buntkowsky, *Solid State Nucl. Magn. Reson.* **35**, 37 (2009).
- [42] G. Czjzek, J. Fink, F. Götz, H. Schmidt, J. M. D. Coey, J. P. Rebouillat, and A. Liénard, *Phys. Rev. B* **23**, 2513 (1981).
- [43] G. Le Caër and R. A. Brand, *J. Phys.: Condens. Matter* **10**, 10715 (1998).
- [44] G. Le Caër, B. Bureau, and D. Massiot, *J. Phys.: Condens. Matter* **22**, 065402 (2010).
- [45] R. Tycko, G. Dabbagh, S. R. Kurtz, and J. P. Goral, *Phys. Rev. B* **45**, 13452 (1992).
- [46] M. J. Duer, *Introduction to Solid-State NMR Spectroscopy*, Blackwell, 2004.
- [47] J. A. Hageman, R. Wehrens, R. de Gelder, W. L. Meerts, and L. M. C. Buydens, *J. Chem. Phys.* **113**, 7955 (2000).
- [48] A. Ostenmeier, A. Gawelcyk, and N. Hansen, Step-size adaptation based on non-local use of selection information., in *Parallel Problem Solving from Nature, PPSN III*, edited by Y. Davidor, H.-P. Schwefel, and R. Männer, Springer, Berlin/Heidelberg, 1994.
- [49] D. Massiot, C. Bessada, J. P. Coutures, and F. Taulelle, *J. Magn. Reson.* **90**, 231 (1990).
- [50] M. H. W. Verkuijlen, R. de Gelder, P. J. M. van Bentum, and A. P. M. Kentgens, *J. Phys. Chem. C* (2011), [dx.doi.org/10.1021/jp109927a](https://doi.org/10.1021/jp109927a).
- [51] J. Amoureux, C. Fernandez, and S. Steuernagel, *J. Magn. Reson. Ser. A* **123**, 116 (1996).
- [52] J. d’Espinose de Lacaillerie, C. Fretigny, and D. Massiot, *J. Magn. Reson.* **192**, 244 (2008).
- [53] S. A. Smith, T. O. Levante, B. H. Meier, and R. Ernst, *J. Magn. Reson. Ser. A* **106**, 75 (1994).
- [54] S. Ding and C. A. McDowell, *Chem. Phys. Lett.* **307**, 215 (1999).
- [55] D. L. A. G. Grimminck, B. J. W. Polman, A. P. M. Kentgens, and W. L. Meerts, *J. Magn. Reson.* **211**, 114 (2011).
- [56] D. L. A. G. Grimminck, B. van Meerten, and W. L. Meerts, Description and features of the program egdeconv: Automated assign and fit programs for powder nmr spectra using evolutionary algorithms, <http://egdeconv.science.ru.nl>, 2012, EGdeconv manual.
- [57] L. Marinelli and L. Frydman, *Chem. Phys. Lett.* **275**, 188 (1997).
- [58] S. Z. Ageev and B. C. Sanctuary, *Mol. Phys.* **84**, 835 (1995).

- [59] S. Ageev and B. Sanctuary, Chem. Phys. Lett. **255**, 71 (1996).
- [60] A. Kentgens, Prog. Nucl. Mag. Res. Sp. **32**, 141 (1998).
- [61] G. M. Muha, J. Magn. Reson. **53**, 85 (1983).
- [62] R. B. Creel, J. Magn. Reson. **52**, 515 (1983).
- [63] Wolfram Research, Inc., *Mathematica Edition: Version 8.0*, 2010.
- [64] P. P. Man, Mol. Phys. **78**, 307 (1993).
- [65] N. M. Trease, K. K. Dey, and P. J. Grandinetti, J. of Magn. Reson. **200**, 334 (2009).
- [66] T. T. Nakashima, K. J. Harris, and R. E. Wasylshen, J. Magn. Reson. **202**, 162 (2010).
- [67] V. B. Cheng, J. Henry H. Suzukawa, and M. Wolfsberg, J. Chem. Phys. **59**, 3992 (1973).
- [68] A. Abraham, R. Prins, J. A. van Bokhoven, E. R. H. van Eck, and A. P. M. Kentgens, J. Phys. Chem. B **110**, 6553 (2006), PMID: 16570954.
- [69] R. Siegel, T. T. Nakashima, and R. E. Wasylshen, Chem. Phys. Lett. **403**, 353 (2005).
- [70] J. Skibsted and H. J. Jakobsen, J. Phys. Chem. A **103**, 7958 (1999).
- [71] D. de Graaf, S. le Rol, H. Hintzen, L. le Gendre, and G. de With, Journal of the European Ceramic Society **26**, 2497 (2006).
- [72] P. Kempgens, R. K. Harris, Z. Yu, and D. P. Thompson, J. Mater. Chem. **11**, 2507 (2001).
- [73] D. Massiot, J. Magn. Reson. Ser. A **122**, 240 (1996).
- [74] P. R. Bunker and P. Jensen, *Molecular Symmetry and Spectroscopy*, NRC Research Press, Ottawa, second edition, 1998.
- [75] G. Herzberg, *Molecular Spectra and Molecular Structure, Vol. 1: Spectra of Diatomic Molecules*, Van Nostrand, New York, 1950.
- [76] M. Born and R. Oppenheimer, Ann. Phys. **84**, 2284 (1927).
- [77] M. Baranger, Phys. Rev. **111**, 481 (1958).
- [78] P. S. Julienne, Phys. Rev. A **26**, 3299 (1982).
- [79] P. S. Julienne and F. H. Mies, Phys. Rev. A **30**, 831 (1984).
- [80] F. H. Mies, P. S. Julienne, Y. B. Band, and S. J. Singer, J. Phys. B **19**, 3249 (1986).
- [81] P. S. Julienne and F. H. Mies, Phys. Rev. A **34**, 3792 (1986).
- [82] M. Baranger, Phys. Rev. **112**, 855 (1958).
- [83] M. Gell-Mann and M. L. Goldberger, Phys. Rev. **91**, 398 (1953).
- [84] J.-M. Hartmann, C. Boulet, and D. Robert, *Collisional effects on molecular spectra*, Elsevier, 2008.

-
- [85] J. Boisssoles, C. Boulet, and X. Bruet, *J. Chem. Phys.* **116**, 7537 (2002).
- [86] L. Monchick, *J. Chem. Phys.* **95**, 5047 (1991).
- [87] L. C. Biedenharn and J. D. Louck, *Angular Momentum in Quantum Physics*, volume 8 of *Encyclopedia of Mathematics*, Addison-Wesley, Reading, 1981.
- [88] A. Ben-Reuven, *Phys. Rev.* **141**, 34 (1966).
- [89] A. Ben-Reuven, *Phys. Rev.* **145**, 7 (1966).
- [90] A. M. Arthurs and A. Dalgarno, *Proc. R. Soc. London, Ser. A* **256**, 540 (1960).
- [91] R. Shafer and R. G. Gordon, *J. Chem. Phys.* **58**, 5422 (1973).
- [92] D. M. Brink and G. R. Satchler, *Angular Momentum*, Clarendon, Oxford, third edition, 1993.
- [93] U. Fano, *Phys. Rev.* **131**, 259 (1963).
- [94] M. O. Bulanin, A. B. Dokuchaev, M. V. Tonkov, and N. N. Filippov, *J. Quant. Spectrosc. Radiat. Transfer* **31**, 521 (1984).
- [95] M. V. Tonkov, N. N. Filippov, Y. M. Timofeyev, and A. V. Polyakov, *J. Quant. Spectrosc. Radiat. Transfer* **56**, 783 (1996).
- [96] B. v. Diedenhoven, O. P. Hasekamp, and I. Aben, *Atmos. Chem. Phys.* **5**, 2109 (2005).
- [97] B. v. Diedenhoven, O. P. Hasekamp, and J. Landgraf, *J. Geophys. Res.* **112**, D15208 (2007).
- [98] F. R. Spiering, M. B. Kiseleva, N. N. Filippov, H. Naus, B. van Lieshout, C. Weijenborg, and W. J. van der Zande, *J. Chem. Phys.* **133**, 114305 (2010).
- [99] A. Predoi-Cross, K. Harnbrook, R. Keller, C. Povey, I. Schofield, D. Hurtmans, H. Over, and G. C. Mellau, *J. Mol. Spectrosc.* **248**, 85 (2008).
- [100] H. Tran, C. Boulet, and J.-M. Hartmann, *J. Geophys. Res.* **111**, 15210 (2006).
- [101] D. A. Long, D. J. Robichaud, and J. T. Hodges, *J. Chem. Phys.* **137**, 014307 (2012).
- [102] L. Frommhold, *Collision-Induced Absorption in Gases*, Cambridge Univ. Press, Cambridge, 1994.
- [103] B. F. Minaev and H. Ågren, *J. Chem. Soc., Faraday Trans.* **93**, 2231 (1997).
- [104] B. F. Minaev and G. I. Kobzev, *Spectrochim. Acta A* **59**, 3387 (2003).
- [105] J. H. v. Vleck, *Astrophys. J.* **80**, 161 (1934).
- [106] F. Lique, *J. Chem. Phys.* **132**, 044311 (2010).
- [107] G. C. Corey and F. R. McCourt, *J. Phys. Chem.* **87**, 2723 (1983).
- [108] B. Minaev, O. Vahtras, and H. Ågren, *Chem. Phys.* **208**, 299 (1996).
- [109] J. Fischer, R. R. Gamache, A. Goldman, L. Rothman, and A. Perrin, *J. Quant. Spectrosc. Radiat. Transfer* **82**, 401 (2003).
- [110] M. C. G. N. van Vroonhoven and G. C. Groenenboom, *J. Chem. Phys.* **116**, 1954

- (2002).
- [111] G. C. Corey, *J. Chem. Phys.* **81**, 2678 (1984).
 - [112] Y. Endo and M. Mizushima, *Jpn. J. Appl. Phys.* **21**, 1379 (1982).
 - [113] P. H. Krupenie, *J. Phys. Chem. Ref. Data* **1**, 423 (1972).
 - [114] H.-J. Werner, P. J. Knowles, and *et al.*, MOLPRO: a package of ab initio programs, version 2010.1.
 - [115] T. H. Dunning, *J. Chem. Phys.* **90**, 1007 (1989).
 - [116] R. A. Kendall, T. H. Dunning, and R. J. Harrison, *J. Chem. Phys.* **96**, 6796 (1992).
 - [117] D. E. Woon and T. H. Dunning, *J. Chem. Phys.* **100**, 2975 (1994).
 - [118] F. M. Tao and Y. K. Pan, *J. Chem. Phys.* **97**, 4989 (1992).
 - [119] S. F. Boys and F. Bernardi, *Mol. Phys.* **19**, 553 (1970).
 - [120] G. C. Groenenboom and I. M. Struniewicz, *J. Chem. Phys.* **113**, 9562 (2000).
 - [121] P. J. Knowles, C. Hampel, and H.-J. Werner, *J. Chem. Phys.* **112**, E3106 (2000).
 - [122] J. D. Watts, J. Gauss, and R. J. Bartlett, *J. Chem. Phys.* **98**, 8718 (1993).
 - [123] P. J. Knowles and H.-J. Werner, *Chem. Phys. Lett.* **115**, 259 (1985).
 - [124] H.-J. Werner and P. J. Knowles, *J. Chem. Phys.* **82**, 5053 (1985).
 - [125] H.-J. Werner, *Mol. Phys.* **89**, 645 (1996).
 - [126] A. van der Avoird, P. E. S. Wormer, F. Mulder, and R. M. Berns, *Top. Curr. Chem.* **93**, 1 (1980).
 - [127] K. T. Tang and J. P. Toennies, *J. Chem. Phys.* **80**, 3726 (1984).
 - [128] T.-S. Ho and H. Rabitz, *J. Chem. Phys.* **104**, 2584 (1996).
 - [129] T.-S. Ho and H. Rabitz, *J. Chem. Phys.* **113**, 3960 (2000).
 - [130] B. R. Johnson, *NRCC Proceedings* **5**, 86 (1979).
 - [131] MATLAB, The MathWorks, Inc., <http://www.mathworks.com>.
 - [132] A. O’Keefe and D. A. G. Deacon, *Rev. Sci. Instrum.* **59**, 2544 (1988).
 - [133] G. Berden and R. Engeln, *Cavity Ring-Down Spectroscopy: Techniques and Applications*, Wiley, 2009.
 - [134] F. R. Spiering and W. J. van der Zande, *Phys. Chem. Chem. Phys.* **14**, 9923 (2012).
 - [135] J. W. Strutt, *Philosophical Magazine* **47**, 375 (1899).
 - [136] L. V. King, *Proceedings of the Royal Society of London. Series A* **104**, 333 (1923).
 - [137] D. R. Bates, *Planet Space Sci.* **32**, 785 (1984).
 - [138] H. Naus and W. Ubachs, *Opt. Lett.* **25**, 347 (2000).
 - [139] F. R. Spiering, M. B. Kiseleva, N. N. Filippov, L. van Kesteren, and W. J. van der Zande, *Phys. Chem. Chem. Phys.* **13**, 9616 (2011).

- [140] F. R. Spiering, M. B. Kiseleva, N. N. Filippov, H. Naus, B. Lieshout, A. M. van der Veen, and W. J. van der Zande, *Mol. Phys.* **109**, 535 (2011).
- [141] D. J. Robichaud, J. T. Hodges, L. R. Brown, D. Lisak, P. Mas, L. Y. Yeung, M. Okumura, and C. E. Miller, *J. Mol. Spectrosc.* **248**, 1 (2008).
- [142] L. Rothman et al., *J. Quant. Spectrosc. Radiat. Transfer* **110**, 533 (2009).
- [143] R. S. Pope, P. J. Wolf, and G. P. Perram, *J. Mol. Spectrosc.* **223**, 205 (2004).
- [144] K. J. Ritter and T. D. Wilkerson, *J. Mol. Spectrosc.* **121**, 1 (1987).

Summary

The use of computers to help us perform tasks more efficiently is common practice in the modern world. Applications vary from writing texts on your personal computer, to complex weather and climate predictions, and embedded computers in your car or electronic devices. This thesis covers a range of computer applications in the research field of spectroscopy, *i.e.*, the study of light-matter interaction. In seven chapters we move from using the computer to steer an NMR spectrometer in search of the best settings, to extracting information about the molecular structure of materials from NMR spectra, and finally the computation of quantum mechanical predictions for the absorption of light by molecular oxygen in the atmosphere. Each topic is covered by an introduction followed by the corresponding publication(s).

In chapter 1 the problem of broad spectral features due anisotropic (angular dependent) interactions in nuclear magnetic resonance (NMR) spectra of solid-state materials is introduced. This broadening for example due to proton-proton interactions overshadows the spectral features of other important interactions, such as the chemical shift or J-coupling. Knowledge of these other interactions provides additional and important information about the structure of the material at the molecular level. The simple trick of mechanically rotating the material (sample) at an angle of 54.74° provides a way to spatially average part of the not-wanted interaction anisotropy towards zero. The remaining interaction anisotropy may be removed (partly) by manipulation of the spin system with a radio frequency (rf) field. This rf-field can be shaped almost arbitrarily, and combined with sample rotation it is a complex matter to find the best pulse sequence for proton decoupling.

In the approach presented in chapter 2 an evolutionary algorithm is used to optimise rf-pulse sequences. This is performed in a feed-back loop set up between NMR spec-

trometer and a computer. Firstly our converged results for experiments at moderate sample spinning speed and rf-field strength are presented. These confirm the optimal performance of pulse shapes readily available in the literature. Simulation of the experiment reproduces the experimental results, which indicates a (near) ideal behaviour of the experimental setup and the spin system. Subsequently, an experiment is presented that is carried out at very high rf-field strength and moderate sample spinning speed. Here we find a new pulse sequence with a competitive performance compared to experiments performed at high sample spinning speeds. Such an effective decoupling at very high rf-field strength has not been demonstrated before in the literature. Simulation of the experimental results shows differences, which are possibly caused by imperfections in the phase modulation of the pulses.

In chapter 3 a new topic, the analysis of solid-state NMR spectra of quadrupolar nuclei, is introduced. Nuclei with a quadrupole moment interact with the electric field gradient (e.f.g.) of their surroundings. The full description of this interaction, requires knowledge of two interaction parameters C_q and η . These parameters determine the interaction strength and the local asymmetry of the e.f.g., providing direct information about the different local structures in the studied material. To extract these interaction parameters and the relative occurrence of the different local structures from the experimental spectrum, we simulate and fit a theoretical spectrum to the data. This simulated spectrum is the sum of subspectra, that each correspond to one presumed local structure. Evolutionary algorithms are used to guide the fitting process.

Chapter 4 presents the analysis of 1D data. The first step in the simulation is the calculation of a library of spectra as a function of η and C_q using second-party simulation software. During the actual fitting process the library is read into the computer's internal memory, which allows for a fast synthesis of a theoretical spectrum. With this approach the most time-consuming simulation step is removed from the fitting process. In particular the fitting of spectra of disordered materials, represented by a distribution in interaction parameters, benefits from this approach. Three case studies are presented. The program (*EASY-GOING deconvolution*) has been made available to the NMR community.

In chapter 5 the *EASY-GOING deconvolution* program is extended with the ability to simulate and fit multiple-quantum magic angle spinning (MQMAS) data. The power of this type of 2D experiment, that correlates a multi-quantum coherence with a single-quantum coherence, is that an isotropic spectrum is obtained after transformation of the data. Now the information of the formerly overshadowed chemical shift interaction is obtained. In contrast to the 1D simulation model, this data is simulated using a fully analytical model, which is both fast and accurate in describing the complex excitation

behaviour of quadrupolar nuclei (implicitly multi-level quantum systems). Three case studies are presented to show the capabilities of the program that is made available to the NMR community.

In chapters 6 and 7 the final topic of this thesis is treated. Here the collisional effects of helium on the rotationally resolved magnetic dipole A-band absorption spectrum of molecular oxygen is studied theoretically. Molecular oxygen in the atmosphere absorbs significant amounts of electromagnetic radiation in the A-band region (≈ 760 nm). Collisions with other particles change the wavelength dependence of this absorption. For a better understanding of the mechanisms involved, the relatively simple collision partner helium was used. The collisional effects on the A-band spectrum are treated in the impact approximation that is introduced in chapter 6. From this description follows that absorption lines in the spectrum may be coupled to each other via the occurrence of inelastic collisions, *i.e.*, collisions that change the state of the oxygen molecule. This is called line-mixing.

In chapter 7 a fully quantum mechanical treatment is used to accurately describe these collisions. To this end a new interaction potential was computed for helium with the excited b state of oxygen, the final state of the electronic A-band transition. The theory for the spectroscopy of oxygen for this transition is described in full, before treating the spectrum in the impact approximation. Our calculated results for the integrated line cross sections and the broadening coefficients of several spectral lines are in good agreement with experimental results from the literature. Additionally, cavity ring-down data were measured to compare with the theoretical predictions. This technique enables the measurement of minute absorption strengths between spectral lines of the A-band spectrum that are sensitive for the effect of line-mixing. Using these data we show that line-mixing is an important mechanism to correctly determine the collisional absorption strength dependence. With this work we are the first in the literature to present the fully quantum mechanical treatment of collisional effects on a molecular electronic transition in the impact approximation.

Samenvatting

Het gebruik van computers om taken efficiënter uit te voeren is een alledaagse bezigheid in de moderne tijd. De toepassingen variëren van het tekstverwerken op de pc, tot complexe weer-en klimaatvoorspellingen en de ingebouwde computers in de auto en elektronische apparaten. Deze thesis beschrijft een brede variatie aan toepassingen van de computer in het onderzoeksveld van de spectroscopie, oftewel het bestuderen van licht-materie interactie. Gedurende zeven hoofdstukken wordt beschreven hoe de computer gebruikt kan worden voor het aansturen van een NMR spectrometer om de beste instellingen te vinden, hoe informatie over de moleculaire structuur van materialen uit NMR spectra kan worden gehaald, en hoe met behulp van quantum mechanica de absorptie van licht door moleculair zuurstof in de atmosfeer kan worden uitgerekend en voorspelt. Elk onderwerp wordt beschouwd doormiddel van een introductie en het bij het onderwerp gepubliceerde werk.

In hoofdstuk 1 wordt het probleem beschouwd van brede spectrale lijnvormen veroorzaakt door anisotrope (hoekafhankelijke) interacties in Nuclear Magnetic Resonance (NMR) spectra, in het Nederlands magnetische kernspin resonantie, van vaste stoffen. Deze verbreding, die bijvoorbeeld wordt veroorzaakt door proton-proton interacties, overschaduwde de spectrale lijnvormen van andere belangrijke interacties zoals de chemische verschuiving en de J-koppeling. Hierdoor gaat extra informatie over de structuur van een materiaal op moleculair niveau verloren. Een eenvoudige truc als het mechanisch roteren van het materiaal onder een hoek van 54.74° , maakt het mogelijk om een gedeelte van de niet-gewilde anisotropie van de interactie ruimtelijk uit te middelen richting nul. De overblijvende anisotropie kan weer verder worden verwijderd doormiddel van het manipuleren van het spinsysteem met een radiofrequent (rf) veld. Dit veld kan een nagenoeg willekeurige vorm gegeven worden. In combinatie

met de mechanische rotatie wordt het vinden van de beste pulssequentie een complex probleem.

De aanpak die wordt gepresenteerd in hoofdstuk 2 is het gebruik van een evolutionair algoritme voor het optimaliseren van de rf pulssequentie. Om dit te bereiken is een feed-back loop tussen NMR spectrometer en computer opgezet. Eerst worden de geconvergeerde resultaten gepresenteerd voor experimenten bij matige rotatiesnelheid en rf veldsterkte. Deze experimenten bevestigen het optimaal presteren van pulssequenties uit de literatuur. Simulatie van de experimenten reproduceert de resultaten. Dat geeft aan dat de experimentele opstelling zich nagenoeg perfect gedraagt. Daarna wordt een experiment gepresenteerd dat is uitgevoerd bij matige rotatiesnelheid en zeer hoge rf veldsterkte. Hier vinden we een nieuwe pulssequentie die competitief presteert in vergelijking met experimenten uitgevoerd bij hoge rotatiesnelheid. Simulatie van dit experiment reproduceert de resultaten niet volledig, dit is mogelijk veroorzaakt door imperfecties in de fasemodulatie van de pulsen in het experiment.

In hoofdstuk 3 wordt een nieuw onderwerp geïntroduceerd, namelijk de analyse van vaste stof NMR spectra van quadropoolkernen. Atoomkernen met een quadropool moment hebben een interactie met de elektrische veldgradiënt (e.v.g.) van hun omgeving. De beschrijving van deze interactie ligt vast aan de hand van twee interactie parameters C_q en η . Deze parameters beschrijven de interactiesterkte en de lokale asymmetrie van de e.v.g., en geven daardoor directe informatie over de verschillende lokale structuren in het bestudeerde materiaal. Het bepalen van de interactieparameters en de relatieve hoeveelheden van de lokale structuren uit het experimentele spectrum, wordt gedaan aan de hand van het simuleren en fitten van de data. Het gesimuleerde spectrum is de som van subspectra, waarvan elk subspectrum correspondeert met een lokale structuur. Evolutionaire algoritmen worden gebruikt om het fitproces te sturen.

Hoofdstuk 4 behandelt de analyse van 1D data. De eerste stap in de simulatie is het berekenen van een bibliotheek van spectra als functie van η en C_q met reeds beschikbare simulatie software van een andere onderzoeksgroep. Gedurende het fitproces is de bibliotheek in het computer werkgeheugen geladen, dit zorgt voor de snelle synthese van een theoretisch spectrum. Met deze aanpak is de meest tijdconsumerende stap uit de simulatie gehaald. Met name het fitten van spectra van wanorderlijke materialen, gerepresenteerd door een distributie van interactie parameters, gaat sneller met deze aanpak. Drie toepassingen van het programma worden besproken. Het nieuwe programma, genaamd *EASY-GOING deconvolution*, is beschikbaar gesteld voor de NMR gemeenschap.

In hoofdstuk 5 wordt het *EASY-GOING deconvolution* programma uitgebreid met de mogelijkheid om multi-quantum magic angle spinning (MQMAS) data te kunnen

simuleren en fitten. De kracht van dit type 2D experiment, dat multi-quantum coherentie correleert met single-quantum coherentie, is dat het isotrope spectrum wordt verkregen na transformatie van de data. De informatie over de voorheen overschaduwde chemische verschuiving interactie wordt zo beschikbaar. In tegenstelling tot het 1D simulatie model, wordt deze data gesimuleerd aan de hand van een volledig analytisch model wat zowel snel als accuraat het complexe excitatiegedrag van quadropool kernen (impliciet multi-level quantum systemen) kan beschrijven. Drie toepassingen worden besproken om de mogelijkheden van het programma te laten zien.

In de hoofdstukken 6 en 7 wordt het laatste onderwerp behandeld. Het gaat hier om de theoretische studie van de botsingseffecten van helium op het rotatie-opgeloste magnetische dipool A-band absorptie spectrum van moleculair zuurstof. Moleculair zuurstof in de atmosfeer absorbeert significante hoeveelheid elektromagnetische straling in de A-band regio (≈ 760 nm). Botsingen met andere deeltjes veranderen de golflengte afhankelijkheid van deze absorptie. Om de deelnemende processen beter te kunnen begrijpen, wordt de relatief eenvoudige botsingspartner helium gebruikt. Het botsings-effect op het A-band spectrum wordt beschreven in de impact benadering die wordt geïntroduceerd in hoofdstuk 6. Uit deze beschrijving volgt dat absorptielijnen in het spectrum met elkaar gekoppeld kunnen zijn door inelastische botsingen, oftewel botsingen die de toestand van het zuurstof molecuul veranderen. Dit mechanisme wordt line-mixing genoemd.

In hoofdstuk 7 worden de botsingen volledig quantum mechanisch beschreven. Om die reden is er een nieuwe interactie potentiaal berekend tussen helium en de elektronisch aangeslagen b toestand van zuurstof, de eindtoestand van de elektronische A-band overgang. De theorie voor de spectroscopie van zuurstof voor deze overgang wordt volledig uitgeschreven, voordat het spectrum in de impact benadering wordt gegeven. De berekende resultaten voor de geïntegreerde lijndoorsnedes en de botsingsverbredingscoëfficiënten voor meerdere spectrale lijnen komen goed overeen met de experimentele resultaten uit de literatuur. Daarnaast zijn er cavity ring-down experimenten uitgevoerd om te kunnen vergelijken met de theoretische voorspellingen. Deze techniek biedt de mogelijkheid om minieme absorptiesterktes te meten tussen de spectrale lijnen in het A-band spectrum, gebieden die gevoelig zijn voor het effect van line-mixing. Met behulp van deze data laten we zien dat line-mixing een belangrijk mechanisme is voor het correct beschrijven van de botsingsafhankelijkheid van de absorptiesterkte. Met dit werk zijn we de eerste in de literatuur die laten zien dat het mogelijk is om met een volledig quantum mechanische beschrijving en de impact benadering de botsingseffecten op een moleculaire elektronische overgang goed te beschrijven.

Publications

1. D. L. A. G. Grimminck, F. R. Spiering, L. M. C. Janssen, W. J. van der Zande, G. C. Groenenboom *A theoretical and experimental study of pressure broadening of the oxygen A-band by helium*, in preparation
2. D. L. A. G. Grimminck, B. van Meerten, M. H. W. Verkuijlen, E. R. H. van Eck, W. L. Meerts, and A. P. M. Kentgens, *EASY-GOING deconvolution: Automated MQ-MAS NMR spectrum analysis based on a model with analytical crystallite excitation efficiencies*, J. Magn. Reson. 228, 116-124 (2013)
3. D. L. A. G. Grimminck, *Kernspin interactie-engineering in de vaste-stof-NMR: Manipuleren in Euclidische en spinruimte*, Ned. Tijdschr. Natuurkd. 78, 152-155 (2012)
4. D. L. A. G. Grimminck, B. J. W. Polman, A. P. M. Kentgens, and W. L. Meerts, *EASY-GOING deconvolution: Combining accurate simulation and evolutionary algorithms for fast deconvolution of solid-state quadrupolar NMR spectra*, J. Magn. Reson. 211, 114-120 (2011)
5. D. L. A. G. Grimminck, S. K. Vasa, W. L. Meerts, A. P. M. Kentgens, and A. Brinkmann, *EASY-GOING DUMBO on-spectrometer optimisation of phase modulated homonuclear decoupling sequences in solid-state NMR*, Chem. Phys. Lett. 509, 186-191 (2011)
6. P. J. Knijn, P. J. M. van Bentum, E. R. H. van Eck, C. Fang, D. L. A. G. Grimminck, R. A. de Groot, R. W. A. Havenith, M. Marsman, W. L. Meerts, G. A. de Wijs and A. P. M. Kentgens, *A solid-state NMR and DFT Study of Compositional Modulations in $Al_xGa_{1-x}As$* , Phys. Chem. Chem. Phys. 12, 11517-11535 (2010)

Curriculum Vitae

Name	(Dennis) Leonardus Adrianus Gerardus Grimminck
Date of birth	May 28, 1985
Place of birth	Roosendaal en Nispen, The Netherlands
2009 – 2012	PhD at the Institute for Molecules and Materials, Radboud University Nijmegen. Research groups: Molecular and Biophysics, Solid-State NMR, and Theoretical Chemistry
2008	Four-month research project in the group of Prof. M. Schmitt Heinrich Heine Universität, Düsseldorf Research topic: Anharmonic corrections for the constants of motion of semi-rigid molecules.
2006 – 2008	MSc in Chemistry, Radboud University Nijmegen (<i>cum laude</i>) <ul style="list-style-type: none">• Major: Molecular and Biophysics, and Solid-State NMR groups Thesis title: <i>Fitting an NMR powder spectrum of $Al_xGa_{1-x}As$, using genetic algorithms</i>• Minor: Six-month research project in the group of Prof. P. Čársky, J. Heyrovský Institute, Prague. Research topic: Implementation of a complex DFT electron cor- relation potential for electron scattering calculations.
2003 – 2006	BSc in Chemistry, Radboud University Nijmegen